Satellite optical remote sensing of clouds and aerosols: From particle single-scattering and gaseous absorption through radiative transfer to retrieval products

Ping Yang[1], Kerry Meyer[2], Robert Levy[2], Dongchen Li[1], Feng Xu[3], Anita D. Rapp[1], Zhibo Zhang[4]

***Abstract*— Clouds and aerosols are fundamental regulators of Earth's radiation budget and climate system, influencing both solar and terrestrial radiation through scattering, absorption, and emission processes. Accurate characterization of their physical and radiative properties from space requires a rigorous understanding of particle single-scattering, gaseous absorption, and radiative transfer in the atmosphere, as well as reliable inversion methods. This review synthesizes the physical foundations and algorithmic implementations of satellite-based passive optical remote sensing of clouds and aerosols, spanning the ultraviolet to thermal infrared spectral range. Beginning with electromagnetic scattering theory and state-of-the-art methods for computing single-scattering by nonspherical particles and computationally efficient methods for accounting for atmospheric absorption, we discuss the radiative transfer framework underpinning cloud and aerosol retrievals. The connection between single-scattering and multiple-scattering is rigorously formulated. We then summarize operational and research-grade retrieval techniques, including cloud masking and thermodynamic phase determination, CO_2 slicing for cloud-top pressure, the Nakajima-King shortwave bi-spectral, and infrared split-window approaches for cloud optical thickness and effective particle size, inversion algorithms for determining aerosol properties from multi-spectral and/or multi-angle radiometric and polarimetric measurements, and active-passive sensing synergy. Examples of the global cloud and aerosol climatologies are illustrated using observations from the Moderate Resolution Imaging Spectroradiometer (MODIS) and the Multi-angle Imaging SpectroRadiometer (MISR). Furthermore, the unique strengths of active remote sensing techniques based on spaceborne lidar observations are briefly elaborated in the context of studying ice clouds composed of randomly and horizontally oriented ice crystals, which is a significant challenge for conventional passive remote sensing techniques. By connecting physical theory to practical retrievals, this review highlights both the maturity of current methodologies and the remaining challenges in reducing uncertainties in particle morphology, vertical structure, absorption, and aerosol-cloud interactions. Furthermore, the impact of artificial intelligence (AI) on atmospheric remote sensing is briefly addressed.**

***Index Terms*—**Aerosols, clouds, cloud mask, cloud phase, cloud-top pressure, effective particle size, gaseous absorption, light scattering, optical thickness, radiative transfer, radiometric and polarimetric remote sensing

The manuscript was submitted on March 16, 2026. This work was primarily supported in part by the endowment funds (02-512231-00000) associated with the David Bullock Harris Chair in Geosciences at Texas A&M University. Texas A&M High Performance Research Computing (HPRC) clusters were used in the light-scattering computations presented in this paper.
(Corresponding author: Ping Yang; email: pyang@tamu.edu).

I. INTRODUCTION

Clouds and aerosols are two critical components of Earth's atmosphere, with both short-term and long-term effects on weather variability and the climate system through their microphysical and radiative effects. Clouds regulate the planetary energy budget by modulating incoming solar radiation and outgoing terrestrial infrared (IR) emission, while aerosols affect radiation directly through scattering and absorption and indirectly through their interactions with clouds. The complex interplay between clouds and aerosols shapes the radiative balance, hydrological cycle, and atmospheric dynamics, thus rendering the accurate characterization and monitoring of their properties essential for improved weather prediction and climate modeling.

Clouds are ubiquitous, covering on average 65-68% of Earth's surface, though these values are sensitive to detection thresholds, which range from 56% when only optically thick clouds (optical thickness > 2) are considered, to as high as 73% when subvisible cirrus clouds are included [1], [2]. Based on their thermodynamic phase, clouds can be classified as water clouds composed of liquid water droplets spanning a range of sizes, ice clouds composed of complex ice crystals with various morphologies and sizes, or mixed-phase clouds in which liquid droplets and ice crystals coexist. Of this total, ice clouds account for, depending on instrument sensitivity and the cloud optical thickness threshold applied as criteria to cloud classification or detection, approximately 30–40% globally [2], with substantially higher fractions in the tropics, where ice cloud coverage typically averages 60% and higher (e.g., the maximum cirrus cloud amounts that occur over the western pacific warm pool can be as large as 70%) in regions of persistent deep convection [2], [3]. Differences in cloud thermodynamic phase are radiatively significant because liquid droplets and ice crystals have distinct optical properties, namely the extinction efficiency, single-scattering albedo, and phase function (or the phase matrix if the polarization state of the radiation field is of concern, such as in polarimetric remote sensing applications). Our knowledge of the microphysical and

[1]Department of Atmospheric Sciences, Texas A&M University, College Station, TX; [2]NASA Goddard Space Flight Center, Greenbelt, MD; [3]School of Meteorology, University of Oklahoma, Norman, OK. [4]Department of Physics, University of Maryland, Baltimore County, Baltimore, MD.

radiative properties of ice clouds is much more limited than that of water clouds. Furthermore, it is even more challenging to achieve a robust understanding of mixed-phase clouds from both measurements and theoretical studies.

While exceptions occur, cloud thermodynamic phase generally varies systematically with height: Low-level clouds forming in warmer environments consist primarily of liquid water droplets, while high-level clouds near the colder tropopause region are composed mainly of ice crystals. Intermediate-level clouds can be mixed phase, containing a mixture of supercooled liquid droplets and ice particles. Cloud characteristics are closely tied to atmospheric stability, temperature, and altitude. For example, cirrus clouds are typically higher than 6 km, with their delicate, wispy, and feathery appearance as demonstrated in the example cirrus clouds in Fig. 1 (upper panel) observed over College Station, Texas, USA, on February 12, 2026. The typical horizontal dimension of a fair-weather cumulus cloud (cumulus humilis) is approximately 1 km with vertical thickness less than 1 km. In stable conditions, clouds often form stratiform layers that extend horizontally over large distances but remain relatively shallow, typically less than 1 km thick. In unstable conditions, deep convective systems can develop, extending from near the surface to the upper troposphere, and coupling lower- and upper-atmospheric processes. The International Satellite Cloud Climatology Project (ISCCP) cloud classification scheme developed by Rossow and Schiffer [4] has been extensively used in satellite-based remote sensing, cloud climatology studies, and climate modeling simulations (e.g., [5]) to classify clouds in terms of their heights and optical thicknesses in the visible spectrum. As illustrated in the lower panel of Fig. 1, ISCCP classifies clouds with cloud-top pressures higher than 680 hPa as low clouds, including cumulus, stratocumulus, and stratus; clouds with cloud-top pressures between 440-680 hPa as middle clouds, including altocumulus, altostratus, and nimbostratus; and those with cloud-top pressures lower than 440 hPa as high clouds, including cirrus, cirrostratus, and cumulonimbus associated with deep convection, mainly thunderstorms.

The modulation of both incoming solar radiation and outgoing terrestrial thermal IR emission by clouds is critically dependent on the cloud phase and microphysical properties. Solar radiation spans ultraviolet through visible to near- and mid-IR wavelengths (approximately 0.4–5 μm), while absorbed energy is reemitted by the Earth–atmosphere system at longer IR wavelengths (roughly 3–100 μm). Low-level liquid water clouds generally have high albedos and efficiently reflect solar radiation, producing a net cooling effect. High-level ice clouds, particularly thin cirrus clouds, both reflect sunlight and absorb outgoing longwave radiation emitted from the surface and lower atmosphere. By trapping IR radiation, these ice clouds can contribute to atmospheric warming. The net radiative forcing effect of a specific cloud (whether warming or cooling dominates) therefore depends on its altitude, thermodynamic phase, optical thickness, single-scattering albedo, and scattering phase function.

Monitoring these properties on a global scale relies heavily on satellite observations. Polar-orbiting and geostationary meteorological satellites provide continuous observations of cloud macrophysical properties, such as cloud-top height and thermodynamic phase, as well as microphysical and optical characteristics, including cloud optical thickness and effective particle size. These observations are essential for numerical weather prediction, where near-real-time cloud information improves forecasts of precipitation, temperature, and severe weather. Over longer timescales, satellite-derived cloud climatologies are used to evaluate and refine global climate models. However, constructing consistent multi-decadal datasets presents challenges, as sensor calibration must remain stable despite instrument degradation, orbital changes over time, and platform or instrument changes.

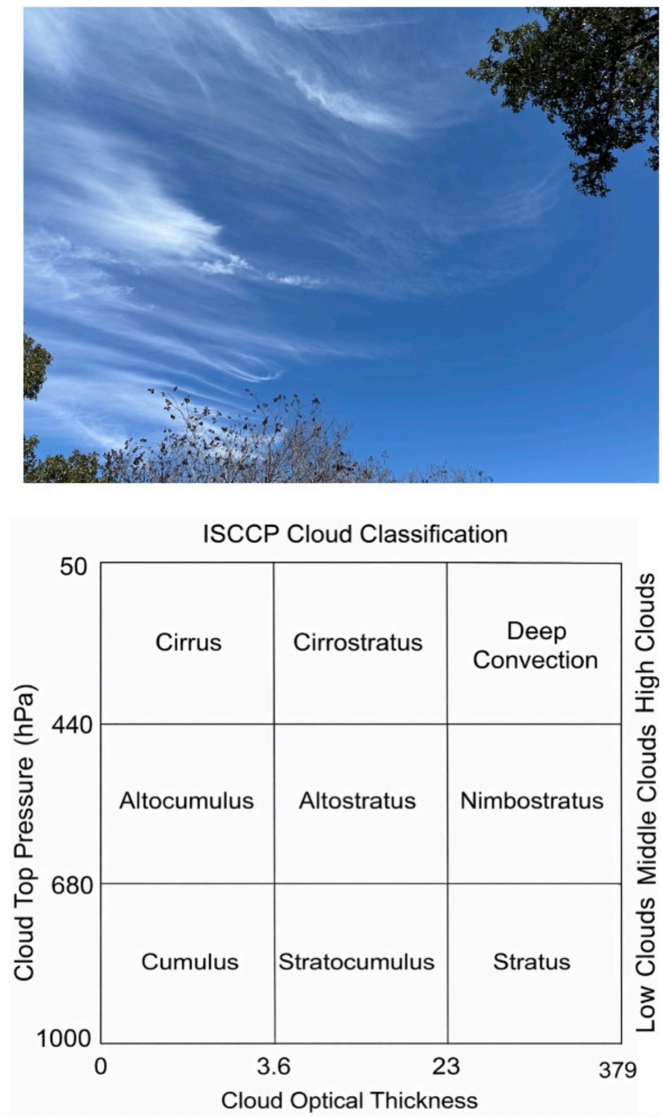

Fig. 1. (Upper panel): an image of cirrus clouds, taken on the campus of Texas A&M University in College Station, Texas, USA, on February 12, 2026; (Lower panel) the ISCCP cloud classification scheme based on cloud optical thickness and cloud-top pressure [4].

Retrieving cloud properties from space requires interpreting radiances measured in carefully selected spectral bands, typically located within atmospheric "windows" to minimize gaseous absorption effects. Visible and shortwave IR measurements are converted to bi-directional reflection functions, while thermal IR observations are expressed as brightness temperatures (BTs). Radiative transfer models and retrieval algorithms then infer cloud-top pressure, thermodynamic phase (ice, water, or mixed), optical thickness, and effective particle size based on these measurements of reflectance or BTs. While the optical properties of liquid water clouds composed of spherical water droplets can often be well quantified using the well-established Lorenz-Mie theory [6], [7], ice clouds are more complex. Ice crystals occur in a wide variety of nonspherical habits or shapes [8], [9], such as columns, plates, aggregates, bullet rosettes, overall irregular forms, and morphologies with small-scale irregularities or surface roughness, leading to intricate scattering behavior and greater uncertainty in their radiative representation [10]. Ongoing advances in light-scattering and radiative transfer simulations, satellite retrieval techniques, multi-spectral and multi-angular observations, radiometric and polarimetric measurements, and field campaigns continue to improve the characterization of both liquid and ice clouds and their representations in weather and climate models.

As another important constituent of the atmosphere that is critical to the terrestrial radiation budget and climate system, atmospheric aerosols are airborne small particles that can be classified in terms of three main size modes based on the particle diameters: the Aitken mode (10 nm - 0.1 μm), the accumulation or fine mode (0.1-2.5 μm), and the coarse mode (>2.5 μm). In addition to their well-known impacts on air quality and public health, aerosols influence radiative transfer directly through scattering and absorption of solar and terrestrial thermal radiation (the aerosol direct effect), and indirectly through interactions with clouds (the aerosol indirect effect). For the former, scattering aerosols such as sulfates and sea salt enhance planetary reflectivity and exert a cooling effect, whereas absorbing aerosols, such as black carbon, can warm the atmosphere by altering vertical temperature profiles. For the latter, aerosols may serve as cloud condensation nuclei and ice-nucleating particles, modifying cloud droplet number concentration, optical thickness, lifetime, and precipitation efficiency [11], [12], [13]. For the semi-direct effect, absorbing aerosols such as black carbon cause local heating of the atmosphere. The magnitudes of these radiative effects depend on particle loadings, absorption, composition, size distribution, morphology, vertical distribution, and underlying surface properties.

Aerosol optical behavior is spectrally dependent and governed by key parameters including aerosol optical depth (AOD), single-scattering albedo (SSA), and the asymmetry parameter (g). Globally, visible AOD typically ranges from 0.1 to 0.15 but can exceed 5.0 during intense dust or smoke events. SSA generally ranges from 0.8 to near 1.0 in visible wavelengths, and the asymmetry parameter commonly falls between 0.6 and 0.75. Aerosol populations are commonly represented by combinations of lognormal size distributions, with the scattering efficiency maximized when particle sizes are comparable to the wavelength of the incident radiation. Fine-mode particles efficiently scatter visible radiation, while coarse-mode particles more strongly influence shortwave IR wavelengths. These spectral characteristics provide critical insight into aerosol size, composition, and loading that can be exploited with carefully selected measurements.

Ground-based sunphotometers, e.g., those deployed by the AErosol RObotic NETwork (AERONET) project [14], provide the most direct measurement of column-integrated AOD with spectral dependence characterized by the Ångström exponent. However, satellite-based aerosol remote sensing remains challenging due to factors such as variability in underlying surface reflectance, molecular scattering, gaseous absorption, cloud contamination, and instrument limitations in spatial, spectral, and temporal resolution. Retrieval algorithms must therefore rely on simplifying assumptions and cloud-masking techniques. Although advances in multi-angle, multispectral, polarization-sensitive, and lidar observations have improved aerosol characterization, accurately constraining aerosol absorption, vertical distribution, and aerosol–cloud interactions from spaceborne observations remains a central scientific challenge.

Together, aerosols and clouds constitute a tightly coupled system that regulates atmospheric radiation and climate. Continued advances in observational capabilities, theoretical understanding, and modeling approaches are essential to reduce uncertainties and improve predictions of their combined influence on weather and climate systems. In the literature, a number of papers have been published on satellite-based remote sensing of clouds and aerosols, such as [15], [16], [17], [18], [19], [20], [21], [22], to list just a few.

The present review summarizes satellite-based remote sensing of cloud and aerosol properties using visible through IR wavelengths. Because the single-scattering, absorption, and multiple-scattering (radiative transfer) processes are both essential to the physical principles and implementations of remote sensing techniques, Section 2 recapitulates the physical fundamentals of light scattering and radiative transfer, including a summary of state-of-the-art light-scattering computational capabilities and computationally efficient methods for accounting for absorption by atmospheric gases. Sections 3 and 4 summarize the physical basis for cloud mask and cloud thermodynamic phase determination. In particular, the cloud mask and cloud phase algorithms developed by the Moderate Resolution Imaging Spectroradiometer (MODIS) science team are reviewed. Section 5 reviews the widely used CO_2 slicing method [23], originally developed to infer cloud-top pressure. Section 6 reviews a bi-spectral method [24] based on a visible and a near-IR channel, and the thermal split-window method based on the BT in one thermal window channel and the BT difference (BTD) in two thermal window channels. Examples of cloud property retrievals based on MODIS observations are presented. Section 7 reviews the well-known dark target (DT) and the Deep-Blue (DB) aerosol retrieval algorithms. Retrieval examples based on DT are also shown. Section 8 reviews an aerosol property retrieval algorithm based on collocated observations by an active sensor (a spaceborne lidar) and a passive sensor (an imaging IR radiometer, IIR). Section 9 summarizes aerosol property retrievals based on observations by the Multi-angle Imaging SpectroRadiometer (MISR). Section 10 summarizes a polarimetric aerosol property retrieval method. Section 11 briefly discusses inferring the percentage of horizontally oriented ice crystals in ice clouds from spaceborne lidar observations, a task unachievable with passive remote sensing techniques. Section 12 concludes this review.

II. PARTICLE SINGLE-SCATTERING, GASEOUS ABSORPTION, AND RADIATIVE TRANSFER IN THE ATMOSPHERE

Particles in the atmosphere, such as ice crystals in cirrus clouds, liquid droplets in water clouds, or aerosols, can substantially modify the radiation field in the atmosphere under cloudy or aerosol-laden conditions. Knowledge of single-particle scattering by particles, gaseous absorption, and radiative transfer of electromagnetic radiation in the atmosphere is essential for implementing remote sensing techniques. In this section, we briefly elucidate the physical fundamentals of particle single-scattering, gaseous absorption, and radiative transfer processes in a plane-parallel atmosphere, i.e., one that is horizontally homogeneous.

A. Scattering of Radiation by Individual Particles

To understand single-scattering by an individual particle, let us consider the attenuation of light due to the presence of a particle under illumination by a collimated beam (i.e., the light beam propagates in only one direction). The physical quantity that quantifies light attenuation is called the extinction cross section, and it differs in value from the particle's projected area. The extinction process involves two distinct physical mechanisms, namely scattering and absorption. In the following discussions, we consider only elastic scattering, i.e., the redistribution or partial redistribution of the incident electromagnetic energy in all directions, with the scattered and incident electromagnetic waves having the same frequency. The absorption process converts electromagnetic energy into a different energy form, particularly heat. The extinction, scattering, and absorption cross sections, C_e , C_s and C_a, have units of area and satisfy the following relation:

$$C_e = C_s + C_a. \tag{1}$$

In practical applications, we usually quantify the extinction, scattering, and absorption processes in terms of dimensionless efficiency factors Q_e, Q_s and Q_a, which are the ratios of the corresponding cross sections to the projected area A_p of the particle on a plane perpendicular to the incident direction:

$$Q_e = C_e/A_p,\ Q_s = C_s/A_p,\ \text{and}\ Q_a = C_a/A_p, \tag{2}$$

where

$$Q_e = Q_s + Q_a. \tag{3}$$

Another quantity that specifies the scattering ability of a particle is the SSA, defined as

$$\widetilde{\omega} = \frac{C_s}{C_e} = \frac{Q_s}{Q_e} = 1 - \frac{Q_a}{Q_e}. \tag{4}$$

To quantify the angular distribution of the scattered electromagnetic energy and associated polarization state, let us consider the incident-scattering geometric configuration in Fig. 2. The plane containing the incident and scattering directions is referred to as the scattering plane, and the angle θ between the two directions is called the scattering angle.

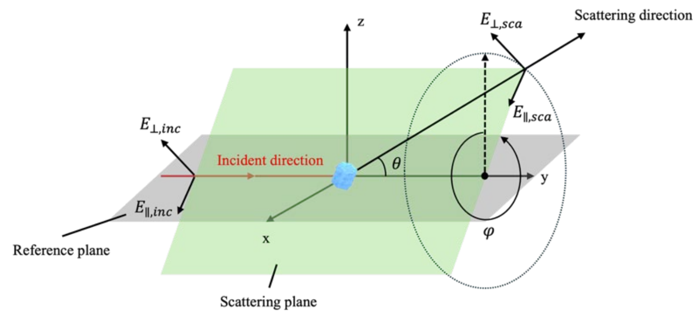

Fig. 2. Schematic illustration of the incident-scattering geometric configuration for light scattering by a general nonspherical particle.

If the incident and scattered electric vectors are decomposed into the components along the directions parallel and perpendicular to the scattering plane illustrated in Fig. 2, they are related in the following form:

$$\begin{bmatrix} E_{s,\parallel} \\ E_{s,\perp} \end{bmatrix} = \frac{\exp\,[ik(\xi - y)]}{-ik\xi} \boldsymbol{S} \begin{bmatrix} E_{i,\parallel} \\ E_{i,\perp} \end{bmatrix}, \tag{5a}$$

$$\boldsymbol{S} = \begin{bmatrix} S_2 & S_3 \\ S_4 & S_1 \end{bmatrix}, \tag{5b}$$

where ξ is the distance between the particle and the observer. Matrix $\boldsymbol{S}$ is referred to as the amplitude scattering matrix. In (5a), we implicitly assume that the temporal dependence of a harmonic electromagnetic wave is $e^{-i\omega t}$, where ω is the angular frequency. In (5b), we use a common notation for the $\boldsymbol{S}$ matrix elements, which was originally introduced by [25]. For a particle with rotational symmetry around the incident direction, the amplitude scattering matrix is a function of the scattering angle θ. For a general nonspherical particle, the amplitude scattering matrix depends on scattering angle θ and the rotation of the scattering plane around the incident direction with respect to a specific reference plane, specified by the azimuthal angle φ in Fig. 2. For a sphere, matrix $\boldsymbol{S}$ is diagonal, i.e., S_3 and S_4 are zero, and the analytical solutions to S_1 and S_2 are given by the famous Lorenz-Mie theory [6], [7] that is a milestone in the history of classical physics. The amplitude scattering matrix given in (5b) contains all information about the scattering and absorption properties of the scattering particle.

For a sphere or a collection of nonspherical particles under the random orientation condition with an equal number of mirror-image particles, the incident and scattered Stokes parameters are related by the following relation:

$$\begin{bmatrix} F_s \\ Q_s \\ U_s \\ V_s \end{bmatrix} = \frac{C_s}{4\pi\xi^2} \mathbb{P} \begin{bmatrix} F_i \\ Q_i \\ U_i \\ V_i \end{bmatrix}, \tag{6}$$

where $\mathbb{P}$ is called the scattering phase matrix. For a sphere, $\mathbb{P}$ is given in the form of

$$\mathbb{P} = \begin{bmatrix} P_{11} & P_{12} & 0 & 0 \\ P_{21} & P_{11} & 0 & 0 \\ 0 & 0 & P_{33} & P_{34} \\ 0 & 0 & -P_{34} & P_{33} \end{bmatrix}. \tag{7}$$

The scattering phase matrix averaged over a collection of nonspherical particles under the random orientation condition with an equal number of mirror-image orientations, is given by

$$\mathbb{P} = \begin{bmatrix} P_{11} & P_{12} & 0 & 0 \\ P_{21} & P_{22} & 0 & 0 \\ 0 & 0 & P_{33} & P_{34} \\ 0 & 0 & -P_{34} & P_{44} \end{bmatrix}. \tag{8}$$

From the comparison between (7) and (8), $P_{22} = P_{11}$ in the case of a sphere, whereas $P_{22} \neq P_{11}$ for general nonspherical particles; therefore, P_{22}/P_{11} is a quantity that can be used to indicate the nonsphericity of a scattering particle [26]. The elements of the scattering phase matrix can be directly calculated from the amplitude scattering elements. For example, P_{11}, also known as the phase function, can be given by

$$P_{11} = \frac{2\pi}{C_s k^2} \left(|S_1|^2 + |S_2|^2 + |S_3|^2 + |S_4|^2\right). \tag{9}$$

The phase function given in Eq. (9) is dimensionless and normalized in the form

$$\frac{1}{2}\int_0^{\pi} P_{11}(\theta) sin\theta d\theta = 1. \tag{10}$$

To illustrate the angular variation of the phase function, panels (a) and (b) of Fig. 3 show the phase function (P_{11}) and $-P_{12}/P_{11}$ (the degree of linear polarization of the scattered light, when the incident light is unpolarized such as natural sunlight) of a collection of water droplets specified in terms of the Gamma particle size distribution [27], which is referred to as a polydisperse medium. Panels (c) and (d) of Fig. 3 show the phase function and $-P_{12}/P_{11}$ of an ice crystal under the random orientation condition with an equal number of mirror-image orientations. In the case of light scattering by an ensemble of large water droplets, the scattering peaks corresponding to the primary rainbow, secondary rainbow, and glory are clearly shown in panel (a) of Fig. 3, whereas the 22° and 46° halo peaks are indicated in panel (c) of Fig. 3. Light scattering by nonspherical particles without symmetry in specific orientations is an advanced topic and will not be discussed in this paper. Briefly, the phase matrix may have 16 nonzero elements, and the extinction matrix rather than a scalar extinction cross section should be defined and used in radiative transfer simulations. Panels (e) and (f) of Fig. 3 show the phase function and $-P_{12}/P_{11}$ in the Rayleigh scattering regime where the size of the scattering particle is much smaller than the wavelength of the incident light, which is symmetric about the 90° scattering angle and is associated with strong linear polarization. Panels (g) and (h) of Fig. 3 show the phase function and $-P_{12}/P_{11}$ of dust aerosols represented in terms of a collection of randomly distorted hexahedral particles defined in the TAMUdust2020 dust optical property database [28]. The phase function of dust aerosols is relatively smooth, and the associated linear polarization is weak.

In many practical applications, it is computationally inefficient to explicitly account for the detailed phase function. Instead, the asymmetry factor, an integrated optical quantity, is often used, which is defined in the form

$$g = \frac{1}{2}\int_0^{\pi} P_{11}(\theta) cos\theta sin\theta d\theta. \tag{11}$$

The value of the asymmetry factor is between -1 and 1. In particular, the usual case is $g > 0$ when more energy is scattered into the forward angular hemisphere. $g < 0$ if more energy is scattered into the backward angular hemisphere, and this occurs when the scattering particle is embedded in an absorbing medium [29], [30]. For Rayleigh scattering, the asymmetry parameter is $g = 0$ because the scattering pattern is symmetric for the forward and backward hemispheres in the 4π scattering angular space.

With the asymmetry parameter, an analytical phase function referred to as the Henyey-Greenstein function $P_{11}(\theta)$ can be specified in the form

$$P_{11}(\theta) = \frac{1-g^2}{(1+g^2-2gcos\theta)^{3/2}}. \tag{12}$$

The Henyey-Greenstein function can be a reasonable surrogate for the realistic phase function in broadband flux computations in some cases (e.g., in the two-stream radiative transfer simulations, [31]), but it often leads to significant errors in remote sensing applications, particularly in retrieval algorithm implementations involving ice clouds and coarse-mode dust aerosols.

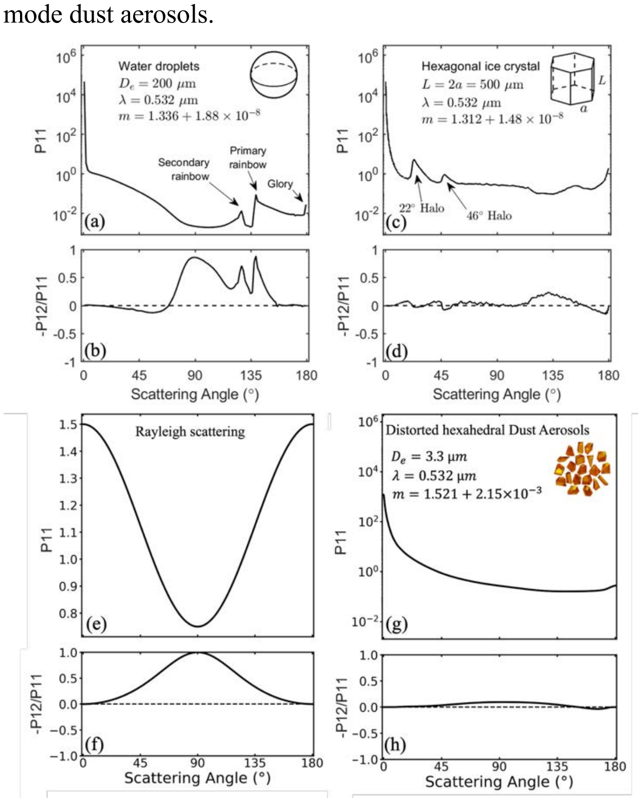

Fig. 3. Panels (a) and (b): The phase function and $-P_{12}/P_{11}$ (the degree of linear polarization of scattered light in the case of unpolarized incident light) of an ensemble of water droplets;

Panels (c) and (d): hexagonal ice crystals under the random orientation condition; Panels (e) and (f): Rayleigh scattering (lower-left panels); Panels (g) and (h): dust aerosols (lower-right panels). For water droplets, $D_e = 2r_e$, where r_e is the effective particle radius defined by (14) for an ensemble of polydisperse particles with various sizes specified in terms of the Gamma distribution (13). For nonspherical dust aerosols, the effective radius is defined based on Eq. (15) for an ensemble of 20 randomly distorted hexahedral particles, as explained in detail in [28].

In addition to the size and shape of a scattering particle, its scattering and absorption properties are highly sensitive to its complex refractive index ($m = m_r + im_i$). The imaginary part of the refractive index largely determines the absorption of light by the scattering particle. Figure 4 shows the refractive index of ice at temperatures 160, 210, and 270K and the refractive index of liquid water at temperatures 240, 270, and 300K [32], [33]. Although the present review focuses on the optical spectrum from the visible to the thermal IR, it is worth noting that the imaginary part of the refractive index of either ice or liquid water is sensitive to temperature in the far-IR (FIR)-to-microwave spectral regime. For water, the real part of the refractive index also strongly depends on temperature in the FIR-to-microwave spectral regime.

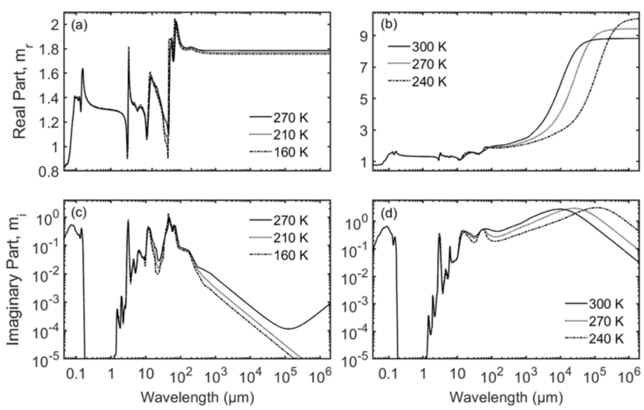

Fig. 4. The refractive indices of ice (left panels) at temperatures 160, 210, and 270K, and the refractive indices of liquid water (right panels) at temperatures 240, 270, and 300K at wavelengths from ultraviolet to microwave. Courtesy of Siheng Wang, Texas A&M University.

For practical applications in remote sensing, the bulk optical properties of particulate matter (e.g., a cloud or aerosol layer) containing polydisperse particles with various sizes depicted by the particle size distribution are needed. As an example, here we consider the bulk optical properties of water droplets in a low cloud. The particle size distribution can be specified in terms of the Gamma distribution in the form [27],

$$N(r)dr = N_0 r^{(1-3v_e)/v_e} e^{-r/r_e v_e} dr, \tag{13}$$

where r is the particle radius and N_0 is a constant. $N(r)dr$ denotes the number concentration (number of particles per unit volume) of the particles with radii between $(r - \frac{dr}{2})$ and $(r + \frac{dr}{2})$. In the above equation, v_e is the effective variance and is assumed to be 0.1 for water clouds, and r_e is the effective radius defined as the cross-section weighted average radius in the form [27]:

$$r_e = \frac{\int_{r_{min}}^{r_{max}} r\pi r^2 N(r)dr}{\int_{r_{min}}^{r_{max}} \pi r^2 N(r)dr} = \frac{\int_{r_{min}}^{r_{max}} r^3 N(r)dr}{\int_{r_{min}}^{r_{max}} r^2 N(r)dr}. \tag{14}$$

In the case of nonspherical particles (i.e., ice crystals in a cirrus cloud), the above definition can be generalized in terms of the ratio of total volume to total projected area [34], particularly in the form:

$$r_e = \frac{3}{4}\frac{\int_{r_{min}}^{r_{max}} V(r)N(r)dr}{\int_{r_{min}}^{r_{max}} A_p(r)N(r)dr}, \tag{15}$$

where r indicates half of the characteristic dimension of a nonspherical particle, V is the volume of the particle, and A_p is the projected area of the particle on a plane perpendicular to the incident radiation, the same as the counterpart in (2). The bulk optical properties, for example, the bulk phase function and extinction coefficient, can be defined as

$$P_{11} = \langle P_{11}(r)\rangle = \frac{\int_{r_{min}}^{r_{max}} P_{11}(r)C_s(r)N(r)dr}{\int_{r_{min}}^{r_{max}} C_s(r)N(r)dr}, \tag{16}$$

$$k_e = \int_{r_{min}}^{r_{max}} C_e(r)N(r)dr, \tag{17}$$

where $\langle\ \ \rangle$ denotes the average over the scattering particle population. The extinction coefficient k_e has units of inverse length, whereas the extinction cross-section has units of area. For a cloud layer with geometrical thickness Δz, the dimensionless optical thickness ($\Delta\tau$), a very important quantity in radiative transfer simulation, is defined as

$$\Delta\tau = k_e \Delta z. \tag{18}$$

It should be pointed out that r_e and $\Delta\tau$ are two important parameters in defining the microphysical properties of clouds. For example, the ice water path (IWP) associated with a vertically homogeneous ice cloud with a thickness of Δz can be expressed as

$$\begin{aligned} IWP &= \rho_{ice}\int V(r)N(r)dr \cdot \Delta z \\ &= \rho_{ice}\left[\frac{3}{4}\frac{\int V(r)N(r)dr}{\int A_p(r)N(r)dr}\right]\left[\frac{4}{3}\int Q_e(r)A_p(r)N(r)dr\right]\Delta z \\ &\times \frac{\int A_p(r)N(r)dr}{\int Q_e(r)A_p(r)N(r)dr} \\ &= \frac{4}{3\bar{Q}_e}\rho_{ice} r_e \Delta\tau, \end{aligned} \tag{19a}$$

$$\Delta\tau = \int Q_e(r)A_p(r)N(r)dr\ \Delta z, \tag{19b}$$

$$\bar{Q}_e = \frac{\int Q_e(r)AA_p(r)N(r)dr}{\int A_p(r)N(r)dr}, \tag{19c}$$

where ρ_{ice} is the mass density of ice, $\Delta\tau$ specifies cloud optical thickness, and $\bar{Q}_e$ is the mean extinction efficiency, averaged over the particle size distribution. In practice, $\bar{Q}_e \approx 2$ is a highly accurate approximation because ice crystals in ice clouds are predominately much larger than the wavelength of the incident radiation in the visible and thermal IR spectra. The importance of knowing the effective particle radius is further manifested by the use of this parameter in the cloud radiative property parameterizations in climate models. Specifically, the bulk mass extinction coefficient, single-scattering albedo, and asymmetry factor can be parameterized in the form ([35], and references cited therein):

$$\langle \frac{k_e}{IWC} \rangle = \frac{a_0 + a_1 r_e^{-1}}{1 + a_2 r_e^{-1} + a_3 r_e^{-2}}, \quad (20)$$

$$1 - \langle \tilde{\omega} \rangle = \sum_{n=0}^{n=4} c_n r_e^n, \quad (21)$$

$$\langle g \rangle = \sum_{n=0}^{n=4} d_n r_e^n, \quad (22)$$

where IWC denotes ice water content, and the coefficients $a_i, i = 0 - 3$, $c_i, i = 0 - 4$, and $d_i, i = 0 - 4$ are empirical coefficients determined by using the equations to fit the bulk optical properties computed for a range of effective radii.

Many methods have been developed to compute the single-scattering properties of an individual dielectric particle. Below we briefly encapsulate the basic concepts of several extensively used electromagnetic/light-scattering computational methods.

For light scattering by a dielectric particle, we can introduce an effective or equivalent conductivity to account for the absorption of light by the particle. In particular, the effective conductivity is zero and positive for nonabsorbing and absorbing particles, respectively. In this case, Maxwell's equations can be written as

$$\nabla \times \vec{H}(\vec{\xi}, t) = \frac{\varepsilon}{c} \frac{\partial \vec{E}(\vec{\xi}, t)}{\partial t} + \frac{4\pi}{c} \sigma \vec{E}(\vec{\xi}, t), \quad (23a)$$

$$\nabla \times \vec{E}(\vec{\xi}, t) = -\frac{1}{c} \frac{\partial \vec{H}(\vec{\xi}, t)}{\partial t}, \quad (23b)$$

$$\nabla \cdot \vec{E}(\vec{\xi}, t) = 0, \quad (23c)$$

$$\nabla \cdot \vec{H}(\vec{\xi}, t) = 0, \quad (23d)$$

where c is the speed of light in vacuum, and σ is the effective conductivity. We assume the permeability to be 1 for a non-ferromagnetic medium commonly encountered in atmospheric scattering research. We present the above form of Maxwell's equations in the Gaussian system for convenience in numerical computation. For example, $c\Delta t$ is the distance that an electromagnetic wave propagates in a time interval of Δt in the finite difference scheme used to solve the equations, as will be detailed in the following discussion. If we assume the temporal dependence of an electromagnetic wave to be time harmonic in the form of $e^{-i\omega t}$ (here ω is the angular frequency) and the complex index of refraction of the medium to be $m = m_r + i m_i$ (Note: The complex index of refraction is in the form $m = m_r - i m_i$, if the temporal dependence of a harmonic wave is selected as $e^{i\omega t}$), the frequency-domain form of (23a) is

$$\nabla \times \vec{H}(\vec{\xi}) = -i \frac{\omega}{c} \tilde{\varepsilon} \vec{E}(\vec{\xi}), \quad (24)$$

where $\tilde{\varepsilon} = \varepsilon + i 4\pi\sigma/\omega$ is the effective complex permittivity. Given that $\tilde{\varepsilon} = m^2$ [26], we have

$$\varepsilon = m_r^2 - m_i^2, \quad (25a)$$

$$\sigma = \frac{\omega}{2\pi} m_r m_i. \quad (25b)$$

Physically, the permittivity can be a complex quantity due to a complex electric susceptibility. The reader is referred to [36] for a detailed explanation. With the permittivity and effective conductivity specified in terms of the real and imaginary parts of the refractive index based on (25a) and (25b), one can use the finite-difference time-domain (FDTD) method to solve for the optical properties of a scattering dielectric particle [37], [38], [39]. Specifically, (23a) and (23b) can be discretized using the leap-frog finite-difference scheme as

$$\vec{E}^{n+1}(\vec{\xi}) = e^{-\eta\Delta t} \vec{E}^n(\vec{\xi}) + \frac{c\Delta t}{\varepsilon} e^{-\eta\Delta t/2} \nabla \times \vec{H}^{n+1/2}(\xi), \quad (26a)$$

$$\vec{H}^{n+1/2}(\vec{\xi}) = \vec{H}^{n-1/2}(\vec{\xi}) + c\Delta t \nabla \times \vec{E}^n(\vec{\xi}), \quad (26b)$$

where $\eta\Delta t = \frac{4\pi\sigma\Delta t}{\varepsilon} = 4\pi m_r m_i c\Delta t/[\lambda(m_r^2 - m_i^2)]$, and λ is the wavelength of interest.

It is obvious that the above introduction of the effective conductivity avoids using complex quantities in the FDTD simulation when the scattering particle is absorptive. To discretize (26a) and (26b), we can use the staggered grids shown in Fig.5, which were originally proposed by [37]. For practical light-scattering computations with the FDTD method, it is necessary to truncate the near-field spatial domain containing the particles by imposing an appropriate boundary condition such as the perfectly matching layer (PML) absorbing boundary condition [38], [40]. The near fields in the time domain can be converted to the counterparts in the frequency domain. Then, the near-field on the particle surface or within the particle can be mapped to the far fields to compute the optical properties of the particles. The technical details can be found in [38].

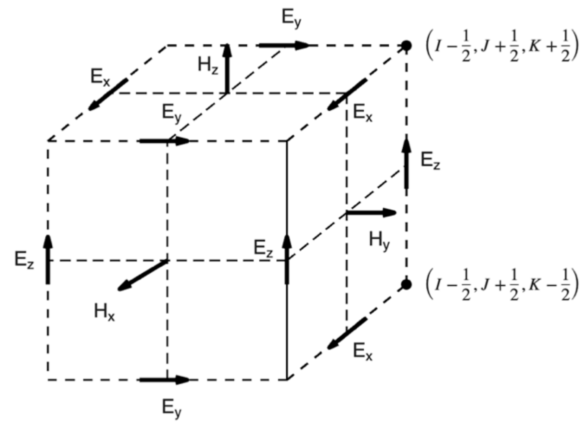

Fig. 5. Locations of the components of the electric and magnetic field vectors on a Cartesian cell, following a staggered finite-difference scheme developed originally by Yee [37].

Another widely used light-scattering computational method is the discrete dipole approximation (DDA) pioneered by [41]. In this method, a scattering dielectric particle is approximated as a collection of electric dipoles. Each of the dipoles responds to the sum of the incident field and the induced field due to other dipoles. The scattered field is the superposition of the induced fields by all the dipoles. DDA-based computational programs in the public domain have been developed [42], [43]. It should be pointed out that FDTD and DDA methods are limited to small-to-moderate size parameters, particularly in cases where the particle random orientation condition is concerned, and substantial computational effort is needed. The strengths of DDA and a variation or an improved form of FDTD, namely the pseudo-spectral time-domain (PSTD) method [44], are compared by [45].

Furthermore, with the choice of $e^{-i\omega t}$, the electromagnetic wave equation in the frequency domain is given as

$$\nabla^2 \vec{E}(\vec{\xi}) + \frac{\omega^2 m^2}{c^2} \vec{E}(\xi) = 0, \quad (27a)$$

$$\nabla^2 \vec{H}(\vec{\xi}) + \frac{\omega^2 m^2}{c^2} \vec{H}(\vec{\xi}) = 0. \quad (27b)$$

For coordinate-conforming geometries, particularly spheres and spheroids, the separation of variables method (SVM) can be used to solve (27a) and (27b) subject to the electromagnetic boundary conditions that the electric and magnetic fields are continuous across the particle surface. The SVM in the case of light scattering by a sphere, i.e., the Lorenz-Mie theory is a classic, which can be found in many texts and is not summarized here. [46] extended the SVM to spheroidal particles by expanding the fields in the spheroidal coordinate system using spherical harmonics. Unfortunately, their approach is not computationally robust and is limited to very small size parameters with moderate aspect ratios (Note: the aspect ratio is defined as the ratio of the equatorial radius to the semi-length of the axis of the rotational symmetry). Recently, [47], [48] further improved the SVM implemented in the spheroidal coordinate system by using the Wigner-d functions to stabilize the field expansion, developing a numerically robust algorithm to compute radial spheroidal functions, and using the Tikhonov regularization to overcome numerical instability. The improved SVM can be applied to size parameters as large as 1,000 for both homogeneous and two-layer spheroids. Figure 6 illustrates the domain of applicability of the improved SVM compared to the applicability of the previous SVM method reported in [46], the T-matrix method implemented with the extended boundary condition [49], and the invariant imbedding T-matrix method (IITM) [50], [51]. The applicability ranges of these methods depend slightly on the refractive index. The computations in Fig. 6 were performed with a refractive index of $1.53 + i5 \times 10^{-4}$. The aspect ratio of a spheroid is defined as a/c, where a and c are the semi-equatorial axis and the rotationally symmetric semi-axis lengths, respectively. a /c$<$ 1 and a /c$>$ 1 indicate a prolate and oblate spheroid, respectively. For very elongated spheroids with large size parameters, we found that the radial functions used in expanding the electromagnetic fields caused numerical instability, as illustrated in Fig. 6. The dimensionless size parameter in Fig. 6 is defined as ka for oblate spheroids and ka for prolate spheroids, where $k = 2\pi/\lambda$ with λ as the wavelength of the incident light. It deserves an endeavor in the future to stabilize the radial functions in numerical computation.

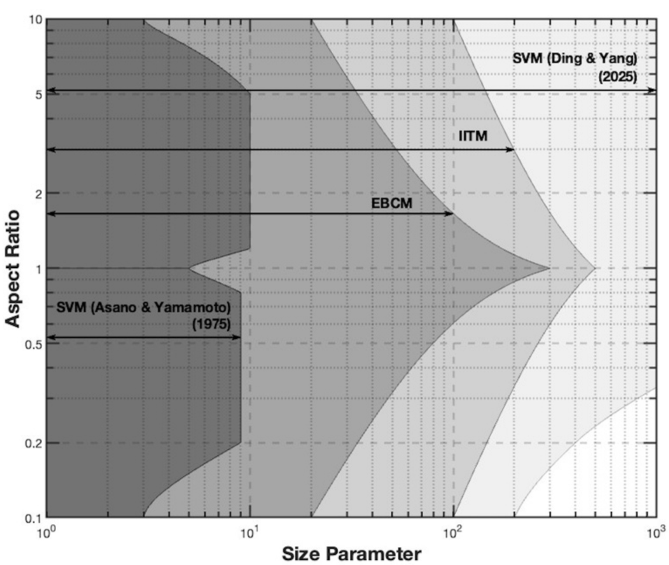

Fig. 6. The applicability domain in the aspect ratio and size parameter space of the original separation of variables method (SVM) [46], the T-matrix method based on the extended boundary condition method [49], IITM) [50], [51], and the improved SVM [47], [48].

The improved SVM has been combined with the T-matrix method (hereafter, the new method is referred to as SV-TM) to improve computational efficiency [52]. As an example, Fig. 7 shows the phase matrix computed by SV-TM for a prolate spheroid with a size parameter of *kc* = 2000 and an aspect ratio of *a/c*=0.6 under the random orientation condition. Figure 7 also shows the result computed with an improved geometric optics method (IGOM), a simplified version of the full physical-geometric optics method (PGOM) [53] that will be discussed in more detail. In IGOM, the phase interference of scattered waves is locally accounted for in terms of the ray spreading effect described in detail in [54]. The IGOM result agrees well with the SV-TM counterpart; however, the SV-TM phase function is larger than the IGOM counterpart in the 180° backscattering direction, and this difference may have implications for applications to lidar-based remote sensing.

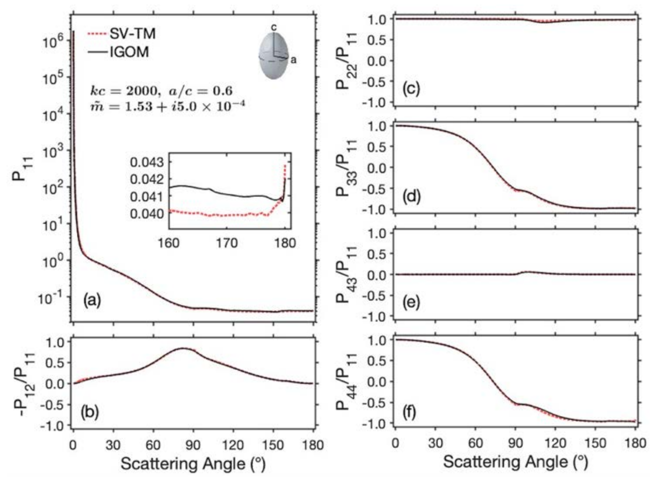

Fig. 7. The phase matrix of a prolate spheroid (*kc* = 2000 with an aspect ratio of *a/c*=0.6) computed by the SVM-TM and an improved geometric optics method (IGOM). Courtesy of Siheng Wang, Texas A&M University.

Spherical geometry offers only one degree of freedom (specifically, the particle size) but spheroidal geometry offers two degrees of freedom (specifically, the particle size and the aspect ratio— the ratio of the minor-axis length to the major-axis length). As a first-order approximation, the spheroidal model has been used to represent nonspherical particles in light-scattering computations and significant success has been achieved in various downstream remote sensing applications, for example, inference of dust aerosol properties [55]. Figure 8 illustrates that the simulated phase function and the degree of linear polarization of scattered light associated with unpolarized incident light, $-P_{12}/P_{11}$, based on the spheroidal model can match the experimental measurement of a feldspar dust sample [56]. In the simulation, the aspect ratios of spheroids range from 0.2 to 5 (Fig. 8c) with particle sizes, specified in terms of equivalent-volume spherical radius, from 0.076 to 12.88 μm (Fig. 8d). The selection of the particle size and aspect ratio is to optimize the agreement between the theoretical results and measurements, following the method in [55]. The results in Fig. 8 demonstrate that the spheroidal shape model can be used to approximately represent complex nonspherical particles in light-scattering computations, provided that the aspect ratios and sizes of the spheroids are appropriately selected.

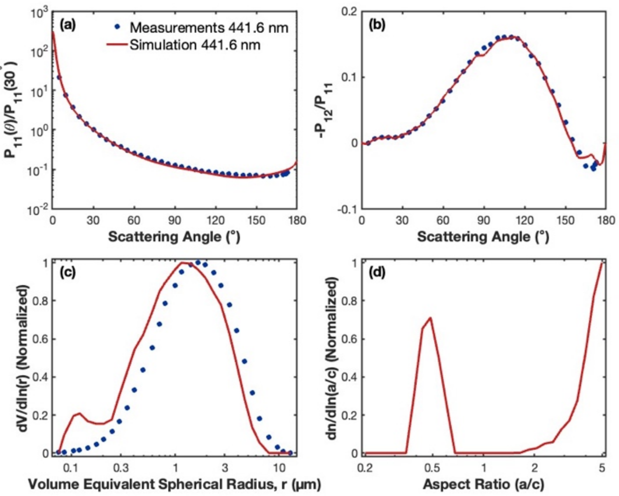

Fig. 8. The comparison of the simulated and measured phase functions. The spheroidal model is assumed to approximate the nonspherical particle geometries of a collection of feldspar dust particles. Courtesy of Siheng Wang, Texas A&M University.

At present, there is no single method that is applicable for light scattering with size parameters ranging from the Rayleigh scattering regime (when the particle size is much smaller than the wavelength of the incident light) to the geometric optics regime (when the particle size is much larger than the wavelength of the incident light) for general nonspherical particles. Fortunately, a synergistically unified method [53] based on combining IITM [50], [51] and PGOM [54], [57], [58] can be used to fill the gap in this regard. In particular, IITM is used for small-to-moderate size parameters and PGOM is used for moderate-to-large size parameters. At present, PGOM is limited to particles with facets or aggregates composed of convex elements. As a reasonable approximation, IGOM can be used for particles with curved surfaces.

In IITM, a particle is discretized in terms of a number of thin concentric inhomogeneous spherical shells, as shown in Fig. 9. The index of refraction may vary in the angular direction in each spherical layer defined in this form, i.e., the inhomogeneity of concentric spherical layers allows the feasibility of accounting for inhomogeneous particles in light-scattering computation. If the T-matrix from layer 1 to n-1, $T(\xi_{n-1})$, is known, then the T-matrix from layer 1 to n, $T(\xi_n)$, can be obtained through various volume-integration based matrix operations. In this manner, the T-matrix of the entire particle can be iteratively computed in a symbolic form of $T(\xi_{n-1}) \rightarrow T(\xi_n)$ through various volume-integration-based matrix operators. After the T-matrix is obtained, it is straightforward to compute the single-scattering properties. For example, the extinction and scattering cross sections for a scattering particle under the random orientation condition can be computed as follows [51]:

$$C_s = \frac{2\pi}{k^2}\sum_{l=1}^{L_{max}}\sum_{l'=1}^{L_{max}}\left(\left|T_{11}^{l,l'}\right|^2 + \left|T_{12}^{l,l'}\right|^2 + \left|T_{21}^{l,l'}\right|^2 + \left|T_{22}^{l,l'}\right|^2\right), \tag{28}$$

$$C_e = -\frac{2\pi}{k^2} Re\left[\sum_{l=1}^{L_{max}}\left(T_{11}^{l,l} + T_{22}^{l,l}\right)\right]. \tag{29}$$

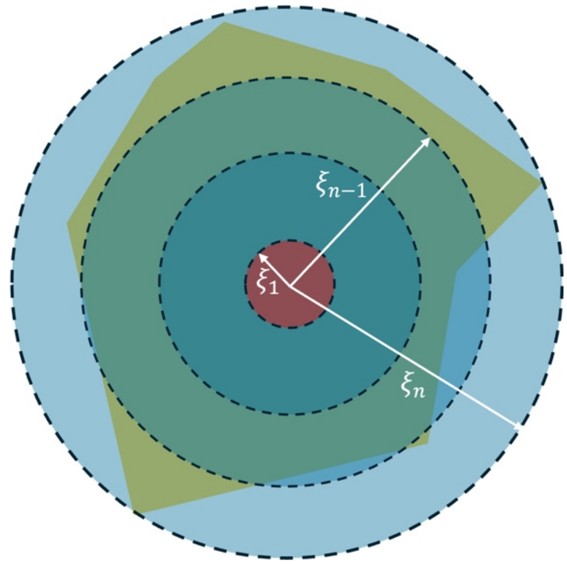

Fig. 9. Schematic illustration of the invariant-imbedding T-matrix method for light scattering computation.

In PGOM (Fig. 10), the wavefront of the incident wave is discretized as a number of localized waves, each of which is treated as a beam. The ray-tracing technique is then utilized to compute the electric and magnetic fields on the particle surface. The near field thus obtained is subsequently mapped to the far field (in the zone far away from the particle, or the radiation zone) based on an exact electromagnetic relation to compute the optical properties of the particle:

$$\vec{E}_s(\vec{\xi})|_{k\xi\rightarrow\infty} = \frac{e^{ikr}}{-ikr}\frac{k^2}{4\pi}\hat{\xi} \times \oiint_s \{\hat{n} \times \vec{E}(\vec{\xi}') - \hat{\xi} \times [\hat{n} \times \vec{H}(\vec{\xi}')]\} e^{-ik\hat{\xi}\cdot\vec{\xi}'} d^2\vec{\xi}'. \tag{30}$$

PGOM overcomes the significant shortcomings of the conventional geometric optics method (CGOM) for light-scattering computation. For example, the artificial separation of the diffraction and reflection-refraction contributions in CGOM is not required in PGOM, resulting in a more physically reasonable extinction efficiency. In addition, the singularity, namely the delta-transmission [59], which is inherent in CGOM in the case of a particle with parallel facets, is overcome in PGOM. An improved near-to-far-field mapping approach that applies PGOM to complex particle geometries, e.g., aggregates, based on a rectangular box enclosing the scattering particle has been developed [60]. Furthermore, the near-to-far-field mapping can be implemented using a volume-integral electromagnetic relation [61] based on the near-field within the scattering particle. In principle, the surface-integral and volume-integral equation-based methods are equivalent; differences arise in simulations for relatively small size parameters because the near-field approximations used in these two methods differ.

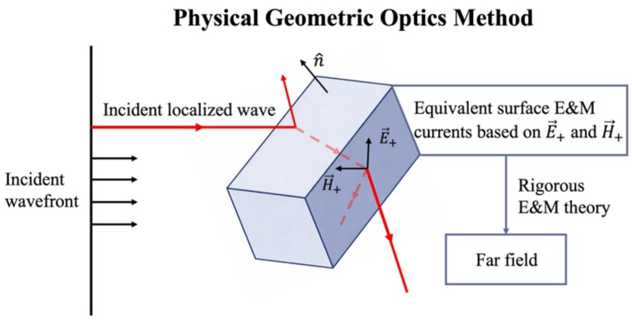

Fig. 10. Schematic diagrams for the physical geometric optics method (PGOM), illustrated with light scattering by a rectangular particle. The wavefront of the incident wave is discretized as many localized waves, which are treated as rays based on the principles of geometric optics. The equivalent surface E&M currents indicate the equivalent electric and magnetic currents on the particle surface [54].

As an example, Fig. 11 shows the nonzero elements of the phase matrix of a hexagonal ice crystal with size parameter kL=200 and aspect ratio 2a/L=1 under the random orientation condition. The PGOM and IITM results agree quite well even in the backscattering directions, particularly in the case of the phase function.

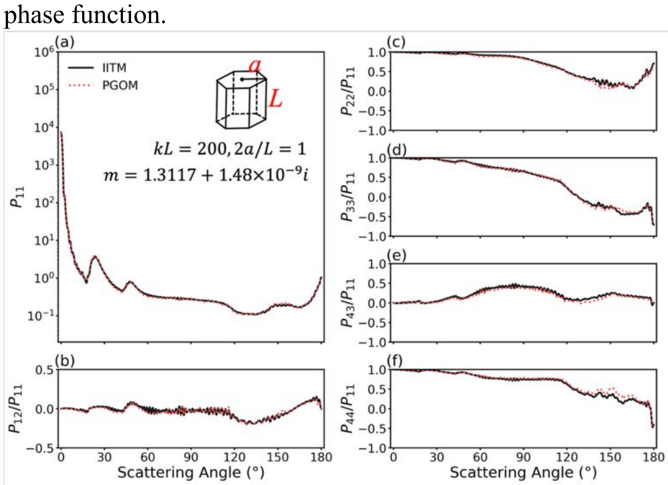

Fig. 11. Phase matrices computed by IITM and PGOM for a hexagonal column under the random orientation condition.

The principles of geometric optics are more valid for large than for small particles. Therefore, the accuracy of PGOM increases with increasing particle size, as PGOM uses the ray-tracing technique based on the principles of geometric optics to compute the near-field. Although IITM is a theoretically exact method except for very small errors in numerical implementation, it requires more computational resources with increasing particle size and becomes unfeasible for large particles. Figure 12 shows the extinction efficiency computed by the IITM and PGOM. At the size parameters near kL=~100, the two results overlap. The smooth transition between the IITM and PGOM leads to the concept of the synergistically unified method. Specifically, we can use the IITM for kL<~100 and PGOM for larger particles, as illustrated in the lowest portion of Fig. 12. In this manner, the synergistically unified method provides a practical approach to computing the optical properties across the entire size-parameter range. The synergistically unified method has been successfully employed to compute databases of the optical properties of nonspherical dust particles [62] and two-layer oceanic particles [63].

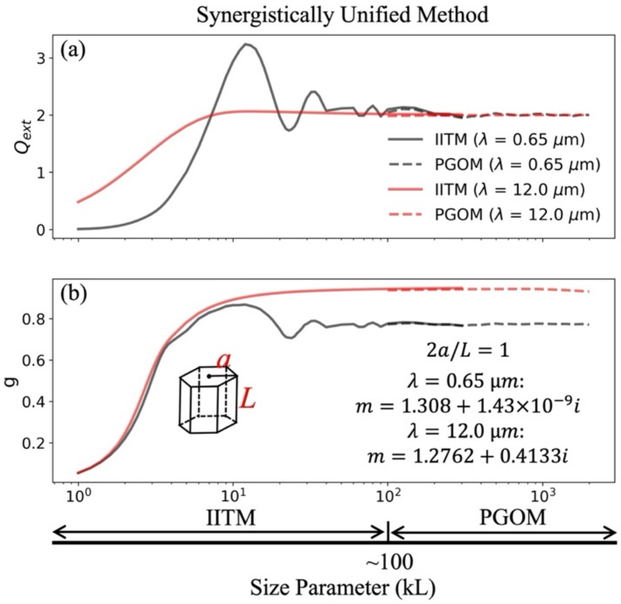

Fig. 12. Comparison of the (a) extinction efficiencies and (b) asymmetry factors computed by the IITM and PGOM; the schematic shown at the bottom illustrates the synergistically unified approach that combines IITM and PGOM for light-scattering computations.

With advanced light-scattering computational capabilities, it is feasible to develop optical property models for remote sensing, e.g., by generating look-up tables (LUTs). As an example, the upper panel of Fig. 13 shows the optical property model used for the MODIS Collection 6 ice cloud property product [16], in which ice crystals are assumed to be severely roughened aggregates with sizes following the Gamma distribution. The lower panel of Fig. 13 illustrates the ice cloud model used for the Clouds and the Earth's Radiant Energy System (CERES) Edition-4 ice cloud property retrievals [17].

Most recently, an advanced ice crystal habit model, referred to as the Passive-Active Remote Sensing Consistent (PARSC) model [64], was developed based on a mixture of three habits, namely an ensemble of irregular aggregates, hexagonal aggregates, and irregular hexagonal columns, with their percentages indicated by the green, red, and blue lines in Fig. 14a, respectively. Figure 14b shows the phase function for three effective particle sizes based on this model. This model ensures spectral consistency (Fig. 14c) between retrievals based on solar spectral bands and thermal IR bands. The lidar ratio and depolarization ratio calculated based on this model are consistent with observations made by the Cloud-Aerosol Lidar with Orthogonal Polarization (CALIOP) on board the Cloud-Aerosol Lidar and IR Pathfinder Satellite Observations (CALIPSO) platform [65], as illustrated by Fig. 14d, where the arrow indicates the variations of the lidar and depolarization ratio values calculated from the model as the effective radius increases from 5 to 60 μm.

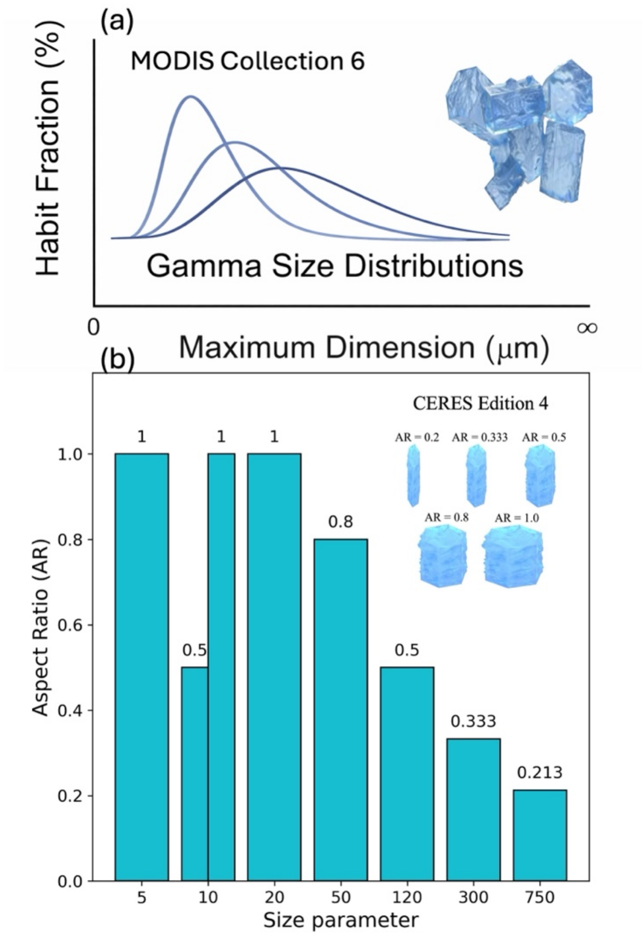

Fig. 13. (a) The ice crystal habit/shape model and size distribution used for the MODIS Collection -6 operational cloud property products [16]; (b) the ice crystal habit/shape and aspect ratio (AR) model used for CERES Edition -4 operational cloud property products [17].

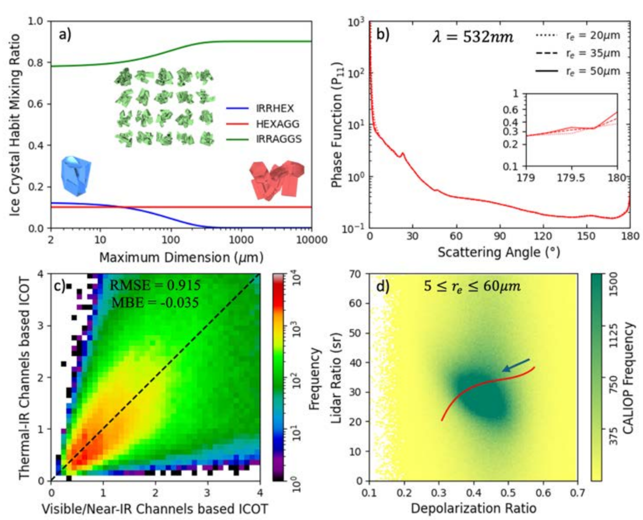

Fig. 14: a) A model habit/shape fraction distribution and ice particle geometry diagram for an ensemble of irregular aggregates (green line), hexagonal aggregates (red line), and irregular hexagonal columns (blue line) ice particles. b) Comparison between the 532nm bulk phase functions based on the ice cloud optical property model for three effective radii. c) 2D frequency plot of CALIOP-observed 532nm lidar and depolarization ratios of 4,787,728 identified tropical ice cloud cases over the ocean (30°S to 30°N) from Sept. 2006 to Dec. 2014. The line plots overlayed represent the lidar and depolarization ratios calculated from the bulk optical properties of the PARSC (red line) models using the equation. Courtesy of James Coy, Texas A&M University.

B. Absorption by Atmospheric Gases

The absorption of gases in the atmosphere substantially modulates the transfer of radiation in both solar and thermal IR spectral regimes. The atmospheric absorption spectrum comprises 10^5 or 10^6 lines of more than 20 gas species [66], arising from transitions between molecular energy levels that fall into four types: translational, electronic, vibrational, and rotational energies; the latter three are quantized. The spectroscopic parameters are provided by the HIgh-resolution TRansmission molecular AbsorptioN (HITRAN) molecular spectroscopic database with the latest version given by HITRAN 2024 [67].

An absorption line is not infinitesimally narrow; it is broadened by the Doppler effect and the collisions between the emitting molecule and other molecules. The Doppler line shape is given by

$$f_D(\upsilon-\nu_0)=\frac{1}{\alpha_D\sqrt{\pi}}exp\left[-\left(\frac{\upsilon-\nu_0}{\alpha_D}\right)^2\right], \tag{31}$$

where α_D determines the width of Doppler broadening. In particular, it can be shown that the half-width at half maximum of the line shape is $\sqrt{ln2}\alpha_D$. The line broadening due to collisions is specified by the Lorentz profile given by

$$f_L(\upsilon-\nu_0)=\frac{1}{\pi}\frac{\alpha_L}{(\upsilon-\nu_0)^2+\alpha_L{}^2}, \tag{32}$$

where α_L determines the Lorentz profile width. In the atmosphere, pressure broadening dominates in the lower atmosphere, particularly in the troposphere and boundary layer where gas densities are high, whereas Doppler broadening is significant in the upper atmosphere where gas densities are low and the speeds of molecule motion are large, particularly in the stratosphere and above. At an altitude between 20–50 km, both pressure broadening and Doppler broadening must be considered [68]. In this case, the line shape is given by the Voigt profile in the form

$$f_V(\upsilon-\nu_0)=\int_{-\infty}^{\infty}f_L(\upsilon'-\nu_0)\,f_D(\upsilon-\upsilon')d\upsilon'. \tag{33}$$

It can be shown that the Voigt profile reduces to the Lorentz profile or the Doppler profile when $\alpha_D\to 0$ or $\alpha_L\to 0$, respectively. Figure 15 shows the Doppler, Lorentz, and Voigt line shapes.

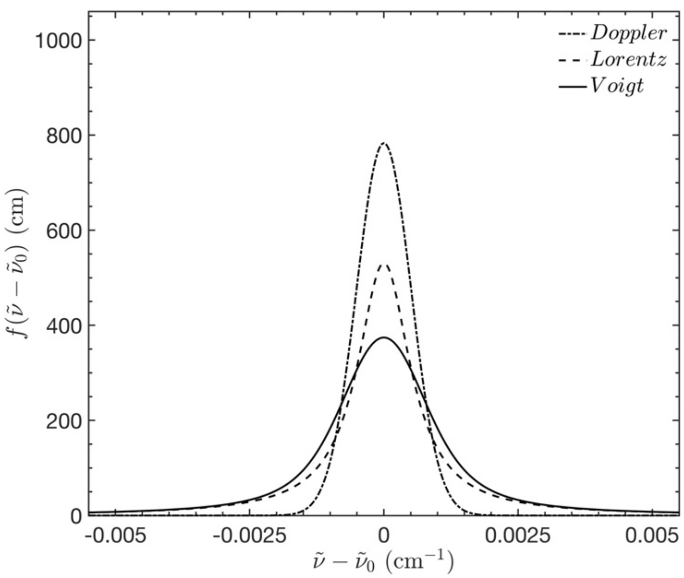

Fig. 15. Illustration of three types of the absorption line shape. The Doppler (dash-dot) and Lorentz (dashed) line shapes are shown with half-widths of $\alpha_D = 6 \times 10^{-4}\ cm^{-1}$ and $\alpha_L = 6 \times 10^{-4}\ cm^{-1}$, respectively. The Voigt line shape (solid line) represents the combined effect of Doppler and Lorentz broadening, using the same half-width values for both components: $\alpha_D = \alpha_L = 6 \times 10^{-4}\ cm^{-1}$.

Rigorous computation of gaseous absorption is the line-by-line computation [69], [70] that requires the spectral resolution be much smaller than the half widths of absorption lines. To improve computational efficiency, the correlated-k distribution (CKD) method [71] can be applied to a narrow band. To explain CKD, let us first explain the k-distribution applied to a homogeneous path length defined as

$$u = \int_0^S \rho_{abs} ds', \tag{34}$$

where ρ_{abs} indicates the mass density of the absorbing gas. The spectrally averaged transmissivity $\overline{\Gamma}(u)$ over spectral interval $\Delta\nu$ can be expressed in the form

$$\overline{\Gamma}(u) = \frac{1}{\Delta\nu}\int_{\Delta\nu} e^{-k(\nu)u} d\nu = \int_{k_{min}}^{k_{max}} e^{-ku} f(k) dk = \int_0^1 e^{-k(G)u} dG, \tag{35}$$

where k *is* mass absorption coefficient. k_{min} and k_{max} are the minimum and maximum values of k within $\Delta\nu$, respectively. $f(k)$ is referred to as the normalized probability distribution, indicating the fraction of $\Delta\nu$, where the mass absorption coefficient is between $k - dk/2$ and $k + dk/2$. G is the cumulative probability function, defined as

$$G(k) = \int_0^k f(k') dk'. \tag{36}$$

The absorption coefficient highly varies in the wavenumber domain, while it is smooth in the *G* domain, as illustrated by Fig. 16. Therefore, a few quadrature points may be sufficient to compute the spectrally averaged transmissivity if the computation is performed in the *G* domain.

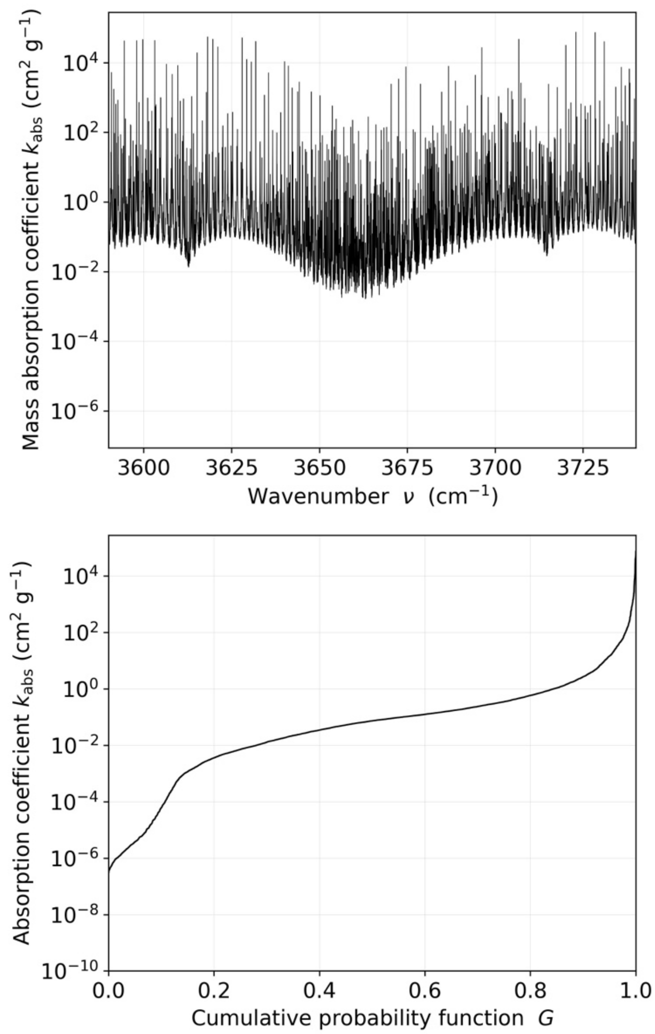

Fig. 16. The upper panel shows the mass absorption coefficients ($cm^2\ g^{-1}$) for CO_2 between 3590 and 3790 cm^{-1} at an air temperature of 260.0 K and a pressure of 1.2 hPa. The lower panel shows the cumulative Probability Function *G* versus absorption coefficient ($cm^2\ g^{-1}$). Courtesy of Jian Wei, Texas A&M University.

CKD is an extension of the *k*-distribution to an inhomogeneous path with the variations of the absorption strength as a function of pressure and temperature. Specifically, CKD assumes that the ordering of the strengths of absorption lines at pressure *P* and temperature *T* is the same as that at reference pressure P_r and temperature T_r, although this assumption is not exactly true. Fu and Liou [72] established the conditions for the validity of CKD.

When the CKD is applied to the computation of the spectrally averaged transmissibility associated with an instrument band, the spectral response function of the measuring instrument should be included [73]. A practically feasible approach has been developed by [74]. In particular, the spectral fraction involved in computing $f(k)$ should be weighted by the normalized spectral response function of the instrument.

Hyperspectral spaceborne sensors, such as the Atmospheric Infrared Sounder (AIRS) [75] and the Infrared Atmospheric Sounding Interferometer (IASI) [76] make observations in thousands of spectral channels, providing a wealth of information on atmospheric composition, clouds, aerosols, and surface properties. To fully exploit this hyperspectral data in real-time applications, the principal component-based radiative transfer model (PCRTM) [77], [78] has been developed to significantly reduce the computational burden encountered by the conventional line-by-line computation. Specifically, PCRTM exploits the high degree of spectral correlation inherent in the hyper-spectra. This method applies Principal Component Analysis (PCA) via Singular Value Decomposition (SVD) to compress thousands of spectral channels into a small set of orthogonal Principal Components (PCs). During an offline training process, an ensemble of representative atmospheric radiance spectra is decomposed so that typically the first 100 to 150 PCs capture more than 99.9% of total spectral variance. The remaining computational effort at runtime is simply to predict the PC scores that are the linear coefficients involved in reconstructing the full spectrum from the prestored PCs. Liu et al. [79] extended the PCRTM framework to the solar spectrum by including multiple scattering effects, the bidirectional reflectance distribution function of the surface, and the wavy sea-surface reflection. The interested reader is referred to [78], [79] for the technical details of PCRTM and [80], [81] for the optical property-based PCA approach.

C. Radiative Transfer in the Atmosphere

Knowing particle single-scattering properties is not sufficient for inferring cloud and aerosol properties from remote sensing measurements, and we must consider multiple scattering of a collection of particles, i.e., the radiative transfer process involving a cloud or aerosol layer, or the transfer of IR radiation under non-scattering atmospheric conditions to infer cloud-top pressures. The scalar radiative transfer equation, without consideration of the polarization state of the radiation field, is given by

$$\mu\frac{\partial I_\lambda(\tau,\mu,\varphi)}{\partial\tau} = I_\lambda(\tau,\mu,\varphi) - \frac{\widetilde{\omega}_\lambda}{4\pi}\int_0^{2\pi}\int_0^{\pi} P_{11,\lambda}(\tau,\mu,\varphi,\mu',\varphi')I_\lambda(\tau,\mu',\varphi')\,d\mu' d\varphi' - \frac{\widetilde{\omega}_\lambda}{4\pi}S_{0,\lambda}e^{-\frac{\tau}{\mu_0}}P_{11,\lambda}(\tau,\mu,\varphi,-\mu_0,\varphi_0) - (1-\widetilde{\omega}_\lambda)B_\lambda, \quad (37)$$

where we use spherical coordinates (θ,φ) and (θ',φ') to indicate the propagation directions of the scattered and incident radiation beams, respectively. τ is the optical thickness, $\mu = cos\theta$, $\mu' = cos\theta'$, $\widetilde{\omega}_\lambda$ is the spectral single-scattering albedo, $S_{0,\lambda}$ is spectral solar irradiance on a plane perpendicular to the incoming sunlight at TOA, and B_λ is the spectral Planck function for the terrestrial thermal emission.

In essentially all the textbooks on radiative transfer, the linkage between single scattering and multiple scattering, i.e., the derivation of the second and third terms on the right-hand side of (37) from the first Stokes parameter in (6), is not explicitly explained. Furthermore, the same symbol (e.g., "I" in [68]) is used for both the first Stokes parameter and radiance, leading to potential confusion, particularly for those who have newly entered the field of single scattering and radiative transfer. To clarify the confusion, let us rewrite the governing equation for the first Stokes parameter (Note: the extension of the following derivation to the full Stokes vector is straightforward) as follows:

$$F_{\lambda,s}(\vec{\xi}_2,r,\theta,\varphi) = \frac{C_{\lambda,s}(\vec{\xi}_1,r)}{4\pi\left|\vec{\xi}_2-\vec{\xi}_1\right|^2}P_{\lambda,s}(\vec{\xi}_1,r,\theta,\varphi,\theta',\varphi')F_{\lambda,i}(\vec{\xi}_1,\theta',\varphi'), \quad (38)$$

where we add the subscript λ to indicate the spectral dependence of the relevant quantities. $\vec{\xi}_1$ and $\vec{\xi}_2$ denote the positions of the scattering particle and the observer, respectively. The above equation stems from Maxwell's equations and does not involve solid angle. In the Systèm International d'Unités (SI), $F_{\lambda,s}$ and $F_{\lambda,i}$ are given by [82]

$$F_{\lambda,s} = \frac{1}{2}\sqrt{\frac{\varepsilon_0}{\mu_0}}\left(E_{\lambda,s,\parallel}E^*_{\lambda,s,\parallel} + E_{\lambda,s,\perp}E^*_{\lambda,s,\perp}\right), \quad (39a)$$

$$F_{\lambda,i} = \frac{1}{2}\sqrt{\frac{\varepsilon_0}{\mu_0}}\left(E_{\lambda,i,\parallel}E^*_{\lambda,i,\parallel} + E_{\lambda,i,\perp}E^*_{\lambda,i,\perp}\right), \quad (39a)$$

where ε_0 and μ_0 are the permittivity and permeability of vacuum, respectively. The subscripts $\parallel$ and $\perp$ indicate the parallel and perpendicular components of the electric vector with respect to the plane, to which the Stokes parameter is defined in reference. The superscript * indicates complex conjugate. In SI, $F_{\lambda,s}$ and $F_{\lambda,i}$ have units of $Wm^{-2}\mu m^{-1}$, while I_λ in Eq. (37) has units of $Wm^{-2}Sr^{-1}\mu m^{-1}$, where μm^{-1} denotes the spectral dependence. It should be pointed out that $F_{\lambda,s}$ decreases with increasing the distance between the scattering particle and the observer, while radiance I_λ is an invariant quantity in a non-absorbing homogeneous medium.

Let us consider a small volume $\Delta V = \Delta A dL$, where ΔA and dL are perpendicular and along the scattering direction pointing to the observer. Therefore, the solid angle subtended by this volume element, as viewed from the observer, is given by

$$\Delta\Omega = \frac{\Delta A}{\left|\vec{\xi}_2-\vec{\xi}_1\right|^2}. \quad (40)$$

Furthermore, the number of particles within ΔV is given by

$$\mathbb{N} = \Delta V\int N(r)dr, \quad (41)$$

where $N(r)dr$ specifies the particle size distribution given by (13) or a different size distribution form.

We assume that the particles within ΔV are randomly distributed and that the distances between them are much larger than the wavelength of the incident light. As a result, the particles are uncorrelated in space, and the phase interference among the scattered electromagnetic waves originating from different particles is nonconstructive, and the corresponding Stokes parameters can be linearly summed. Therefore, from (38) and (41), we obtain

$$\mathbb{N}F_{\lambda,s}(\vec{\xi}_2,\theta,\varphi)$$
$$=\frac{F_{\lambda,i}(\vec{\xi}_1,\theta',\varphi')}{4\pi}\frac{\Delta V}{|\vec{\xi}_2-\vec{\xi}_1|^2}\int C_{\lambda,s}(\vec{\xi}_1,r)P_{\lambda,s}(\vec{\xi}_1,r,\theta,\varphi,\theta',\varphi')\,N(r)dr$$
$$=\frac{F_{\lambda,i}(\vec{\xi}_1,\theta',\varphi')dL}{4\pi}\frac{\Delta A}{|\vec{\xi}_2-\vec{\xi}_1|^2}$$
$$\times\frac{\int C_{\lambda,s}(\vec{\xi}_1,r)P_{\lambda,s}(\vec{\xi}_1,r,\theta,\varphi,\theta',\varphi')\,N(r)dr}{\int C_{\lambda,s}(\vec{\xi}_1,r)\,N(r)dr}$$
$$\times\frac{\int C_{\lambda,s}(\vec{\xi}_1,r)\,N(r)dr}{\int N(r)dr}$$
$$\times\int N(r)dr$$
$$=\frac{F_{\lambda,i}(\vec{\xi}_1,\theta',\varphi')ds}{4\pi}\Delta\Omega P_{\lambda,s}(\vec{\xi}_1,\theta,\varphi,\theta',\varphi')C_{\lambda,s}(\vec{\xi}_1)\,\mathbb{N}/\Delta V, \qquad (42)$$

where $F_{\lambda,s}(\vec{\xi}_2,\theta,\varphi)$, $P_{\lambda,s}(\vec{\xi}_1,\theta,\varphi,\theta',\varphi')$ and $C_{\lambda,s}(\vec{\xi}_1)$ are the bulk Stokes parameter, phase function and the scattering cross section averaged over the particle population within the volume element ΔV, given by

$$F_{\lambda,s}(\vec{\xi}_2,\theta,\varphi)=\langle F_{\lambda,s}(\vec{\xi}_2,r,\theta,\varphi)\rangle=\frac{\int F_{\lambda,s}(\vec{\xi}_2,r,\theta,\varphi)N(r)dr}{\int N(r)dr}, \qquad (43a)$$
$$P_{\lambda,s}(\vec{\xi}_1,\theta,\varphi,\theta',\varphi')=\langle P_{\lambda,s}(\vec{\xi}_1,r,\theta,\varphi,\theta',\varphi')\rangle$$
$$=\frac{\int C_{\lambda,s}(\vec{\xi}_1,r)P_{\lambda,s}(\vec{\xi}_1,r,\theta,\varphi,\theta',\varphi')N(r)dr}{\int C_{\lambda,s}(r)N(r)dr}, \qquad (43b)$$
$$C_{\lambda,s}(\vec{\xi}_1)=\frac{\int C_{\lambda,s}(\vec{\xi}_1,r)N(r)dr}{\int N(r)dr}. \qquad (43c)$$

Equations (42), (43a), (43b), and (43c) logically define the bulk Stokes parameter, phase function, and scattering cross section. The bulk scattering coefficient $k_{\lambda,s}$ with units of m^{-1} in SI is then given by

$$k_{\lambda,s}(\vec{\xi}_1)=C_{\lambda,s}(\vec{\xi}_1)\mathbb{N}/\Delta V. \qquad (44)$$

According to the definition of radiance [68], which is invariant along a radiation beam in a nonabsorbing homogeneous medium, the scattered radiance contributed by the volume element is given by

$$\Delta I_{\lambda,s}(\vec{\xi}_1,\theta,\varphi)=\Delta I_{\lambda,s}(\vec{\xi}_2,\theta,\varphi)=\mathbb{N}F_{\lambda,s}(\vec{\xi}_2,\theta,\varphi)/\,\Delta\Omega. \qquad (45)$$

Therefore, (42) can be rewritten as

$$\Delta I_{\lambda,s}(\vec{\xi}_1,\theta,\varphi)=\frac{K_{\lambda,s}(\vec{\xi}_1)dL}{4\pi}P_{\lambda,s}(\vec{\xi}_1,\theta,\varphi,\theta',\varphi')F_{\lambda,i}(\vec{\xi}_1,\theta',\varphi')$$
$$=\frac{K_{\lambda,s}(\vec{\xi}_1)dL}{4\pi}P_{\lambda,s}(\vec{\xi}_1,\theta,\varphi,\theta',\varphi')I_{\lambda,i}(\vec{\xi}_1,\theta',\varphi')\Delta\Omega', \qquad (46)$$

where we use the following relation

$$F_{\lambda,i}(\vec{\xi}_1,\theta',\varphi')=I_{\lambda,i}(\vec{\xi}_1,\theta',\varphi')\Delta\Omega'. \qquad (47)$$

In (47), $I_{\lambda,i}(\vec{\xi}_1,\theta',\varphi')$ is the incident radiance observed at the location of the volume element ΔV. $\Delta\Omega'$ is the solid angle subtended by the volume element, as viewed from the source point of the incident radiation along the direction (θ',φ'). After we consider the contributions of the incident radiation from all directions, the scattered radiance due to the multiple scattering effect is given by

$$dI_{\lambda,s}(\vec{\xi}_1,\theta,\varphi)=$$
$$\frac{K_{\lambda,s}(\vec{\xi}_1)dL}{4\pi}\int_0^{2\pi}\int_0^{\pi}P_{\lambda,s}(\vec{\xi}_1,\theta,\varphi,\theta',\varphi')I_{\lambda,i}(\vec{\xi}_1,\theta',\varphi')\sin\theta'\mathrm{d}\theta'\mathrm{d}\varphi'. \qquad (48)$$

If we include the extinction, multiple scattering, and emission, the equation of radiative transfer is given by

$$dI_{\lambda}(\vec{\xi},\theta,\varphi)=-k_{\lambda,e}(\vec{\xi})I_{\lambda}(\vec{\xi},\theta,\varphi)\,dL$$
$$+\frac{k_{\lambda,s}(\vec{\xi})dL}{4\pi}\int_0^{2\pi}\int_0^{\pi}P_{\lambda,s}(\vec{\xi},\theta,\varphi,\theta',\varphi')I_{\lambda,i}(\vec{\xi},\theta',\varphi')\sin\theta'\mathrm{d}\theta'\mathrm{d}\varphi'$$
$$+k_{\lambda,a}(\vec{\xi})dLB_{\lambda}[T(\vec{\xi})], \qquad (49)$$

where $k_{\lambda,e}$ and $k_{\lambda,a}$ are the extinction and absorption coefficients in units of m^{-1}. On the right-hand side, the first term represents the Beer-Bouguer-Lambert law for radiation attenuation due to extinction, the second term denotes the increase in radiance due to multiple scattering, and the third term is the thermal emission contribution.

If we assume that the atmosphere is plane-parallel, i.e., the spatial dependence of the physical quantities is only on height z, (49) can be written as

$$\mu\frac{\partial I_{\lambda}(\tau,\mu,\varphi)}{\partial\tau}$$
$$=I_{\lambda}(\tau,\mu,\varphi)$$
$$-\frac{\tilde{\omega}}{4\pi}\int_0^{2\pi}\int_0^{\pi}P_{\lambda,s}(\mu,\varphi,\mu',\varphi')I_{\lambda,i}(\tau,\mu',\varphi')\mathrm{d}\mu'\mathrm{d}\varphi'$$
$$-(1-\tilde{\omega})B_{\lambda}[T(\tau)], \qquad (50)$$

where we use

$$\mu=cos\,\theta,\ \text{ and } \mu'=cos\theta'. \qquad (51a)$$
$$dL=dz/\mu, \qquad (51b)$$
$$\tilde{\omega}=k_{\lambda,s}/k_{\lambda,e}, \qquad (51c)$$
$$d\tau=-k_{\lambda,e}dz, \qquad (51d)$$

The radiance in (50) is the total (direct plus diffuse) radiance, given by

$$I_{\lambda,\text{total}}(\tau,\mu,\varphi)=I_{\lambda,\text{diffuse}}(\tau,\mu,\varphi)$$
$$+S_{0,\lambda}e^{-\tau/\mu_0}\delta[\mu-(-\mu_0)]\,\delta(\varphi-\varphi_0), \qquad (52)$$

where $\delta(\,)$ denotes the Dirac delta function. Substituting (52) into (50), we can obtain the equation of radiative transfer for diffuse radiation, given by (37).

If the optical thickness of a cloud (e.g., a thin cirrus cloud) or aerosol layer is small in the solar spectrum, single scattering events dominate. In this case, the bidirectional reflection function is given by

$$R_{\lambda}(\mu,\mu_0,\varphi-\varphi_0)=\pi I_r(\mu,\varphi)/\mu_0 S_{0,\lambda}$$
$$\approx\frac{\tilde{\omega}\Delta\tau}{4\mu\mu_0}P_{11}(\mu,-\mu_0,\varphi-\varphi_0)\text{ if }\Delta\tau\ll 1, \qquad (53)$$

where the geometric parameters μ_0 and φ_0 specify the incoming solar radiation angles. The above result underscores the importance of the phase function, as the inference of cloud and aerosol properties relies on the observed bidirectional reflection function. In (53), the effect of the surface reflection is not included. Using the adding principle, it is straightforward to show that the bidirectional reflection function, including the effect of a cloud/aerosol layer and the contribution of the surface reflection, is given by

$$\tilde{R}_{\lambda}(\mu,\mu_0,\varphi-\varphi_0)=R_{\lambda}(\mu,\mu_0,\varphi-\varphi_0)+$$
$$\frac{(t+e^{-\frac{\Delta\tau}{\mu}})R_S(t+e^{-\Delta\tau/\mu_0})}{1-R_S\bar{R}}, \qquad (54)$$

where t and $\bar{R}$ represent the diffuse transmissivity and reflectivity of the cloud/aerosol layer, respectively, and R_s is the surface reflectivity.

In the terrestrial thermal IR regime, (37) can be significantly simplified if the multiple scattering effect can be neglected. In this case, the upward radiance at a nadir view can be given as

$$I_\lambda(0) = B_\lambda(T_s)e^{-\tau_s} + \int_0^{\tau_s} B_\lambda[T(\tau')]e^{-\tau'}\,d\tau'$$
$$= B_\lambda(T_s)\Gamma[\tau(P_s)] + \int_{P_s}^{0} B_\lambda[T(\mathrm{P})]\frac{\partial\Gamma[\tau\prime(\mathrm{P})]}{\partial lnP}\,dlnP, \tag{55}$$

where $\Gamma(\tau') = e^{-\tau'}$ is the transmissivity, and $\frac{\partial\Gamma[\tau\prime(\mathrm{P})]}{\partial lnP}$ is referred to as the weighting function. Figure 17 shows examples of the weighting functions at seven wavelengths in the CO_2 15-μm absorption band, demonstrating the sensitivity of the TOA IR radiances to atmospheric temperatures across various atmospheric layers. Specifically, a spectral channel at the band center is sensitive to the very top portion of the atmosphere, while the radiance is more sensitive to the lower atmosphere as the channel moves toward the band wing, as demonstrated by the weighting functions in the right panel of Fig. 17. This spectral dependence of weighting functions on height in the atmosphere provides the physical basis for temperature soundings [83], [84], [85].

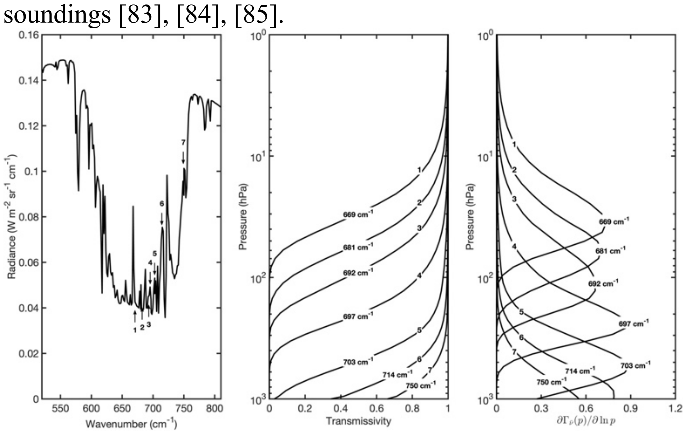

Fig. 17. Example illustrating (left) the outgoing radiance near the 15 μm CO_2 band simulated by the Line-By-Line Radiative Transfer Model (LBLRTM; Clough et al., 2005), with arrows indicating the spectral positions sampled at 669, 681, 692, 697, 703, 714, and 750 cm^{-1}; (middle) the corresponding transmissivity; and (right) the associated weighting functions. Courtesy of Jian Wei, Texas A&M University.

The physical fundamentals reviewed above, including particle single scattering, gaseous absorption, and multiple-scattering radiative transfer, form the theoretical foundation for the satellite remote sensing associated retrievals. In practice, different retrieval techniques exploit different portions of the electromagnetic spectrum. These techniques also utilize distinct sensitivities to cloud and aerosol optical, microphysical, and thermodynamic phase properties.

III. CLOUD MASK DETERMINATION

The previous section reviews the physical fundamentals of light scattering by particles, gaseous absorption, and radiative transfer processes in the atmosphere, which are essential for implementing remote sensing techniques. However, in the practical implementation of a retrieval algorithm to infer cloud and aerosol properties, the first step is to determine whether a pixel of interest is covered by clouds, a procedure known as cloud mask determination. It is worth noting that aerosol property retrieval is usually not performed for cloudy scenes.

As cloud mask determination is a prerequisite step for many downstream satellite retrievals and derived products, it must be performed accurately and robustly while ensuring computational efficiency for near-real-time processing under constraints on CPU time and data volume. Cloud detection from passive satellite radiances is often posed as a contrast problem because clouds are typically brighter (higher reflectance) and colder than the underlying surface, making visible and IR-window threshold methods effective under many conditions. However, this characterization can be challenging in several common situations, particularly over surface snow and ice, and for low-contrast cloud regimes such as thin cirrus clouds, fog and nighttime low stratus clouds, small-scale cumulus clouds, and mixed or partly cloudy satellite pixels near cloud edges, where cloud–surface radiance differences are weak or inherently ambiguous. Below, we specifically discuss the cloud mask algorithm developed by the MODIS cloud science team; however, many of the general techniques described below are applicable to other satellite cloud mask determination algorithms that use similar spectral channels.

To address scenes with the aforementioned ambiguities, the MODIS cloud mask uses a multispectral strategy enabled by its 36 channels and supplements spectral tests with spatial-uniformity information to better distinguish cloudy from clear-sky conditions. The overall approach integrates robust spectral tests with established elements from earlier cloud-screening methods, and its development is closely associated with community efforts within the MODIS Science Teams [86]. The cloud mask product indicates whether a given satellite view of the surface is unobstructed by clouds or by optically thick aerosol, and it is generated at 250 m and 1 km resolutions from calibrated, geolocated radiances. The retrieval uses a defined subset of MODIS bands spanning the visible-to-thermal IR spectrum. Missing or degraded radiometric inputs can reduce product quality, while invalid or missing geolocation prevents the generation of a valid result.

The MODIS cloud mask algorithm builds on prior cloud-detection systems developed for global cloud climatologies and operational satellite processing. In the ISCCP approach, narrowband visible (0.6 μm) and IR-window (11 μm) radiances are evaluated relative to clear-sky composite values, and a pixel is identified as cloudy when the difference between the observed and clear-sky radiances exceeds the uncertainty associated with the clear-sky radiance estimates [87], [88], [89], [90]. This logic is predicated on the separability of clear and cloudy radiance regimes and is biased toward clear-sky identification, which can lead to missed detections for clouds with weak radiometric contrast. The Advanced Very High Resolution Radiometer (AVHRR) schemes such as the AVHRR Processing scheme Over cLoud Land and Ocean (APOLLO) and the (Cloud Advanced Very High Resolution Radiometer-x (CLAVR-x) extend this logic with explicit multispectral thresholds and moving-window variability checks to capture partial cloud and small-scale structure [91], [92], [93], [94], [95], while Cloud and Surface Parameter Retrieval (CASPR) adapts similar concepts for polar scenes using radiative-transfer-based threshold selection and cloud-type-specific screening [96], [97]. Complementary methods for high-cloud detection use the CO_2 slicing technique in the CO_2 15-μm absorption band to infer cloud level and effective cloud amount, thereby improving sensitivity to transmissive high clouds relative to opaque clouds and clear sky. This technique is described in more detail in Section 5. Related methods are used in sounder-based cloud screening with instruments such as the High resolution Infrared Radiation Sounder (HIRS), the Advanced Television and infrared observation satellite Operational Vertical Sounder (ATOVS), and in the Geostationary Operational Environmental Satellite (GOES) sounder algorithms that integrate multispectral radiances with contextual tests based on neighboring pixels [23], [98], [99], [100], [101]. MODIS generalizes this heritage by combining broader spectral coverage with higher spatial sampling (including 250 m and 500 m visible/NIR measurements and 1 km elsewhere), enabling a multi-test, multi-scale mask intended to improve discrimination in known low-contrast and heterogeneous conditions.

A. Algorithm Description for Cloud Mask Determination

The cloud mask algorithm employs a staged decision framework that adapts to scene type and illumination. It applies a set of spectral and spatial-variability tests appropriate to the prevailing surface and viewing geometry, converts the outcome of each test into a clear-sky confidence metric, and combines these metrics to produce an initial cloud-mask estimate. When the initial estimate indicates ambiguity or possible cloud contamination, additional clear-sky restoration tests are applied to recover likely cloud-free pixels. An example of the final product, reported as one of four confidence classes, ranging from "confident clear" to "confident cloudy", is presented in Fig. 18b alongside an RGB true-color image (Fig. 18a) from MODIS/Aqua acquired on 3 December 2025 at 18:45 UTC.

Thresholds for the spectral and spatial-variability tests are derived from multiple sources, including heritage cloud-detection methods, expert interpretation of imagery, and statistics from collocated CALIOP cloud labels matched to MODIS radiances, supplemented by systematically selected and quality-controlled MODIS samples. To reduce sensitivity to any single threshold and to avoid unstable binary decisions, the algorithm explicitly represents uncertainty by assigning intermediate confidence values to observations near decision boundaries, which are then combined to produce the categorical cloud mask.

B. Cloud mask detection based on visible and near-IR observations

Visible and near-IR cloud screening exploits the generally higher shortwave reflectance of clouds relative to water and many land surfaces, while explicitly accounting for variability driven by surface properties and viewing geometry. In MODIS-type cloud masks, a single channel reflectance criterion is applied, with the selected band conditioned on surface type. Vegetated land and coastal scenes use 0.65 μm reflectance ($R_{0.65}$), arid regions use 0.413 μm ($R_{0.413}$) reflectance as discussed by [102], and water scenes use 0.86 μm reflectance ($R_{0.86}$). Figures 19a and 19b show $R_{0.65}$ and $R_{0.86}$, respectively, for an example scene. Both fields capture the spatial distribution of clouds, with $R_{0.65}$ providing a clearer contrast between surface and cloud over land, and $R_{0.86}$ providing a better contrast over the ocean. To reduce false cloud identification associated with spatially varying surface albedo and bidirectional reflectance effects, land thresholds are formulated as dynamic functions of the background Normalized Difference Vegetation Index (NDVI) and

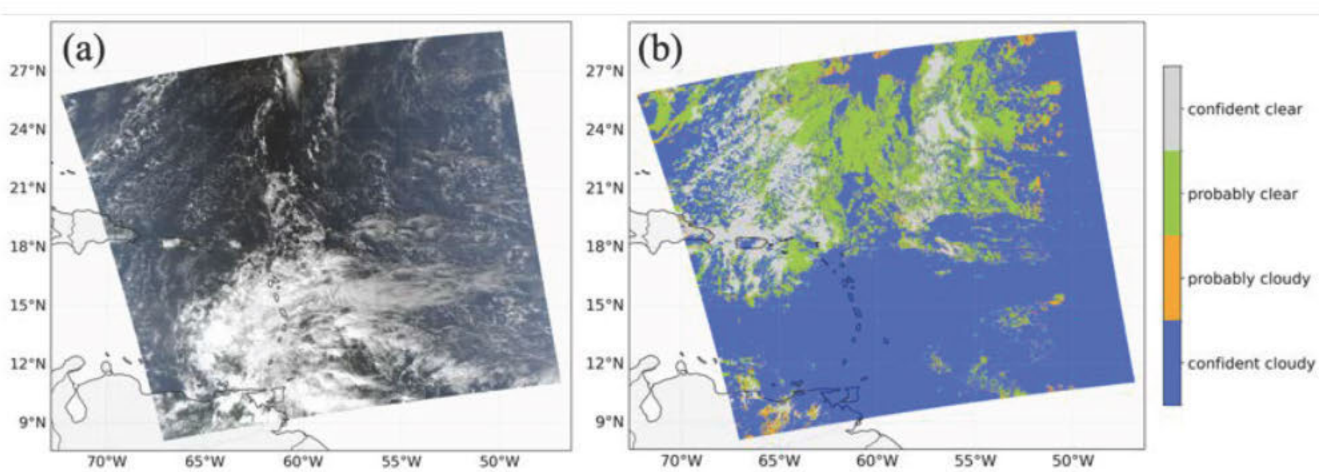

Fig. 18. Example MODIS/Aqua scene acquired on 3 December 2025 at 18:45 UTC, showing true-color imagery and the corresponding cloud-mask classification. (a) RGB true-color composite with bands 1, 4, and 3 mapped to red, green, and blue, respectively. (b) Cloud-mask output for the same swath, displayed as four confidence classes: confident clear, probably clear, probably cloudy, and confident cloudy.

scattering angle [103]. NDVI climatologies are obtained from snow-free multiyear products such as [104]. Thresholds are derived empirically by constructing cumulative distributions for clear and cloudy samples within bins of NDVI and scattering angle, identifying confident-clear and confident-cloudy cutoff values from separation in the distribution tails, and fitting the resulting thresholds as functions of scattering angle to enable pixel-level, view-dependent classification. Over the ocean, the same reflectance-based approach is further modified under the sun-glint conditions by allowing thresholds to vary systematically with glint angle, thereby reducing the likelihood that pixels with specular reflection is misclassified as cloudy.

A complementary spectral-shape test uses the reflectance ratio $R_{0.86}/R_{0.65}$. Because cloud reflectance is nearly spectrally neutral between 0.65 and 0.86 μm, the ratio is typically close to unity over clouds, whereas clouds over the open ocean generally yield substantially smaller values, consistent with AVHRR-based experience and thresholds reported by [91], [105]. In the MODIS/Aqua example (Fig. 19c), $R_{0.86}/R_{0.65}$ reproduces the spatial pattern of the cloud field, with values near one indicating cloud coverage. Over the ocean, MODIS applies a set of thresholds spanning confident clear to confident cloudy and accounts for altered ratio behavior under sunglint conditions. The algorithm also recognizes that arid and semi-arid land surfaces can exhibit a wide range of clear-sky ratios that overlap values commonly associated with clouds. For these challenging dryland regimes, a modified ratio formulation based on the Global Environment Monitoring Index (GEMI; [106]) is adopted, using NDVI dependent thresholds and an explicit upper limit beyond which the ratio-based criterion is not applied.

Thin cirrus is assessed using the strong water vapor absorption band near 1.38 μm. When column water vapor is sufficient, surface contributions are strongly attenuated, causing upper tropospheric ice clouds to appear bright against a suppressed background [107]. Figure 19d illustrates MODIS/Aqua reflectance at 1.38 μm, which effectively highlights high ice clouds through enhanced reflectance, while other cloud types and clear sky scenes remain comparatively dark. Practical limitations noted by [108] motivate disabling this criterion in very dry atmospheres, over high terrain, and

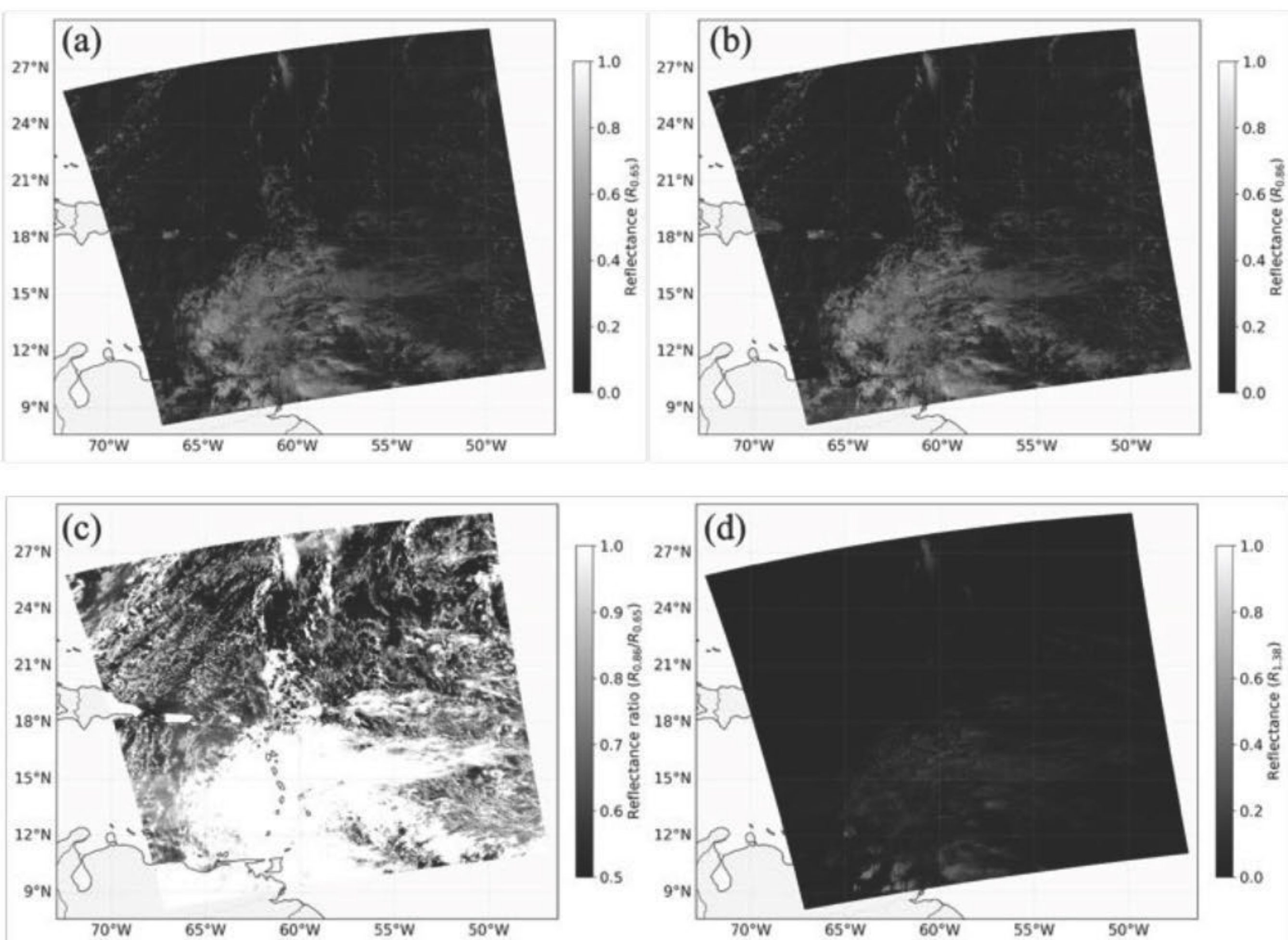

Fig. 19. Visible and near-IR reflectance fields for the MODIS/Aqua scene acquired on 3 December 2025 at 18:45 UTC. (a) Reflectance at 0.65 μm ($R_{0.65}$). (b) Reflectance at 0.86 μm ($R_{0.86}$). (c) Reflectance ratio ($R_{0.86}/R_{0.65}$). (d) Reflectance at 1.38 μm ($R_{1.38}$).

over Antarctica and Greenland. The algorithm further differentiates general cirrus detection from a thin cirrus indicator by applying separate threshold ranges.

C. Cloud Mask Detection based on IR Brightness Temperature Thresholds and Their Differences

The IR cloud masking method is based on BT and BTD. Note that BT corresponding to measured spectral radiance I_λ is given by $B_\lambda^{-1}(I_\lambda)$, where B_λ^{-1} indicates the inverse Planck's function. The BTD for two channels is given by the difference between BT (λ_1) and BT (λ_2). In particular, this method treats clouds as perturbations to clear-sky thermal radiance and exploits how absorption and emission within and above cloud layers modify BTs in adjacent spectral windows. This physical basis supports a compact set of window channel thresholds and BTD

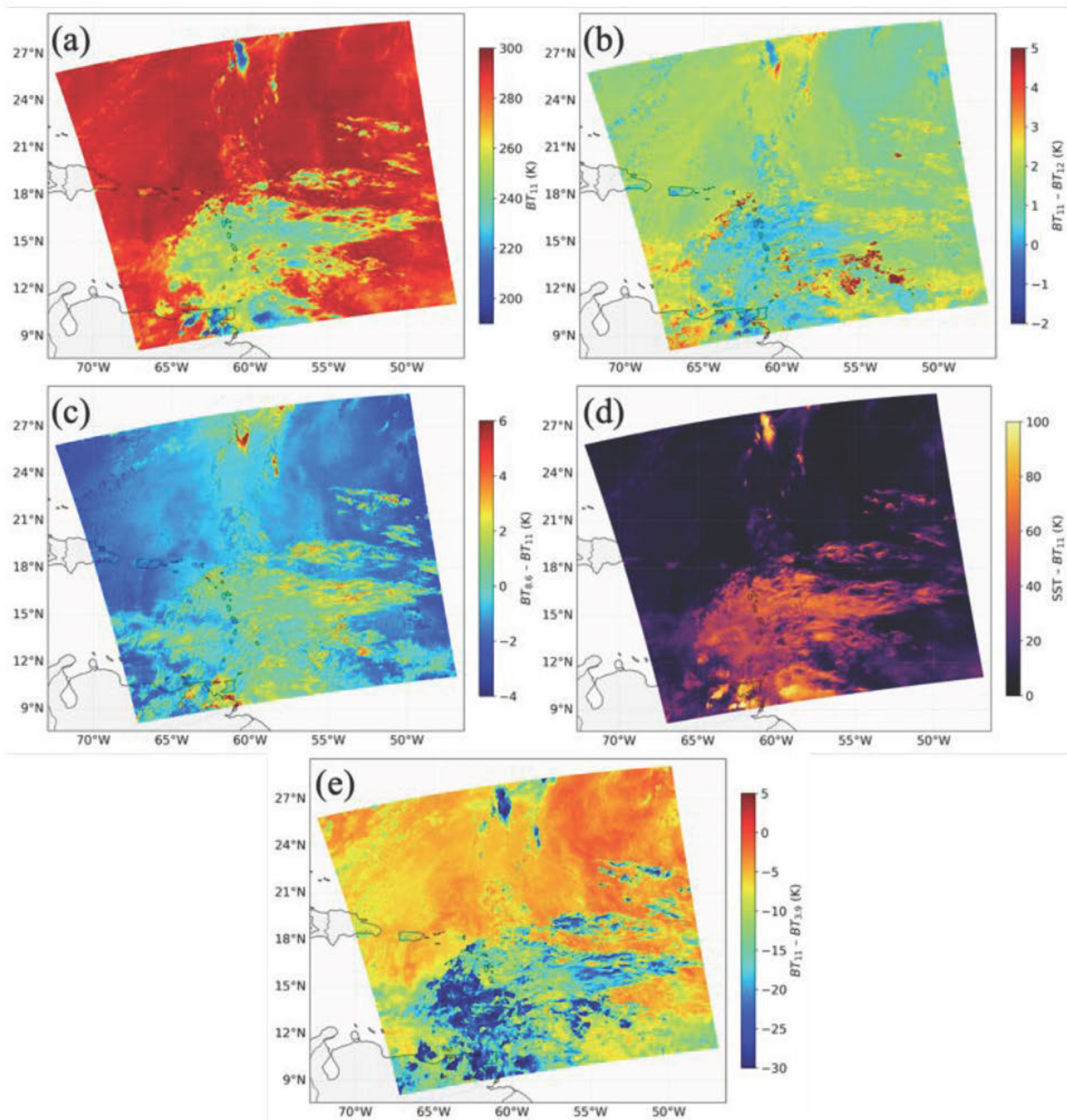

Fig. 20. IR brightness temperature fields and window channel contrasts for the MODIS/Aqua scene acquired on 3 December 2025 at 18:45 UTC. (a) BT at 11 µm (BT_{11}). (b) BTD between 11 µm and 12 µm ($BT_{11} - BT_{12}$). (c) BTD between 8.6 µm and 11 µm ($BT_{8.6}$ - BT_{11}). (d) Sea surface temperature consistency residual (SST – BT_{11}). (e) BTD between 11 µm and 3.9µm ($BT_{11} - BT_{3.9}$).

diagnostics that are sensitive to cloud optical depth, particle size, and atmospheric moisture. In MODIS schemes, an initial cold-cloud screen applies an $\lambda = 11$ µm brightness temperature threshold over the ocean (Fig. 20a). Over land, the same channel is used more conservatively and may also contribute to clear-sky restoration when surface-type constraints indicate that a warm BT_{11} is inconsistent with a cloud. The split-window BT_{11}-BT_{12} (Fig. 20b) is subsequently used to identify semi-transparent cirrus clouds, since differential absorption in the window bands enhances the contrast for thin ice clouds, consistent with AVHRR and geostationary applications [91], [109] and later refinements under the polar conditions [96]. Additional window contrasts such as $BT_{8.6} - BT_{11}$ (Fig. 20c) are effective over liquid water surfaces as land surface emittance at 8.6 µm is too variable, with confidence thresholds set to 0.0 K, −0.5 K, and −1.0 K. To limit false cloud identification driven by water vapor absorption, surface temperature consistency constraints compare BT_{11} with an estimated bulk sea surface temperature (SST) over the ocean derived from window channel structure, viewing geometry, and the Global Data Assimilation System (GDAS) initial guess [110]. The cloud condition is indicated when the SST – BT_{11} residual (Fig. 20d) exceeds 3.0 K, 2.5 K, and 2.0 K. Nighttime land analogs use GDAS surface temperature differences with empirically tuned thresholds that incorporate BT_{11}-BT_{12} and view angle. The shortwave-to-longwave window contrast BT_{11}-$BT_{3.9}$ (Fig. 20e) targets low cloud and fractional cloud cover because 3.9 µm radiance is more sensitive to the warmer component of a mixed scene. This yields large negative differences for broken clouds at night and strongly negative differences during daytime due to reflected solar radiation. Over deserts, a two-sided acceptance range is required to accommodate highly variable surface emissivity, and a separate stratus indicator is tracked over nighttime ocean.

In addition, several brightness temperature difference thresholds provide complementary information for nighttime cloud detection. Screening for high and optically thin clouds is supported by $BT_{3.9}$ - BT_{12}, which is comparatively insensitive to water vapor and effective for distinguishing thin cirrus from clear conditions [111]. Distinct threshold regimes are applied for non-polar land, snow-covered surfaces, and polar night, where extremely cold and dry atmospheres constrain the usable dynamic range. A further nighttime diagnostic over land uses $BT_{7.3}$ - BT_{11}, leveraging the mid tropospheric sensitivity of the 7.3 µm water vapor absorption band relative to the surface-dominated 11 µm window. Thresholds are tuned for both midlatitude conditions and polar night inversion environments, where the thresholds vary with BT_{11} and cloud tends to reduce the magnitude of the clear sky contrast, consistent with the inversion focused analysis of [112].

IV. CLOUD THERMODYNAMIC PHASE

The physical basis of cloud mask determination is reviewed in the previous section. To infer the cloud properties of a cloudy scene in satellite observations, the next step is to determine whether the cloud is water, ice, or mixed-phase. Notably, cloud phase inference has standalone value, as cloud thermodynamic phase strongly modulates cloud radiative effects and, by extension, climate feedbacks, because ice and liquid clouds differ in their optical properties, microphysical evolution, and the vertical distribution of absorbed and emitted energy. Early large-scale estimates of cloud variability and outgoing longwave radiation relied primarily on thermal IR window radiances from polar orbiting and geostationary satellites [113], [114]. However, single channel approaches often underestimate semitransparent cloud, which motivated the adoption of multispectral strategies that better capture cirrus clouds in climatological applications [115], [116]. Multispectral imagers consequently enable joint statistics of semitransparent cloud occurrence and phase at kilometer scale resolution, and long-term analyses indicate that cirrus and other transmissive high clouds comprise a substantial fraction of global high cloud observations.

Within satellite cloud retrieval systems, cloud thermodynamic phase is both a geophysical product and a key constraint that determines the appropriate microphysical and radiative transfer assumptions for subsequent optical and microphysical property retrievals. Operational algorithms explicitly propagate the cloud thermodynamic phase field into downstream steps, so cloud therdynamic phase misclassification can translate directly into biases in derived quantities. This dependence is well established for passive imager retrievals of optical thickness and effective particle size, which typically require phase information to ensure physically consistent solutions. Sensitivity to phase is further amplified by the widespread use of single-layer radiative transfer representations, since multilayer scenes and vertical phase overlap can introduce systematic artifacts. Examples include effective radius biases when an optically thin cirrus cloud overlies a liquid cloud and anomalous droplet size estimates when an ice cloud is mischaracterized as a liquid one. These considerations motivate explicit identification and flagging of multilayer conditions and phase-inconsistent scenes to protect climatological statistics and derived microphysics.

Methodologically, contemporary phase detection builds on split window and multispectral thermal IR approaches developed to characterize semitransparent cirrus clouds and to support long climate records from sensors with more limited channels such as AVHRR. In this context, split-window frameworks have been developed to improve cloud temperature and emissivity climatologies and to produce multidecadal datasets suitable for variability studies. A major step in strengthening operational cloud thermodynamic phase products has been systematically evaluated and constrained using independent active sensor references, particularly observations by CALIOP on CALIPSO, together with continued refinement of sensor characterization and intercomparisons. In MODIS Collection 6 refinements, comparisons with CALIOP phase products indicate improved identification of ice clouds, with fewer optically thin ice clouds misclassified as liquid clouds. Complementary quality controls also enforce physical consistency across retrieval components, allowing cloud thermodynamic phase classifications that conflict with robust high-cloud indicators from cloud-top retrievals to be corrected and transparently flagged for researchers. Below, we summarize the physical basis of IR cloud phase determination.

IR-based cloud thermodynamic phase retrievals are designed to operate independently of solar illumination by exploiting phase-dependent spectral structure in thermal emission. The MODIS approach originated as a trispectral method using the 8.6, 11, and 12-µm bands and was later simplified to a bispectral technique using the 8.6 and 11-µm bands, with cloud thermodynamic phase inferred from the combined behavior of the 11-µm brightness temperature and the brightness temperature difference. Conceptually, the 11-µm band provides a robust constraint on cloud-top thermal state and optical thickness in the window region, while $BT_{8.6}$ -BT_{11} captures phase-sensitive reshaping of the spectrum across nearby window bands. The observed radiances, and therefore the BTD signatures, depend on gaseous absorption (especially water vapor), cloud scattering and absorption governed by particle size distributions, and for ice clouds by ice crystal habit/shape, partial transmission of surface emissivity through optically thin clouds, and cloud height.

Figure 21a presents an example cloud thermodynamic phase product from MODIS Aqua acquired on 3 December 2025 at 18:45 UTC. The physical basis for phase sensitivity in the 8–13 µm region is the complex refractive index of liquid water and ice. The measured refractive indices show that m_i for ice and water are similar between roughly 8.5 and 10 µm but diverge between 10 and 13 µm as illustrated in Fig. 21b. As a result, two clouds with comparable cloud-top temperature, altitude, and particle size distributions can yield similar radiances near 8.5 µm while producing different radiances at the longer window wavelengths because absorption and effective emissivity differ by phase. This wavelength-dependent absorption contrast is the physical foundation for using thermal window BTDs, such as $BT_{8.6}$ -BT_{11}, to infer cloud thermodynamic phase. Cloud thermodynamic phase discrimination based on IR differences remains conditional. Optically thin clouds, substantial surface contributions, and strong variability in atmospheric absorption can yield similar brightness temperature differences for multiple combinations of phase, particle size, and cloud transmissivity, which limits separability using IR information alone.

Operational experience with the MODIS Collection 5 IR phase product highlighted two systematic limitations that follow directly from these physics. First, optically thin cirrus can be misclassified because the surface and lower-tropospheric radiance contributions reduce the phase-specific spectral contrast. Second, discrimination of supercooled water and mixed-phase conditions is intrinsically difficult with IR-only radiances because mixtures, vertical phase layering, and small liquid droplets can yield ambiguous BTD signatures that overlap those of ice and water endmembers. These limitations motivated a simplification of reported categories in MODIS Collection 6 to ice, water, and uncertain, explicitly merging the earlier mixed-phase and undetermined outcomes because the IR-only signal provides limited skill in separating them reliably.

MODIS Collection 6 also strengthened the physical treatment of thin cirrus clouds in the 1 km product by shifting from raw BTD thresholds toward cloud emissivity ratios. The key idea is to reduce surface influence by explicitly referencing clear-sky radiance, either from radiative transfer modeling or nearby cloud-cleared pixels, and then forming band-to-band emissivity relationships summarized by the β parameter of [117]. This approach is described in the context of cirrus-focused improvements by [118], [119], [120], and it primarily improves identification of optically thin high clouds as ice clouds rather than enhancing water-cloud discrimination. A practical complication is that the cloud thermodynamic phase algorithm is executed independently of the cloud-top height retrieval, and cloud height is therefore unavailable when emissivity is estimated. The adopted solution uses a tropopause-temperature reference to keep inferred emissivities

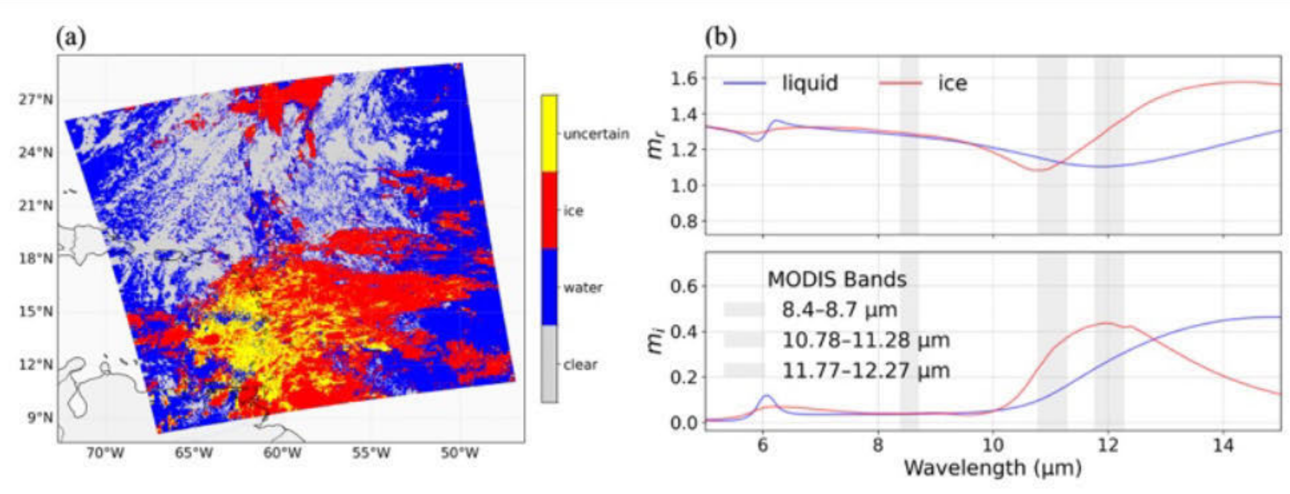

Fig. 21. Cloud phase characterization for the MODIS/Aqua scene acquired on 3 December 2025 at 18:45 UTC. (a) Cloud phase classification from the IR phase product, shown as four categories: clear, water, ice, and uncertain. (b) Representative spectral dependence of the real part (m_r) and imaginary part (m_i) of the refractive index for liquid water and ice across the thermal IR; shaded bands indicate the MODIS thermal IR channels used for cloud phase identification.

physically bounded and leverages the finding that emissivity variations with cloud height are relatively small for cirrus in the upper troposphere when using window bands. Absorption-band information is additionally incorporated to provide height context and to distinguish low-level clouds from optically thin, high-altitude ice clouds. The 7.3 µm band is selected for its mid-tropospheric sensitivity and its reduced susceptibility to artifacts observed in some 15 µm channels, which helps preserve the relative spectral signatures required for phase discrimination even when the tropopause reference introduces bias in absolute emissivity estimates for low clouds.

V. CO_2 SLICING METHOD FOR CLOUD-TOP HEIGHT

Cloud-top height is an important cloud property, which is essential for implementing cloud property retrieval techniques based on IR bands. Smith et al. [85] pioneered the CO_2 slicing method to infer cloud-top pressure using two spectral bands in the CO_2 15-µm absorption spectrum. Here we recapture the main physical principles of this method. In the CO_2 15-µm absorption spectrum, the multiple-scattering effect of clouds is relatively unimportant and can be neglected, allowing the assumption of non-reflecting cloud layers. In reference to Fig. 22, the TOA nadir-viewed radiance at wavenumber ν under the cloudy condition can be approximated by

$$I_\nu^{cld} = \varepsilon_\nu B_\nu(T_c)\Gamma_\nu(P_c,0) + (1-\varepsilon_\nu)[B_\nu(T_s)\Gamma_\nu(P_s,P_c) + \int_{P_s}^{P_c} B_\nu[T(p)]\frac{\partial\Gamma_\nu(P,P_c)}{\partial lnP}dlnP]\Gamma_\nu(P_c,0) + \int_{P_c}^{0} B_\nu[T(p)]\frac{\partial\Gamma_\nu(P,0)}{\partial lnP}dlnP, \quad (56)$$

where B indicates Planck's function, and ε_ν is the cloud emissivity. In Eq. (56), the surface emissivity is implicitly assumed to be unity. (1-ε_ν) represents the transmissivity of the cloud layer. $\Gamma_\nu(P_1,P_2)$ is the atmospheric transmissivity from pressure level P_1 at altitude z_1 to pressure level P_2 at altitude z_2 ($z_2 > z_1$ and $P_1 > P_2$) given by

$$\Gamma_\nu(P_1,P_2) = \exp\left(-\int_{z_1}^{z_2} k_{CO_2,m}\rho_{O_2}dz\right) = \exp\left(-\int_{P_2}^{P_1} k_{CO_2,m}q dP/g\right), \quad (57)$$

where $k_{CO_2,m}$ is the CO_2 mass absorption coefficient, ρ_{O_2} is the CO_2 mass density, q is the mixing ratio of CO_2, and g is the acceleration of gravity. On the right-hand side of (56), the first term represents the transmission of cloud emission to TOA, the second term represents the transmission of the surface emission and the emission of the atmospheric portion below the cloud through the cloud layer and then further to TOA, and the third term represents the contribution by the emission of the atmospheric portion above the cloud layer. In this sense, the CO_2 slicing method divides a cloudy atmosphere into three portions: the atmosphere below the cloud, the cloud layer, and the atmosphere above the cloud.

Noticing that $\Gamma_\nu(P,0) = \Gamma_\nu(P,P_c)\cdot\Gamma_\nu(P_c,0)$ and the clear-sky radiance is given by $I_\nu^{clr} = B_\nu(T_s)\Gamma_\nu(P_s,0) + \int_{P_s}^{0} B_\nu[T(p)]\frac{\partial\Gamma_\nu(P,0)}{\partial P}dP$, we can simplify the cloudy-sky radiance in Eq. (56) as follows

$$I_\nu^{cld} = \varepsilon_\nu B_\nu(T_c)\Gamma_\nu(P_c,0) + (1-\varepsilon_\nu)I_\nu^{clr} + \varepsilon_\nu\int_{P_c}^{0} B_\nu[T(p)]\frac{\partial\Gamma_\nu(P,0)}{\partial lnP}dlnP. \quad (58)$$

It should be pointed out that I_ν^{cld} is incorrectly expressed in some studies reported in the literature as

$$I_\nu^{cld} = \varepsilon_\nu B_\nu(T_c) + (1-\varepsilon_\nu)I_\nu^{clr}. \quad (59)$$

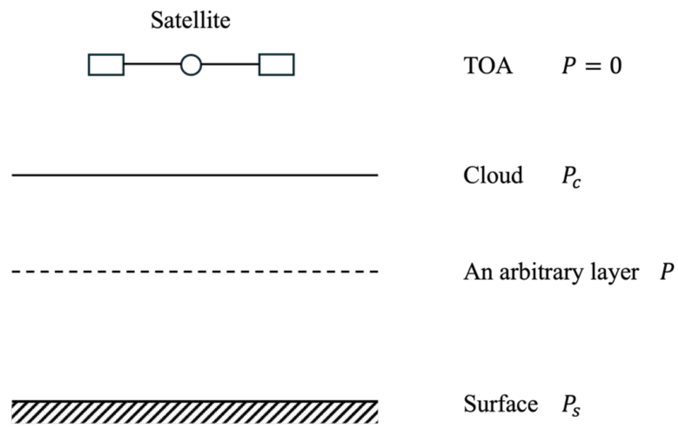

Fig. 22. The atmospheric configuration for the CO_2 slicing method.

The above expression may be a good approximation for high clouds but may introduce substantial retrieval biases for low clouds. For a partially cloudy pixel with cloud amount N, the corresponding radiance is given by

$$I_\nu = NI_\nu^{cld} + (1-N)I_\nu^{clr} = (1-N\varepsilon_\nu)I_\nu^{clr} + N\varepsilon_\nu B_\nu(T_c)\Gamma_\nu(P_c,0) + N\varepsilon_\nu\int_{P_c}^{0} B_\nu(P)\frac{\partial\Gamma_\nu(P,0)}{\partial lnP}dlnP, \quad (60)$$

where $N\varepsilon_\nu$ is referred to as the effective cloud amount. Furthermore, it is straightforward to prove the following relation:

$$I_\nu - I_\nu^{clr} = -N\varepsilon_\nu I_\nu^{clr} + N\varepsilon_\nu B_\nu(T_c)\Gamma_\nu(P_c,0) + N\varepsilon_\nu\int_{P_c}^{0} B_\nu(P)\frac{\partial\Gamma_\nu(P,0)}{\partial lnP}dlnP = N\varepsilon_\nu B_\nu(T_c)\Gamma_\nu(P_c,0) + N\varepsilon_\nu[-B_\nu(T_s)\Gamma_\nu(P_s,0) - \int_{P_s}^{P_c} B_\nu(P)\frac{\partial\Gamma_\nu(P,0)}{\partial P}dP]. \quad (61)$$

Moreover, we have

$$\int_{P_s}^{P_c} B_\nu(P)\frac{\partial\Gamma_\nu(P,0)}{\partial P}dP = B_\nu(P_c)\Gamma_\nu(P_c,0) - B_\nu(P_s)\Gamma_\nu(P_s,0) - \int_{P_s}^{P_c}\Gamma_\nu(P,0)\frac{\partial B_\nu[T(P)]}{\partial lnP}dlnP. \quad (62)$$

From (61) and (62), we obtain

$$I_\nu - I_\nu^{clr} = N\varepsilon_\nu\int_{P_s}^{P_c}\Gamma_\nu(P,0)\frac{\partial B_\nu[T(P)]}{\partial lnP}dlnP. \quad (63)$$

Unlike the absorption of atmospheric gases, cloud optical properties vary relatively slowly with wavenumber. Therefore, it is a reasonable approximation to assume the cloud emissivity values at two bands within the CO_2 15-µm spectrum at wavenumber ν_1 and ν_2 to be the same, that is, $\varepsilon_{\nu_1} = \varepsilon_{\nu_2}$. From (63), we have

$$\frac{I_{\nu_1} - I_{\nu_1}^{clr}}{I_{\nu_2} - I_{\nu_2}^{clr}} = \frac{\int_{P_s}^{P_c} \Gamma_{\nu_1}(P,0) \frac{\partial B_{\nu_1}[T(P)]}{\partial lnP} dlnP}{\int_{P_s}^{P_c} \Gamma_{\nu_2}(P,0) \frac{\partial B_{\nu_2}[T(P)]}{\partial lnP} dlnP}. \quad (64)$$

The above equation provides the basis for inferring P_c. Table 1 lists three examples of the CO_2 slicing-based retrievals compared with radiosonde- and lidar-derived values [23].

TABLE I
THREE EXAMPLES OF THE CO_2 SLICING METHOD RETRIEVALS OF CLOUD-TOP PRESSURE. THE CORRESPONDING RADIOSONDE AND LIDAR INDICATED CLOUD-TOP PRESSURE ALTITUDES ARE ALSO LISTED. DATA TAKEN FROM [23].

Radiosonde Pressure (hPa)	Lidar Pressure (hPa)	CO_2 slicing pressure (hPa)
830	830	800
850	830	850
550	550	550

VI. CLOUD OPTICAL THICKNESS AND EFFECTIVE PARTICLE SIZE

In Section II, we elaborated on the importance of cloud optical thickness and effective particle size, particularly manifested by Eqs. (19)-(22). In this section, we review two widely used algorithms for inferring these two cloud properties using solar bands and thermal IR bands, respectively.

A. Physical basis of retrieval algorithms

The fundamental principle for retrieving cloud optical thickness and effective particle size is to match observed cloud reflectances to forward radiative transfer simulations, iteratively adjusting parameters until convergence between the observed and simulated radiances is achieved [16], [17]. To ensure computational efficiency, this approach typically uses precomputed LUTs for ice and liquid water clouds, which account for various solar/viewing geometries, cloud heights critical to IR cloud property remote sensing techniques, and atmospheric profiles. The optimal estimation method [121] is commonly used to enhance computational efficiency when comparing observations and simulations (e.g., [122], [123]). In particular, the following optimal estimation algorithm is applied in the inversion part of the retrieval algorithms, which can obtain an optimal solution by minimizing the cost function:

$$J(x) = (x - x_a)^T S_a^{-1} (x - x_a) + [y - F(x,b)]^T S_y^{-1} [y - F(x,b)], \quad (65)$$

where x, y, and b are the state vector, the measurement vector, and the model parameter vector, respectively. x_a represents the *a priori* value of the corresponding state vector. $F(x,b)$ is the simulated measurement calculated from the optical property model using the forward models. S_a and S_y are the error covariance matrices for *a priori* values and measurements. The underlying radiative transfer computations require a defined set of cloud single-scattering properties, namely the phase function, single-scattering albedo, and extinction efficiency. Although radiometric observations, such as those from MODIS, do not measure the polarization state of the radiation field, using a scalar radiative transfer model that neglects the vector properties of the radiation field to compute the lookup tables may incur noticeable errors in remote sensing applications based on radiometric observations [124].
To determine optical thickness and effective particle size, operational remote sensing relies on either IR-based thermal emission or visible-shortwave IR (VIS–SWIR) solar reflection. A landmark example is the [24] bi-spectral technique, which was originally developed to use reflected sunlight to retrieve these properties for liquid water clouds. This technique has been extended to infer ice-cloud microphysical and radiative properties. To illustrate the physical basis of the bi-spectral method, Fig. 23 shows the simulations of the spherical albedo for various effective particle sizes with the same optical thickness ($\tau = 17$ at wavelength $\lambda = 0.75\ \mu m$), where the spherical albedo is defined as [68]:

$$r = \frac{2}{\pi} \int_0^{2\pi} \int_0^1 \int_0^1 R(\mu, \mu_0, \varphi - \varphi_0)\, \mu\mu_0 d\mu d\mu_0 d(\varphi - \varphi_0), \quad (66)$$

where $R(\mu, \mu_0, \varphi - \varphi_0)$ is the bi-directional reflection function defined in Eq. (53) for a general optical thickness. Figure 23 shows that, for a spectral channel centered at a wavelength shorter than 1 μm, the cloud spherical albedo is essentially independent of the effective particle size. However, channels centered in the near-IR regime, e.g., at 1.64 μm and 2.13 μm, are sensitive to the effective particle size. This spectral feature provides the physical basis for simultaneously retrieving the optical thickness and effective particle size by using a pair of visible and near-IR channels.

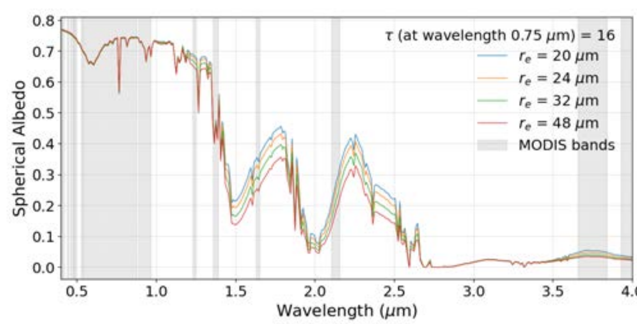

Fig. 23. Cloud spherical albedo as a function of wavelength for selected values of the effective radius of ice crystals. The single-scattering properties based on the MODIS Collection 6 ice cloud optical model illustrated in the upper panel of Fig. 13 are used for the radiative transfer simulation.

Using known single-scattering properties, radiative transfer calculations can be performed across various cloud optical thicknesses and effective particle sizes for different solar and viewing geometries. Well-established methods, such as the discrete ordinate or adding-doubling method, can then be applied to compute the bidirectional reflection functions of these clouds. Figure 24 illustrates the relationship between the reflectances in the 0.64-μm and 2.24-μm channels, two spectral channels provided by the advanced baseline imager (ABI) [125] aboard Geostationary Operational Environmental Satellites such as GOES-17, for cirrus clouds across various optical thicknesses and effective particle sizes for a specific geometry. Similar to the case of Fig. 23, the single-scattering properties based on the MODIS Collection-6 ice crystal habit model are used for the computations associated with Figs. 24 and 25, and the optical thickness values shown are referenced to a wavelength of 0.55 µm. As clouds become opaquer, the curves for optical thickness and particle size become "quasi-orthogonal." This near-orthogonal behavior allows the two-channel (bispectral) technique to independently retrieve both cloud optical thickness (primarily 0.64 µm sensitivity) and effective particle size (sensitive to both, particularly 2.24 µm). For example, if the 'X' symbol in the left panel of Fig. 24 indicates a pair of observed reflectances, one can derive an optical thickness of ~20 and an effective size of ~12.5 µm. In practice, these retrievals utilize various VIS/NIR/SWIR/MWIR combinations; for instance, MODIS uses 0.86 µm over oceans, 0.64 µm over land, and 1.24 µm over surface snow/ice for optical thickness, combined with 1.64, 2.24, or 3.7 µm channels for the effective particle size. It is worth noting that the effective sizes inferred using the 1.64-µm and 3.7-µm channels may be different, as a cloud may be vertically inhomogeneous in its microphysical properties and the two channels are sensitive to different portions of the cloud.

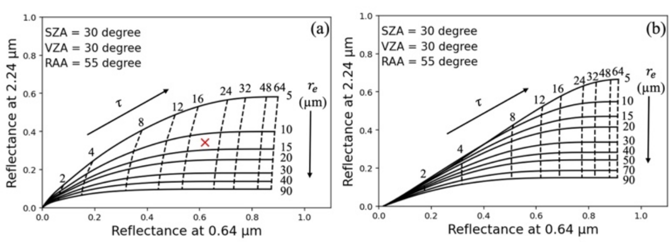

Fig. 24. The theoretical relationship between the reflection function at 0.64 and 2.24 µm for various values of cloud optical thickness (τ) and effective particle radius (r_e) for (a) liquid and (b) ice clouds. The values of the solar zenith angle (SZA), viewing zenith angle (VZA), and the relative azimuthal angle (RAA) are specified.

As an alternative or complement to VIS–SWIR bi-spectral techniques, a technique commonly referred to as the split-window technique uses IR channels within the window region (8–12 µm) to retrieve cloud properties [126], taking advantage of the spectral peak in terrestrial thermal emission. This IR technique offers the benefit of consistent, simplified, day-and-night data reduction, while avoiding the sun glint often present in shortwave reflectance data. They also provide clearer data interpretation over reflective surfaces. These retrievals rely on the sensitivity of BT and cloud emissivity, representing graybody/blackbody emission, to cloud particle size and optical thickness, as illustrated by Fig. 25. By comparing the measured BTD to theoretical models, simultaneous retrievals of cloud microphysics can be obtained, similar to VIS-SWIR techniques. However, the IR technique is more sensitive to atmospheric profiles (specifically temperature and absorbing gases), cloud height, and the surface emissivity, and is limited to optically thinner clouds, as emission becomes indistinguishable from a blackbody for optical thicknesses greater than 10–12. The split-window technique has been employed to develop operational cloud property products [127] based on observations made by the IIR aboard the CALIPSO platform [65].

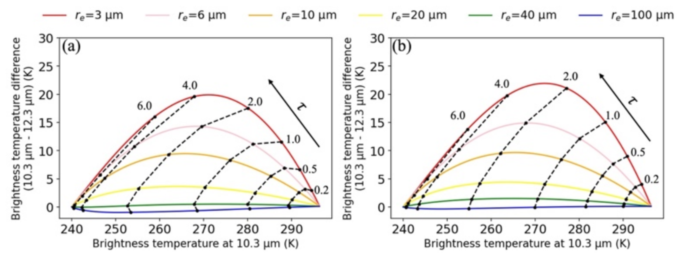

Fig. 25. The variation of the BTD between the 10.3- and 12.3-µm channels as a function of the BT in the 10.3-µm channel, computed for ranges of cloud optical thicknesses and effective particle sizes for (a) liquid and (b) ice clouds.

B. Examples of operational cloud retrieval products based on MODIS observations

Figures 26-28 show a twenty-one year (2003-2023) global climatology of cloud macrophysical and optical properties from the Terra (morning orbit) and Aqua (afternoon orbit) MODIS Collection 6.1 cloud product datasets. Mean daytime cloud fraction and cloud-top pressure, the latter derived from either the 11 µm IR window or the CO_2 slicing technique, are shown in Fig. 26. Global oceans, particularly the stratocumulus regions off the west coasts of North America, South America, southwest Africa, and Australia, along with the Southern Ocean, are notably cloudier during the morning (Terra) than the afternoon (Aqua), owing to burn off of shallow boundary layer clouds that form at night. The reverse is true over land, where daytime surface heating induces afternoon convection and cloud formation. In both morning and afternoon, clouds over land have higher altitude cloud tops, i.e., lower cloud-top pressures, again the result of enhanced convective activity from daytime surface heating; the notable exception is the intertropical convergence zone (ITCZ) and western equatorial Pacific Ocean, where convection is frequent due to low-level Hadley Cell convergence.

Figure 27 shows the global frequency distribution of cloud optical property retrieval fraction separated by thermodynamic phase. Specifically, retrieval fraction is defined as the fraction of all pixels identified as having overcast (fully cloudy field of view, FOV) liquid (top row) or ice (bottom row) clouds that also have successful cloud optical property retrievals. As such, the sum of the liquid and ice cloud retrieval fractions for a given grid box never exceeds the grid box cloud fraction and typically is smaller, given retrieval failures [reflectance observations lying outside the cloud optical thickness cloud effective radius solution space] and/or classification of "cloudy" pixels as being only partly cloud-filled. Nevertheless, these retrieval fractions illustrate the dominant patterns of global cloud phase. Liquid clouds dominate global oceans, and the marine boundary-layer stratocumulus regions are clearly observable, as is the vast cloudiness of the Southern Ocean. Conversely, ice clouds dominate the ITCZ and other deep convective zones, including the western equatorial Pacific and the Amazon and Congo basins. Moreover, the liquid cloud fractions evidently decrease during the afternoon (Aqua) compared with the morning (Terra) due to cloud burn-off, and ice cloud fractions over land surfaces and other convective regions increase due to afternoon heating-driven convection, as noted above in the cloud fractions (Fig. 27).

Figures 28 and 27 show the mean cloud optical thickness and cloud effective radius, respectively, for liquid (top rows) and ice (bottom rows) clouds. These statistics are derived from cloud optical thickness/cloud effective radius retrievals that use the VIS-SWIR bi-spectral channel pair (with the 2.13-µm channel as the SWIR channel) that is the standard MODIS retrieval. For liquid clouds, cloud optical thicknesses are larger over land and, like the liquid retrieval fractions in Fig. 27, decrease during the afternoon. For ice clouds, cloud optical thickness, particularly over land, increases during the afternoon due to enhanced convection. The marine stratocumulus regions are clearly observable in the liquid cloud effective radius statistics as the regions of smaller cloud effective radii off the southwest coasts of North America, South America, and Africa.

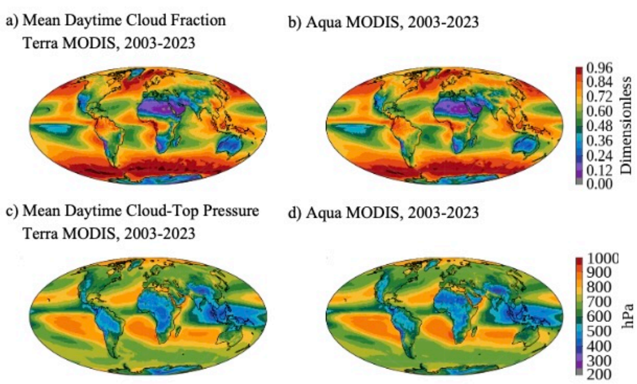

Fig. 26. Multi-year mean daytime cloud fraction (top row) and cloud-top pressure (bottom row) from Terra (left column) and Aqua (right column) MODIS derived from the 21-year (2003-2023) Collection 6.1 cloud product data record. For MODIS, cloud-top pressure is derived from a combination of the 11µm IR window channel approach for low or thick clouds and the CO_2 slicing approach for high thin clouds.

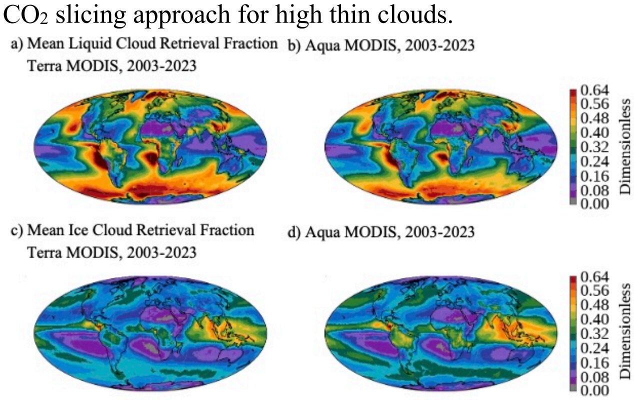

Fig. 27. Upper row: Multi-year mean retrieval fraction for liquid clouds derived from the 21-year (2003-2023) observational record of Terra (a) and Aqua (b) MODIS. Lower row: Similar to the upper row but for ice clouds from Terra (c) and Aqua (d) MODIS. Statistics are derived from the Collection 6.1 cloud products, with retrieval fraction defined as the fraction of all observations for which an overcast cloud scene is observed, and cloud optical/microphysical properties are successfully retrieved.

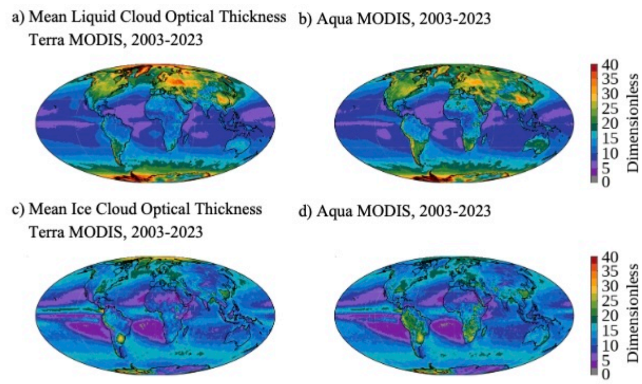

Fig. 28. Upper row: Multi-year mean liquid cloud optical thickness derived from the twenty-one year observational record (2003-2023) of Terra (left column) and Aqua (right column) MODIS. Lower row: Similar to the upper row but for ice clouds. All panels are derived from the Collection 6.1 Terra and Aqua MODIS cloud products using retrievals from the VIS-SWIR bi-spectral retrieval algorithm (with 2.13 µm as the SWIR channel).

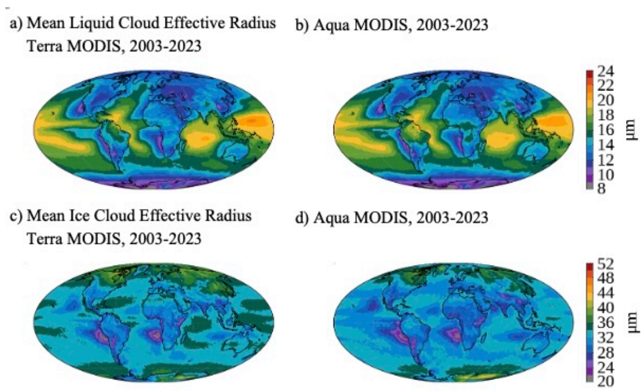

Fig. 29. Upper row: Similar to the upper row of Fig. 28, but for liquid cloud effective radius. Lower row: Similar to the lower row of Fig. 28, but for ice cloud effective radius. As in Fig. 28, these multi-year means are derived from the Collection 6.1 Terra and Aqua MODIS cloud products using retrievals from the VIS-SWIR bi-spectral retrieval algorithm (with 2.13 µm as the SWIR channel).

VII. AEROSOL PROPERTY RETRIEVALS BASED ON OBSERVATIONS MADE BY PASSIVE SENSORS

Solar radiation observed by satellite sensors is governed by scattering and absorption by gas molecules, aerosols, and clouds. Aerosols contribute to path reflectance, atmospheric transmittance, and spherical albedo, while molecular scattering and gaseous absorption further modify the observed radiance. Cloud effects, including direct contamination of aerosol remote sensing and adjacency effects such as bright cloud edges and shadows, also need to be considered. The surface reflectance contributes via the multiple scattering of the transmission and albedo functions. For example, clouds can completely obscure aerosols beneath them, and highly reflective surfaces can dominate the top-of-atmosphere signal, reducing observational sensitivity to aerosol scattering. As a result, not all observing conditions are suitable for aerosol retrievals from passive imagery, and aerosols are only retrieved in situations where when contributions from other constituents and the surface can be neglected or sufficiently characterized. Consequently, to extract aerosol properties from satellite measurements, retrieval algorithms adopt a set of simplifying assumptions to mitigate these limitations. Because aerosol signatures vary with wavelength and viewing geometry, specific spectral bands and angles are preferentially sensitive to particular aerosol types, while surface reflectance also exhibits scene-dependent spectral and angular variability across land-cover classes (e.g., vegetation, deserts, and ocean). MODIS therefore employs multiple aerosol retrieval algorithms, each optimized for different surface–atmosphere regimes. Below, we present a concise overview of the theoretical framework underlying passive aerosol remote sensing, particularly the aerosol property retrieval algorithms developed by the MODIS aerosol science team, while referring readers to complementary literature for additional context and depth.

A. Physical Basis for Aerosol Property Retrievals

A ground-based sunphotometer directly measures the total extinction of solar radiation along the atmospheric column, yielding a direct estimate of aerosol optical depth (AOD) because the detected light has not interacted with the surface. In contrast, MODIS and other passive remote sensing imagers measure solar radiance that has been scattered or reflected within the coupled Earth–atmosphere system, including contributions from the underlying surface. Consequently, aerosol retrieval from passive sensors requires isolating the atmospheric signal from surface reflectance through a set of physically based assumptions and algorithmic approximations. Certain scenes—such as those contaminated by clouds, influenced by sunglint over oceans, covered by snow or ice, or located within gaps between orbital swaths—preclude reliable retrieval. As a result, at MODIS spatial resolution, only a subset of pixels is suitable for aerosol retrieval. Over large portions of North America and adjacent ocean regions, this fraction has been estimated at approximately 34–43% of total pixels.

In the standard algorithms described below, cloudy scenes are screened a priori (e.g., using a cloud mask), and aerosol retrievals are not performed for pixels flagged as cloudy. Accurate characterization of surface reflectance is essential for isolating the atmospheric contribution to the TOA signal. Surface reflectance is prescribed or estimated using long-term climatologies, parameterizations, or temporal consistency within an inversion framework that may jointly retrieve aerosol and surface properties. The primary retrieval objective is the column-integrated aerosol loading, which requires assumptions regarding aerosol optical properties. The algorithms employ precomputed LUTs, such as those built from the scattering calculations described in Section 2, that relate TOA reflectance to aerosol amount for specified aerosol models at each wavelength across a range of viewing and solar geometries. The retrieval compares measured TOA reflectance with LUT entries for the appropriate geometry and assumed surface and aerosol properties to determine the aerosol amount that best reproduces the observation. The resulting solution provides an estimate of the spectral AOD consistent with the measured reflectance.

B. Aerosol Retrieval Algorithms Developed by the MODIS Aerosol Science Teams

There are two standard MODIS aerosol retrieval algorithms associated with the Atmosphere discipline [128]. The at-launch algorithm [129], [130] is now commonly known as Dark Target or DT [131], [132]. This was followed by the Deep Blue (DB) algorithm [21], [133], [134]. Note there is also the Multi-Angle Implementation of Aerosol Correction (MAIAC) [135] under the 'Land' discipline [136], and retrievals of aerosol properties within the 'Ocean' discipline. Each team has its own website with examples [136], [137], [138].

DT and DB are similar in that both retrieve aerosol properties along-orbit, granule by granule, but differ, however, in how they disentangle surface and atmospheric contributions to the observed signal and in how they attribute the remaining atmospheric signature specifically to aerosols rather than to other constituents. These methodological differences lead to distinct choices in scene selection, the spectral bands used for the retrieval, and the decision logic applied to determine whether a retrieval is successful and of sufficient confidence. Such differences are evident in the DT and DB (Fig. 30b-c) retrieval examples shown for the scene in Fig. 30a.

The Dark Target (DT) algorithm retrieves aerosol properties over surfaces that are radiometrically "dark," including vegetated and dark-soil regions over land and the open ocean. The DT method was conceived by [129], [130]. The physical principles of this method are that the aerosol signals observed by a spaceborne sensor are strongest over the surface with low reflectance, i.e., dark targets. Furthermore, the aerosol effect on spaceborne measurements of the atmosphere-surface reflection is proportional to λ^{-1} or even λ^{-2} [139]. As a result, the measured reflectance at a shortwave near-IR (SWNIR) channel (e.g., at 2.12 μm) is essentially contributed by the surface reflection. It is also found that the surface reflection is not independent across the solar spectrum. Therefore, it is feasible to estimate surface reflectance in blue (0.47 μm) and red (0.66 μm) channels using empirical relations. Then, aerosol properties can be inferred by matching measured and theoretical bidirectional reflection functions (39) by selecting an appropriate dynamical aerosol model describing the aerosol size distribution, index of refraction, single-scattering albedo, and phase function. In its current algorithm, DT generates an AOD product at three wavelengths over land [130] and seven wavelengths over ocean [129], with a combined AOD reported at 0.55 μm [140], [141]. The retrieval begins by aggregating native-resolution pixels into N×N blocks and applying a series of screening steps to remove clouds, snow/ice, ocean sunglint, and land surfaces exhibiting high reflectance in the visible and

SWIR bands [142]. Some of this information is provided by the upstream cloud mask (see example in Fig. 28d), while some is computed internally during the aerosol retrieval. By avoiding brighter surfaces, the algorithm reduces sensitivity to uncertainties in assumed surface reflectance. After filtering undesirable pixels, the remaining pixels within each N×N block are aggregated to form a mean multispectral reflectance vector that serves as input to the retrieval. An internal land/sea flag then routes the procedure to the appropriate land or ocean pathway.

Over land, the algorithm applies a Surface Reflectance Parameterization (SRP) that relates visible-band surface reflectance to SWIR reflectance [141], [143] and selects aerosol optical property models according to geographic region and season [20], [141]. Over ocean, surface reflectance is parameterized primarily as a function of wind speed, and the retrieval proceeds by selecting among aerosol models. It is assumed that the total aerosol is comprised of two aerosol models, one deemed as "fine" (dominated by small particles) and one deemed as "coarse" (dominated by coarse particles) [129], [140]. In addition, we assume that we know enough about that model's aerosol optical properties, molecular scattering, and surface interactions so we can calculate path reflectance and surface-atmosphere interactions. Therefore, we can approximate the total bi-directional reflection function as the sum of the contributions from the two aerosol models, balanced by the fine-mode weighting (FMW or η):

$$\tilde{R}_\lambda(\mu,\mu_0,\varphi-\varphi_0) = \eta\tilde{R}_\lambda^f(\mu,\mu_0,\varphi-\varphi_0) + (1-\eta)\tilde{R}_\lambda^c(\mu,\mu_0,\varphi-\varphi_0), \quad (67)$$

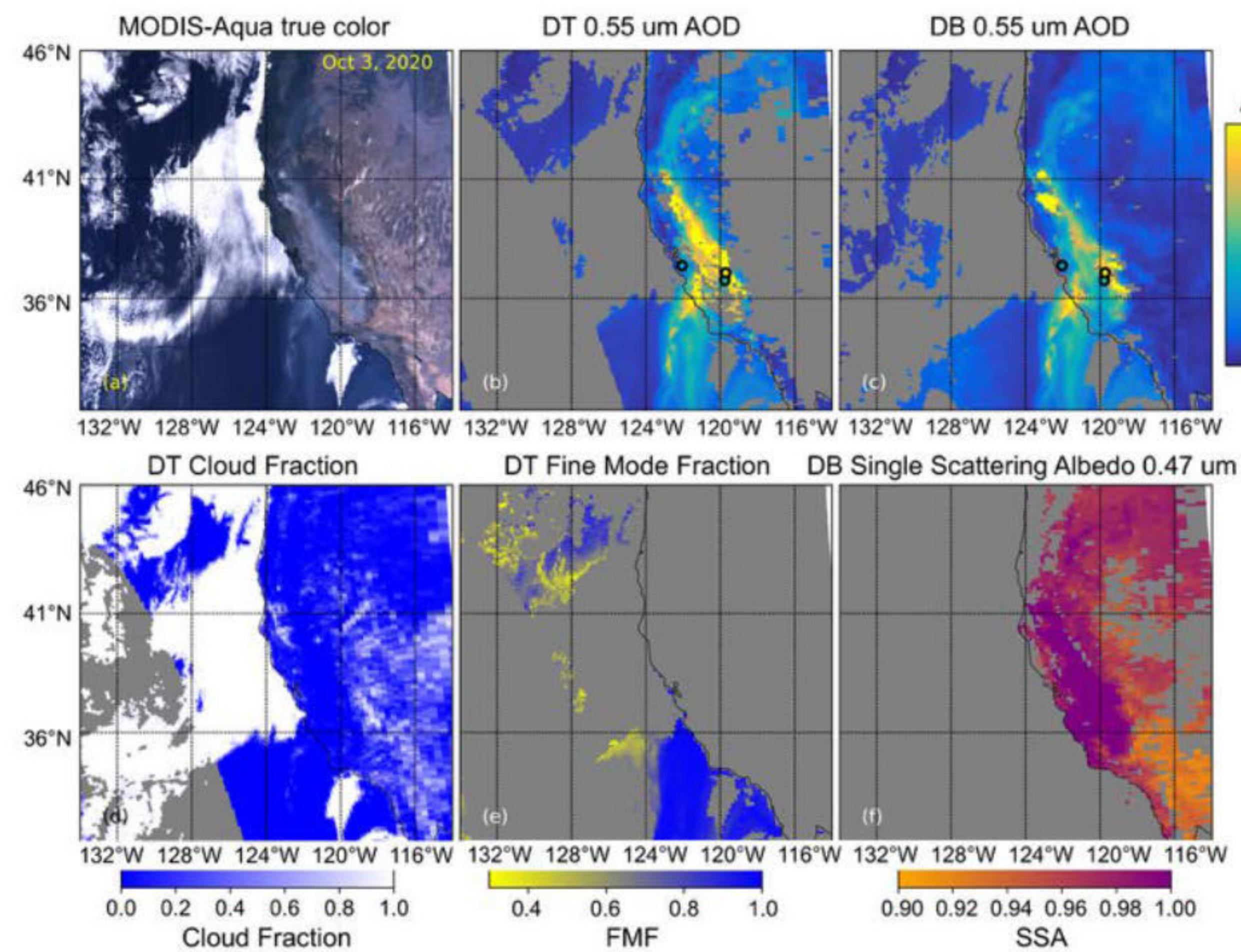

Fig. 30. Illustration of MODIS Aqua image of a smoke case near California coast on October 3, 2020. (a) MODIS RGB image. Retrievals of AOD at 0.55 mm over land and ocean from (b) DT and (c) DB algorithms, (d) cloud fraction from the DT algorithm, (e) Over-ocean AOD fine mode fraction at 0.55 mm from the DT algorithm, and (f) SSA over land at 0.47 mm from the DB algorithm. DT and DB retrievals are derived at non-gridded 10 km^2 (nadir) and are created from Aqua data. The tiny circles represent the AOD values reported at AERONET sites at the time of overpass. These AERONET sites include (with latitude/longitude): Fresno_2 (36.79°N, 119.77°W), NASA_Ames (37.42°N, 122.06°W) and NEON_SJER (37.11°N, 119.73°W). Grey areas represent "fill values" meaning that there is no value derived for that variable.

where the f and c indicate fine and coarse_aerosol models. η is independent of wavelength, and this parameter enables discrimination between coarse-mode aerosols, such as mineral dust, and aerosols dominated by smaller particles, such as smoke or urban/industrial pollution [144], [145].

Figure 30 shows an example of DT and DB aerosol property retrievals. Although the model selection and fitting procedures differ between dark targets over-land and over-ocean, both produce an estimate of the FMW, defined as the fraction of the total AOD at 0.55 μm attributable to the fine mode. An example of the fine mode fraction retrieval over dark surfaces is shown in Fig. 30e.

It is a significant challenge to infer aerosol properties over a bright surface. To address this challenge, Hsu et al. [133] developed a novel method, referred to as the Deep-blue algorithm, to retrieve aerosol properties over, e.g., arid, semiarid, and urban areas. The underlying principle is that the surface is usually bright in the red or near-IR channels for the above surface conditions, but much darker in blue spectrum ($\lambda < 0.5\ \mu m$). Based on the minimum reflectivity technique, an empirical surface reflectance database has been developed on a global scale [133], allowing simultaneous retrievals of AOD and aerosol type. However, it should be pointed out that the implementation of DB is quite involved, and the reader is referred to [133], [146], for technical details.

As sunphotometers are the most direct method for observing column-integrated aerosol properties, data from the ground-based AERONET [147], [148] have repeatedly been used to validate MODIS aerosol products [15], [21], [130], [131], [135], [149], [150], [151], [152] as demonstrated in Fig. 30. Coastal and island-based AERONET sites as well as the ship-borne Marine Aerosol Network [153] are used to evaluate over-ocean retrievals. Validation is performed site-by-site, on local, regional and/or global scales, and/or on case-by-case, or any temporal scales. Both DT and DB products have been globally validated, indicating that approximately 2/3 (or 1 standard deviation) of all satellite/sunphotometer collocations (for AOD at 0.55 mm) match within an error envelope (EE) of approximately $\pm(0.05 + 15\%)$ over land and $\pm(0.03 + 10\%)$ over ocean. Generally, the ocean surface is easier to constrain, leading to lower uncertainty. However, both DT and DB teams are clear that these numbers represent global statistics, and actual retrieval performance varies by location and season. Validation efforts have been applied for characterizing AOD at other wavelengths, as well as for aerosol Ångström exponent that is a parameter describing AOD spectral dependence, FMW, and SSA (if available as a product). In addition to validation of the retrieved products, AERONET inversion data are also used to confirm assumptions of aerosol particle properties. Each MODIS aerosol team web page can direct users to published and unpublished validation resources [136], [137], [138].

C. Examples of Operational Aerosol Retrieval Products based on MODIS Observations

Orbit-level DT and DB retrievals are routinely aggregated onto a 1° x 1° grid [154], [155] and are provided as daily and monthly aggregations including summary statistics such as the mean, standard deviation, minimum, maximum, and pixel count for each grid cell and time period. These standard products can be further aggregated to seasonal, annual, or climatological scales.

Figs. 31 and 32 present seasonal mean AOD and FMW at 0.55 μm, respectively, composited from the combined MODIS DT/DB aerosol aggregated products from Aqua over 2003–2022. The aerosol FMW is computed over both land and ocean, but is shown over ocean, where it is generally more quantitatively interpretable. High FMW indicates aerosol populations dominated by small particles typical of smoke and anthropogenic pollution, whereas low FMW is characteristic of coarse-mode plumes dominated by dust and sea salt. These seasonal composites illustrate the large-scale variability of the global aerosol system. During December–January–February (DJF), enhanced pollution is evident over East Asia and northern India, along with localized dust influences from the African Sahel. In March–April–May (MAM), dust transport intensifies from the major desert regions and biomass burning emerges over Southeast Asia. By June–July–August (JJA), wildfire smoke from boreal Asia and biomass burning over equatorial Africa coincide with active dust sources, exporting aerosol from continental regions over adjacent ocean basins. In

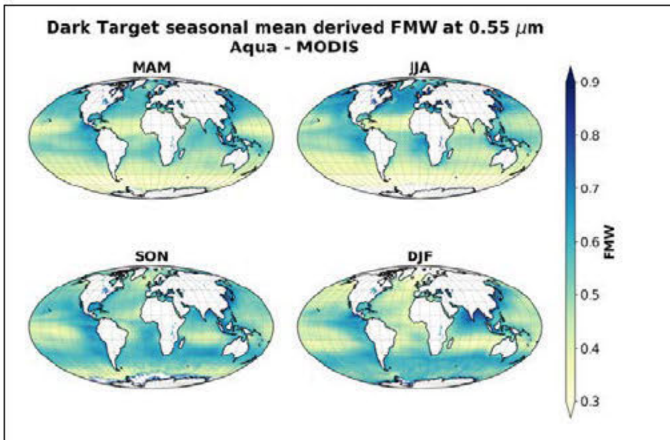

Fig. 31. 1° x 1° seasonal map of AOD at 0.55 μm, calculated from the L3 monthly gridded Aqua products: 2003-2022.

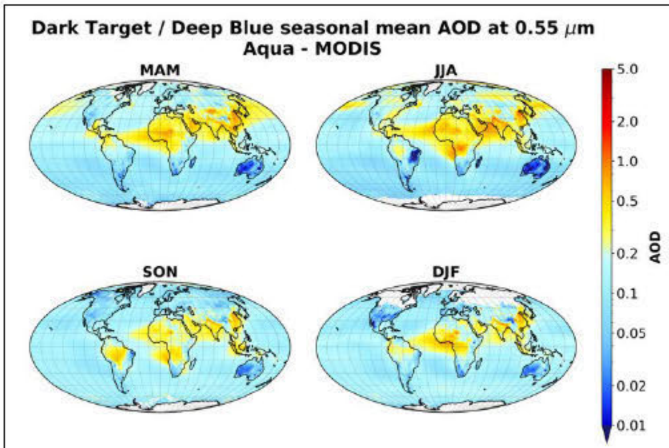

Fig. 32. 1° x 1° seasonal map of FMW at 0.55 μm, calculated from the L3 monthly gridded Aqua products:

September–October–November (SON), dust activity weakens, and biomass burning in the Amazon and southern Africa becomes the dominant source, while pollution begins to increase again over East Asia and India.

VIII. PHYSICALLY CONSISTENT RETRIEVAL OF DUST AEROSOL PROPERTIES BASED ON SYNERGISTIC OBSERVATIONS FROM ACTIVE-PASSIVE SENSORS

CALIPSO, launched on April 28, 2006, is part of the A-Train satellite constellation, dedicated to studying the optical and microphysical properties of clouds and aerosols, and their impact on the earth's radiative budget. CALIPSO carries both CALIOP, which measures the parallel and perpendicular components of the 532 nm backscattered signal, and IIR, which observes BTs in atmospheric window channels; together, these complementary measurements provide a unique and unprecedented capability for investigating dust aerosol properties.

A novel physics-based retrieval system has been developed for retrieving dust aerosol properties based on synergistical observations from CALIOP and IIR. Dust bulk optical properties are derived from the TAMUdust2020 database [28] and include regionally varying refractive indices constrained by observational mineralogical composition datasets (e.g., [156], [157], [158], [159]). These properties are used to solve the radiative transfer equation in the forward models for CALIOP and IIR, enabling a physically consistent representation of dust–radiation interactions. For the CALIOP lidar component, a Monte Carlo radiative transfer model (MCRTM; [160]) is employed to simulate 532-nm backscatter and depolarization signals based on the computed dust optical properties. Although the MCRTM-simulated backscatter and depolarization signals explicitly account for in-layer attenuation within the plume, the effect is minimal and can be considered negligible due to the thinness of each dust layer. To improve computational efficiency, LUTs are constructed from the MCRTM simulations, spanning combinations of dust aerosol optical thickness (DAOT) and dust aerosol effective radius (DAER) and their corresponding backscatter coefficient (BSC) and particulate depolarization ratio (PDPR) at 532 nm. Figure 33a illustrates the CALIOP retrieval strategy based on this LUT for both a global-mean mineralogical composition and an Eastern Asia sample, highlighting the sensitivity of DAOT and DAER to BSC and PDPR and the influence of mineralogical variability. Because CALIOP provides vertically resolved profiles of BSC and PDPR, the BSC–PDPR method can be applied to retrieve the vertical distributions of DAOT and DAER. As shown in Fig. 33a, BSC remains sensitive across a wide range of DAOT, whereas PDPR primarily constrains DAER, especially for DAER < 2 μm. This sensitivity diminishes for larger particles (DAER > 2 μm), limiting PDPR's ability to constrain coarse-mode dust. The noticeable offset and skew between the global-mean and Eastern Asia LUTs, most pronounced at large DAOT or DAER, further demonstrate the strong dependence of CALIOP-based retrievals on regional dust mineralogy.

In the thermal IR retrieval system for IIR, the forward model uses a single-layer radiative transfer scheme based on the two-stream approximation (TSARTM; [161], [162]). The TIR forward model simulates band-average BT and forms two split-window BTD, $BTD_{8.65-12.05\mu m}$ and $BTD_{10.6-12.05\mu m}$, which are used for retrieval following the established TIR sensitivity to both DAOT and DAER [163] and for the identification and retrievals of dust storms [164]. Figure 33b presents split-window diagrams for the global-mean and Eastern Asia dust samples for a dust-layer top temperature (DTT) of 285 K, assuming an off-nadir viewing angle of 3 degrees, sea surface temperature (SST) of 297 K, total precipitable water of 8 mm, and a constant surface emissivity of 0.99 in each IIR band. The two samples exhibit substantially different split-window behavior, indicating that dust mineralogical composition can exert a stronger influence on TIR-based retrievals than on CALIOP lidar-based retrievals. As DTT increases, the sensitivity to small DAER (DAER < 1 μm) decreases and the corresponding signatures increasingly overlap with those of

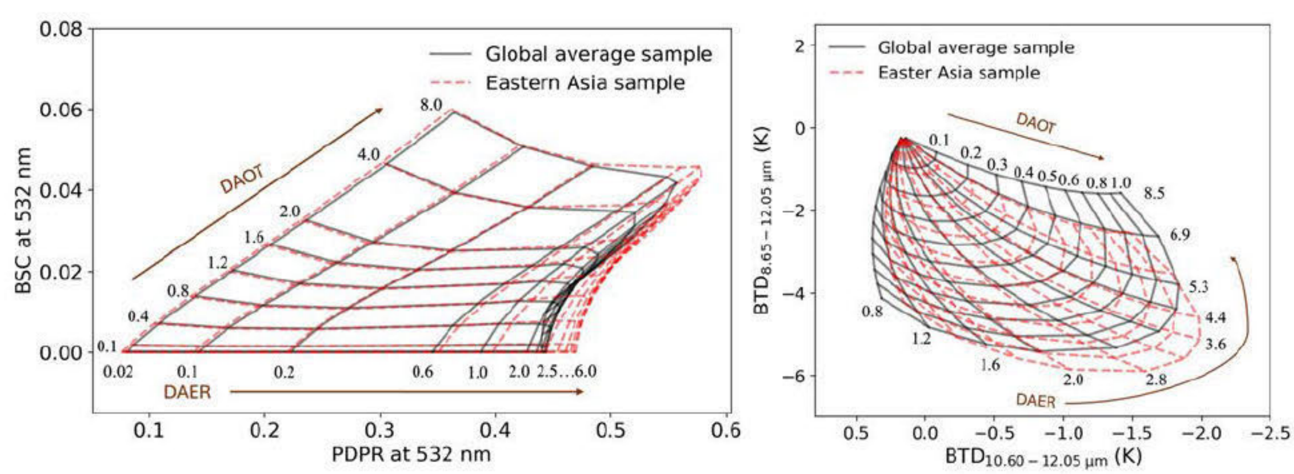

Fig. 33. Dust aerosol retrieval strategy based on (a) CALIOP measurements of the backscatter coefficient and particulate depolarization ratio and (b) IIR BT observations. Curves are shown for the global average sample (black) and Eastern Asia sample (red).

larger DAER, as reported by [165], because the thermal contrast between the surface and the dust layer becomes weak. Under these conditions, the DAOT–DAER relationship becomes strongly non-orthogonal and can be non-monotonic, which reduces retrievability and may lead to retrieval failures as well as increased uncertainties and systematic biases. For larger particles (DAER > 1 μm), the DAOT–DAER relationship becomes more orthogonal, with $BTD_{8.65-12.05\mu m}$ being relatively more sensitive to DAOT and $BTD_{10.6-12.05\mu m}$ is more sensitive to DAER. This complementary sensitivity enables simultaneous retrieval of DAOT and DAER, and the systematic shift of the split-window diagram with DTT provides an additional constraint.

The limitations of lidar-based and TIR retrieval methods have motivated the development of data-fusion approaches that combine high-spatial-resolution observations from active and passive sensors to improve dust aerosol property retrievals [165], [166], [167], [168], [169]. In [165], the active and passive retrievals are combined by using the integrated DAOT and DTT derived from the lidar-based method as a priori information in the TIR retrieval. The DTT from CALIOP is obtained by identifying the highest dust layer from the CALIOP Level 2 profile atmospheric volume description product, which specifies cloud and aerosol type for each layer, and then interpolating layer height with temperature profiles from MERRA-2 reanalysis. Because the lidar-based method has limited sensitivity to large dust aerosol effective radius (DAER), the lidar-derived DAER is not directly used as an a priori constraint in the TIR retrieval and instead serves only as a climatological reference. The lidar-based and TIR retrieval algorithms adopt consistent physical assumptions, which improves the robustness of the retrieval framework and helps ensure physical consistency between the two methods. This methodology can be extended to upcoming satellite missions such as EarthCARE, as well as to ground-based observations and broader multi-angle, multi-sensor synergistic analyses, thereby increasing its applicability to future observing systems. Figure 34 presents the retrieved global oceanic dust properties, including DAOT, DAER, DTT, and dust plume top pressure (DTP), obtained from the synergistic use of CALIOP and IIR observations, showing the spatial distribution and variability of retrieved dust optical and microphysical properties and dust-layer thermodynamic structure over ocean.

IX. MULTI-ANGLE AEROSOL REMOTE SENSING WITH MISR

Single-view, multispectral radiometric retrievals, such as those implemented for MODIS, have demonstrated substantial capability in constraining aerosol optical depth and related bulk properties by exploiting spectral contrast and empirical surface reflectance relationships. However, when observations are acquired from a single dominant viewing direction, the angular dependence of scattered radiance is only partially sampled. Multi-angle measurements provide an additional constraint by directly characterizing the directional dependence of reflectance. This capability enhances sensitivity to aerosol phase function, particle nonsphericity, and surface

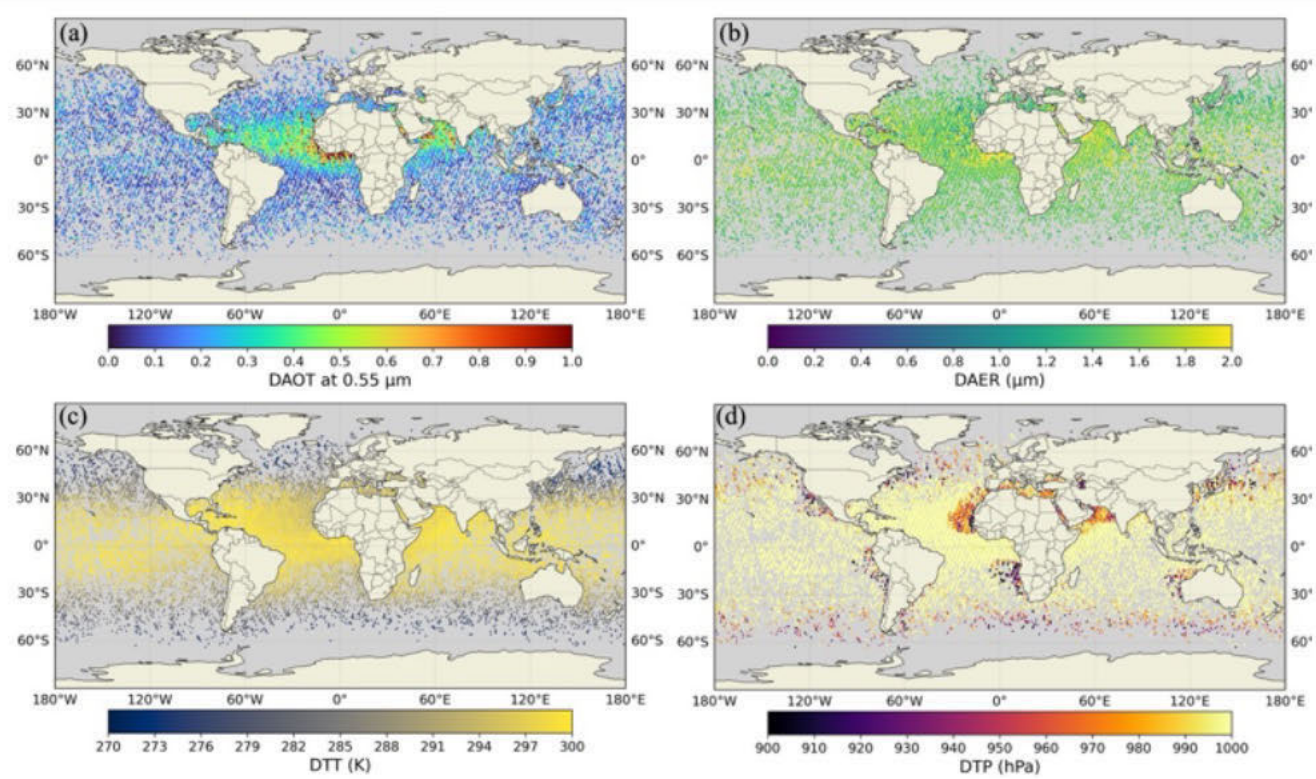

Fig. 34. Global oceanic dust aerosol retrievals for 2015 from the synergistic CALIOP–IIR retrieval system, showing (a) DAOT at 0.55 μm, (b) DAER, (c) DTT, and (d) DTP.

bidirectional reflection function. In this sense, multi-angle observations complement multispectral radiometry.

The Multi-angle Imaging SpectroRadiometer (MISR; [170]), aboard Terra, measures top-of-atmosphere reflectance at multiple viewing angles, providing significant constraints for aerosol remote sensing [171], [172]. This multi-angle view capability is achieved using nine pushbroom cameras that observe the Earth at nadir and at off-nadir angles of ±26.1°, ±45.6°, ±60.0°, and ±70.5°. Radiometric measurements are made in four spectral bands centered at 446, 558, 672, and 866 nm. Within an approximately 7-minute time interval, the cameras observe a 380 km-wide overlapped swath from the nine angles. The multi-angle measurements allow a sampling of TOA reflectance across a wide scattering-angle range within a single overpass. Capitalizing on this capability, the aerosol phase function can be better constrained, and the degeneracy between aerosol scattering and surface BRF is reduced. This provides valuable information to decouple surface reflection from aerosol scattering, discriminate dust from spherical fine-mode particles, and estimate aerosol abundance. The retrieval operationally outputs the best AOD and mixture(s) that fit the measurement. Key references for MISR instrument and aerosol retrieval algorithm have been documented in [170], [171], [173], [174], [175], [176].

A. Retrieval Algorithm

The MISR aerosol retrieval algorithm is based on a lookup-table (LUT) search approach. The observed multi-angle reflectances are compared against a precomputed database of simulated radiances across MISR's spectral bands for a total 74 candidate aerosol mixtures [22], [174]. The calculation assumes a plane-parallel atmosphere for running radiative transfer simulation. For every aerosol mixture, the LUT has the dimension of AOD and observing geometry, including solar zenith angle, view zenith angle, and scattering angle. The 74 mixtures are formed by combining up to three components with discrete mixing fractions [22]. Each component is characterized by a lognormal size distribution, prescribed complex refractive indices, and spherical or nonspherical shape. Common components include nonabsorbing or absorbing particles, small or medium/large sized particles, and spherical and nonspherical (dust) particles. This discretization transforms a continuous aerosol retrieval into a highly efficient search of the best solution(s) among the prescribed candidate mixtures. Overall, about 70% to 75% of MISR AOD retrievals fall within 0.05 or 20%×AOD of the coincident AERONET validation data, and about 50% to 55% are within 0.03 or 10%×AOD of AERONET, except at sites where dust or mixed dust-smoke conditions are prevalent [174]. The current version of MISR Level-2 aerosol product is reported on a 4.4 km spatial grid, or "region". Each region is composed of 4×4 subregions (hereafter referred to as "pixels"), each covering an area of 1.1 km. The Level-2 aerosol retrieval uses three types of cloud masks: the radiometric camera-by-camera cloud mask (RCCM, [177], [178]), the stereoscopically derived cloud mask (SDCM, [148]), and the angular signature cloud mask (ASCM, [179]). These masks are reported at the 1.1 km spatial resolution. In addition, angle-to-angle smoothness and angle-to-angle correlation are evaluated to further screen the pixels that may be cloud contaminated [173]. In addition to excluding the pixels contaminated by clouds or, over water, affected by sun glint, no aerosol retrievals are attempted over land when the surface topography is complex.

MISR's aerosol retrieval over land capitalizes on the spatial contrast in the region composed of 4×4 pixels. The darkest pixel is picked from such a region for fitting, and the maximum AOD is determined as the upper bound AOD for each aerosol mixture. Mixture-dependent AODs that are incompatible with the observed data are eliminated. For each combination of AOD and aerosol mixture, the LUT-derived path radiances are subtracted from the measurements. If a combination of aerosol model and AOD is correct, the residual corresponds to the surface Hemispherical-Directional Reflectance Factors (HDRFs), which should further satisfy the spectral invariance constraint in terms of the angular shape of the surface HDRFs. AOD-mixture combinations are rejected if they violate the spectral invariance constraint beyond a specified threshold metric. This process eliminates poorly fitting mixtures and narrows the range of acceptable optical depths in the remaining mixtures. Moreover, MISR's aerosol retrieval over land is characterized by the application of a "HetSurf" algorithm [173]. Empirical orthogonal functions (EOFs) are calculated from the reflectance differences between the TOA signals of the pixel of smallest mean of $\cos^{-1}q_{\mathrm{view}}$-weighted reflectance over the cameras in red band and those of other pixels in the 4×4-pixel region. This procedure enables an empirical decoupling of atmospheric path radiance from surface-leaving radiance. The surface reflectance is then reconstructed from the leading EOFs, and its deviation from the model-corrected surface reflectance is evaluated. The model-corrected surface reflectance is obtained by subtracting the modeled path radiance from the measured signals for each combination of AOD and aerosol mixture. Using a chi-square error metric to quantify the deviation, an AOD-aerosol mixture combination is rejected if the corresponding chi-square value exceeds a prescribed threshold.

The final reported AOD is typically derived from the ensemble of acceptable mixtures that survive all of the above screening criteria, rather than from a single best-fit solution, thereby reducing sensitivity to discrete LUT spacing and measurement noise. One strength of MISR's aerosol retrieval algorithm lies in its treatment of surface reflectance. Instead of assuming a constant surface albedo, MISR exploits the constraint that the angular shape of surface HDRFs does not vary significantly across its visible-to-near-IR spectral bands [172], [180]. Combined with the "HetSurf" algorithm, this approach reduces ambiguity between surface BRDF and atmospheric scattering contributions and retrieves reliable AOD over bright land, and sensitivity to particle shape.

For aerosol retrieval over dark water, however, there is no need to perform "HetSurf" algorithm through EOF analysis, as large water bodies (e.g., the open ocean) typically exhibit uniform contrast. Using the pair of red (672 nm) and near-IR (866 nm) bands to retrieve aerosols, the water-leaving reflectance is negligible and the spectral invariance constraint on the depolarizing surface reflection is turned off. In this case, the top-of-atmosphere (TOA) reflectance at non-glint viewing angles is fitted directly. To calculate radiative transfer in a coupled ocean-atmosphere system, wind-driven ocean surface roughness must be accounted for. This is achieved using the Cox-Munk model [181], which represents surface roughness with a Gaussian distribution of facet slopes whose variance depends on the near-surface wind speed. In addition, an empirical parameterization of wave shadowing effects [182] is included to model the bidirectional reflectance factor. The modeled radiances for all combinations of aerosol mixtures and AODs are compared with the actual measurements. Using several types of goodness-of-fit metrics, the successful aerosol mixture(s) and associated AOD(s) are identified [171].

B. Examples of Aerosol Retrieval Products based on MISR Observations

Figure 35 demonstrates an example of MISR seasonal climatology of AOD for Year 2021. The spatial patterns exhibit pronounced seasonal variability consistent with known aerosol source regions and transport regimes. Elevated AOD is observed over North Africa and the Middle East during boreal summer, associated with intensified Saharan dust emissions and westward trans-Atlantic transport. In boreal fall, enhanced AOD appears over southern Africa and South America, reflecting biomass burning activity. Wintertime maxima shift toward equatorial Africa and South Asia, where anthropogenic emissions and seasonal burning contribute to increased column loading. Overall, the seasonal migration of high-AOD regions follows the climatological displacement of major dust and biomass-burning sources.

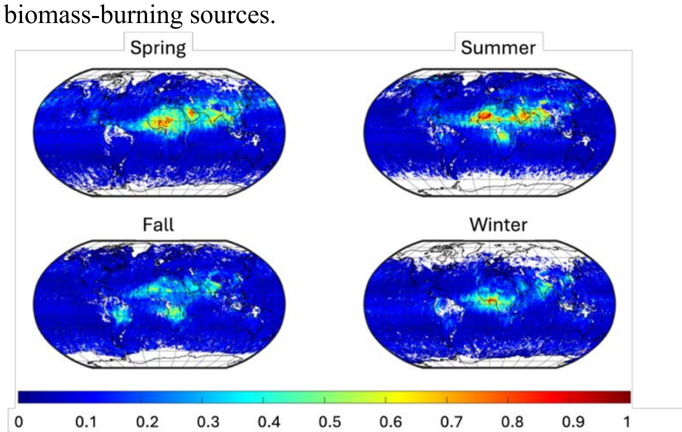

Fig. 35. Seasonal mean global distribution of MISR-retrieved AOD at 555 nm for 2021. Panels show the results for the northern hemisphere spring, summer, fall, and winter, respectively. Courtesy of Wenzhi Zhang, University of Oklahoma.

Although multi-angular observations provide strong constraints on aerosol microphysical properties, some limitations remain. For example, multi-angle radiometric measurements in 446, 558, 672, and 866 nm bands do not ensure sufficient sensitivity to aerosol absorption, particularly for mixtures containing black and brown carbon. Indeed, enhanced sensitivity to aerosol absorption can be achieved through ultraviolet observations, which increase Rayleigh scattering contrast, while polarimetric measurements add independent constraints on particle size, shape, and complex refractive index, thereby increasing retrieval information content. These capabilities are provided by some advanced multi-angle Spectro-polarimetric instruments, such as the Multi-Angle Imager for Aerosols (MAIA; [183]), which extends spectral coverage into the ultraviolet and incorporates polarization measurements. By integrating multi-angle, ultraviolet, and polarimetric observations, the information content is substantially enhanced, enabling retrieval over a more continuous parameter space. This also represents a significant advancement over MISR's LUT-based aerosol retrieval, in which aerosol properties are represented by a finite set of predefined mixtures whose physical characteristics, including components, size distribution, and refractive index, are prescribed based on climatology [184].

X. POLARIMETRIC REMOTE SENSING OF AEROSOL PROPERTIES

The previous sections focus primarily on remote sensing techniques for inferring cloud and aerosol properties based on radiometric observations of electromagnetic radiation. However, an electromagnetic wave is a vector wave, and the direction of the electric vector determines its polarization. Four Stokes parameters, I, Q, U, and V can be used to specify the polarization state of a radiation field [185]. It is worth noting that two radiation beams are indistinguishable by an optical instrument if they have the same Stokes parameters [186]. Polarimetric observations of clouds and aerosols provide much more information about these atmospheric constituents compared to radiometric observations (i.e., observations associated with the first Stokes parameter, or radiance). In this section, we demonstrate the strengths of polarimetric remote sensing techniques in the case of aerosol property retrievals.

Solar radiation incident at the top of the atmosphere is unpolarized. After interacting with atmospheric molecules, aerosols, and clouds, the scattered radiation becomes partially polarized. Multi-angle polarimetry exploits both the angular and polarization dependence of light scattering to retrieve aerosol optical and physical properties that are difficult to constrain with intensity-only measurements. Polarimetric measurements of the Stokes vector components I, Q, and U provide additional constraints on particle size, shape, and complex refractive index, improving the retrieval accuracy of aerosol physical properties, especially those related to aerosol composition and absorption. Combined with extended spectral coverage from ultraviolet to shortwave, this approach can further increase sensitivity to absorbing aerosols and coarse-mode particles.

A. Optimization-Based Inversion for Polarimetric Aerosol Retrieval

State-of-art polarimeters as well as the deployed algorithms are reviewed in [187]. Building upon the success of AirHARP [188] and the airborne SPEX spectropolarimeter [189], NASA's Plankton, Aerosol, Cloud, ocean Ecosystem mission (PACE; [190]) deploys two polarimeters: the Hyper-Angular Rainbow Polarimeter-2 (HARP2; [191]) and the Spectro-Polarimeter for Planetary Exploration (SPEXone; [192]), to complement the hyperspectral measurements from the Ocean

Color Instrument (OCI; [193]). HARP2 provides wide-swath, hyper-angular measurements, whereas SPEXone delivers high-accuracy hyperspectral polarimetric observations. The synergy between SPEXone and HARP2 increases the information content for aerosol characterization and reduces uncertainties in atmospheric correction for water-leaving reflectance, thereby improving the accuracy of derived ocean color products.

Numerical experiments and real data analyses have been performed to assess the quantitative benefits of multi-angle spectro-polarimetry. For example, Xu et al. [194] conducted aerosol retrievals using multiple field campaign datasets acquired by NASA Jet Propulsion Laboratory's Airborne Multiangle SpectroPolarimetric Imager (AirMSPI; [195]). Comparisons of AOD and SSA with AERONET reference data show that retrieval accuracy improves as the number of viewing angles increases. As demonstrated in Fig. 36, substantial gains in AOD and SSA accuracy are achieved when increasing the number of angles from two to five. However, smaller improvements are obtained when more than five viewing angles are used. Moreover, excluding polarimetric measurements results in a significant loss of AOD and SSA retrieval accuracy. Such a magnitude of improvement has also been observed earlier in [196], [197] through theoretical studies and analyses of polarimetric data acquired by NASA Goddard Institute for Space Studies (GISS)'s Research Scanning Polarimeter [198], respectively.

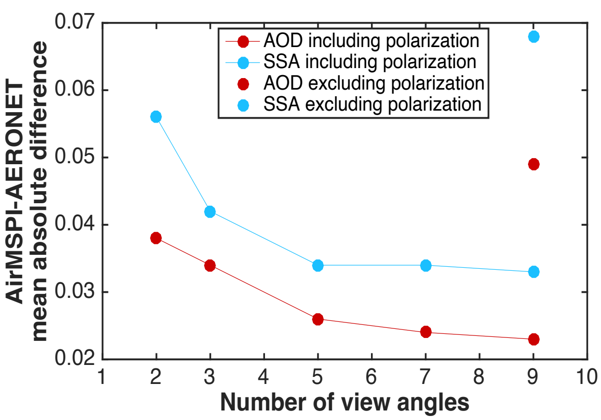

Fig. 36. Dependence of AOD and SSA retrieval accuracy on number of view angle and polarimetry. The analyses are based on AirMSPI field data collected from multiple airborne campaigns [194].

Optimization-based approaches are widely used to exploit the information content of multi-angle spectro-polarimetric observations for aerosol property retrieval. These methods formulate the problem as a nonlinear inverse problem constrained by observations:

$$y_i^* = f_i(\mathbf{x}) + \varepsilon_i, \tag{68}$$

where y_i^* includes i^{th} measured multi-angle signal such as radiance (L), linear polarimetric components $q=Q/L$, $u=U/L$, $\mathbf{x}$ is the retrieval state vector that typically includes a set of geophysical quantities to which the polarimetric measurements have sensitivity, and ε_i is the measurement error. To fit observation, the vector radiative transfer forward equation needs to be solved to obtain $f_i(\mathbf{x})$. As a sensitive set of parameters, $\mathbf{x}$ typically includes aerosol properties such as aerosol concentrations, size distribution, shape, complex refractive index, aerosol layer height and width of distribution, and a set of parameters that govern the surface bidirectional reflectance factors. However, traditional optimization approaches face many confounding issues. Among the main challenges to overcome are non-uniqueness of the solutions. Although multi-angle polarimetry carries more information about aerosol properties than does the radiometry and explores the solution in continuous parameter space, it still cannot guarantee a globally optimized solution to be found. Insufficient information in the observations leads to non-uniqueness of the solutions. To stabilize the inversion process, optimization is often informed by extra constraints to supplement the observations. Exploration of these constraints is a primary task in designing reliable inversion. A particularly effective type of constraint applied to remote sensing inversion is the so-called smoothness condition (see [199], [200], [201], [202], [203]), which takes advantage of the general observation that some targeted geophysical quantities vary smoothly in one or more dimensions. For aerosols, their loading and their properties such as size distribution and refractive index tend to vary more smoothly in the horizontal dimension compared to the underlying surface. Moreover, the surface reflectance tends to vary smoothly in the temporal dimension. Imposition of these smoothness constraints leads to the "multi-pixel" inversion approach [204].

To impose a priori constraints, optimization-based inversion algorithms have been advanced for polarimetric aerosol retrieval. For the n^{th} type of constraint, the retrieval state vector $\mathbf{x}$ must satisfy

$$\boldsymbol{f}_n^* = \boldsymbol{f}_n(\boldsymbol{x}) + \Delta \boldsymbol{f}_n^*, 1 \le n \le N, \tag{69}$$

where $\mathbf{f}_n^*$ denotes the n^{th} type of constraint (observational or physical) expressed as a function of the state vector $\mathbf{x}$, and $\Delta\mathbf{f}_n^*$ denotes the associated error term. Assuming the imposed constraints to be statistically independent, their joint covariance matrix is diagonal, and $\mathbf{f}^*=[\mathbf{f}_1^*; \mathbf{f}_2^*; \ldots; \mathbf{f}_N^*]$. Including all N types of constraints in a retrieval leads to a quadratic form of the objective cost function to be minimized [205], namely:

$$\Psi_{\text{total}}(\mathbf{x})=\sum_{n=1}^{N} \gamma_n \Psi_n(\mathbf{x}), \tag{70}$$

where the Lagrange factor γ_n weights the contribution of n^{th} type of constraint through $\Psi_n=[\mathbf{f}_n(\mathbf{x}) - \mathbf{f}_n^*]^{\mathrm{T}}\mathbf{C}_n^{-1}[\mathbf{f}_n(\mathbf{x}) - \mathbf{f}_n^*]$, where $\mathbf{C}_n$ is the covariance matrix.

Minimization of $\Psi_{\text{total}}(\mathbf{x})$ in Eq. (55) implies that its gradient with respect to the solution $\mathbf{x}$ approaches zero, namely,

$$\nabla\Psi_{\text{total}}(\mathbf{x}) = \sum_{n=1}^{N} \gamma_n \nabla\Psi_n(\mathbf{x}) = \mathbf{0}, \tag{71}$$

which can be ensured by enforcing the gradient of all components approaches zero:

$$\nabla\Psi_n(\mathbf{x}) = \mathbf{K}_n^T \mathbf{W}_n^{-1}(\boldsymbol{f}_n(\mathbf{x}) - \boldsymbol{f}_n^*) = \mathbf{0}, \tag{72}$$

where $\mathbf{K}_n$ is the Jacobian matrix.

To solve the above equation iteratively, we replace $\mathbf{x}$ by $\mathbf{x} - \Delta\mathbf{x}$ and substitute

$$\boldsymbol{f}_n(\mathbf{x} - \Delta\mathbf{x}) = \boldsymbol{f}_n(\mathbf{x}) - \mathbf{K}_n\Delta\mathbf{x} \tag{73}$$

into the above equation. This results in

$$\nabla\Psi_n(\mathbf{x}-\Delta\mathbf{x}) = \mathbf{K}_n^T\mathbf{W}_n^{-1}(\boldsymbol{f}_n(\mathbf{x}) - \mathbf{K}_n\Delta\mathbf{x} - \boldsymbol{f}_n^*) = \mathbf{0} \quad (74)$$

or equivalently,

$$(\mathbf{K}_n^T\mathbf{W}_n^{-1}\mathbf{K}_n)\Delta\mathbf{x} = \mathbf{K}_n^T\mathbf{W}_n^{-1}(\boldsymbol{f}_n(\mathbf{x}) - \boldsymbol{f}_n^*) = \nabla\Psi_n(\mathbf{x}). \quad (75)$$

The Jacobian matrix $\mathbf{K}_n$ in (72)-(75) consists of the derivative of the l-th observational or *a priori* data with respect to the i-th unknown:

$$K_{n,(l,i)} = \frac{\partial f_{n,l}}{\partial x_i}. \quad (76)$$

Accounting for all types of constraints, the following linear system of equations can be established to solve for the increment of a state vector Dx during an iterative step of optimization:

$$\left[\sum_{n=1}^{N}(\mathbf{K}_n^T\mathbf{W}_n^{-1}\mathbf{K}_n)\right]\Delta\mathbf{x} = \sum_{n=1}^{N}\mathbf{K}_n^T\mathbf{W}_n^{-1}(\boldsymbol{f}_n(\mathbf{x}) - \boldsymbol{f}_n^*). \quad (77)$$

B. Example of Aerosol Retrieval based on Polarimetric Observations

Figure 37 presents a representative example of aerosol retrieval using the optimization approach described above, applied to POLDER/PARASOL observations acquired on February 4, 2013. POLDER/PARASOL measures the angular distribution of radiances and linear polarization in three bands centered at 490, 670, and 865 nm, and radiances only in another three bands centered at 443, 565, and 1.020 nm. The number of viewing angles ranges from 14 to 16, depending on the geographic location of the observation. The spatial resolution is 5.3 × 6.2 km at nadir. Figures 37a and 37b show representative radiance and degree-of-linear-polarization images, respectively, over the Southern California region. The retrieved AOD map is demonstrated in Fig. 37c. Comparisons of the retrieved spectral AOD, SSA, and size distribution with the reference data provided by the AERONET DRAGON site at Porterville are made in Figs. 37d-37f, respectively. The comparison indicates good agreement in AOD. The differences in retrieved SSA are within 0.02-0.03, which lies within the reported AERONET uncertainty [206]. For the size distribution, the two modes are generally comparable. However, a noticeable discrepancy in the concentration of coarse-mode aerosols is observed, due to the lower measurement sensitivity to coarse-mode particles compared to fine-mode aerosols. When converted to number-weighted size distributions, the number concentration of coarse-mode particles is significantly smaller, which reflects the limited sensitivity of polarimetric observations to this mode.

While polarimetry enhances sensitivity to aerosol microphysical and surface reflection properties, such sensitivity does not necessarily translate into independent

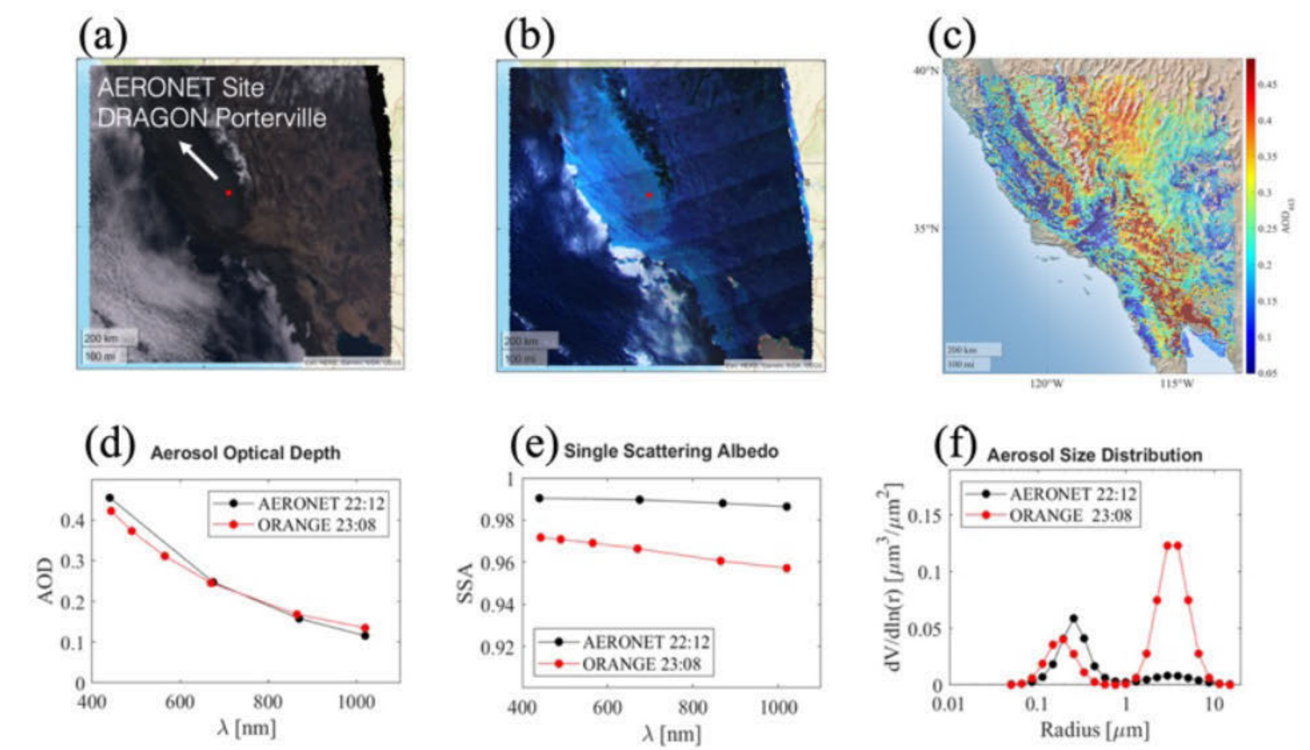

Fig. 37. Radiometric (a) and degree of linear polarization (DOLP, b) images of Southern California region made by POLDER/PARASOL on Feb 04 of 2013. The two images are from spectral combination of three bands centered at (490, 565, 670) nm and (490, 670, 865) nm, respectively. The retrieved AOD map is displayed in (c). In (d-f), comparisons of the retrieved AOD, SSA, and volumetric size distribution are made to the reference data reported by the AERONET DRAGON site at Porterville, whose location is marked by the red dot in a) and b). The retrieval uses the optimization-based aerosol retrieval algorithm developed by Xu et al. [194]. Courtesy of Benting Chen, University of Oklahoma.

parameter retrievability. Strong correlations among state vector elements can lead to limited effective degrees of freedom for the signal, as revealed by information content analysis. In practice, simplifications are often made to improve the robustness and accuracy of some key retrieval parameters, such as AOD and SSA. For example, the current version of the GRASP algorithm provides an option of component-based aerosol retrieval [207], [208]. In this framework, five main aerosol types are predefined, each with known size distributions and refractive indices [209]. The optimization procedure then determines their relative fractions. This approach allows multiple aerosol types to be retrieved simultaneously, reduces the dimensionality of the retrieval problem, and improves the accuracy of AOD estimation. Xu et al. [210] capitalized on the spatial and temporal correlations of aerosol properties to constrain the inversion and developed a correlation-based aerosol retrieval approach. Instead of directly retrieving aerosol microphysical properties, the correlation-based method determines the weights and elements of a small number of principal components that capture the dominant spatial-temporal variability of aerosol properties over a targeted area, thereby reducing the retrieval parameter space and improving the algorithm stability. Preliminary applications of this approach to ground-based AERONET observations [211], AirMSPI observations [210], and POLDER observations [212] demonstrate reasonable accuracy. Figure 38 compares AOD retrieved using the GRASP component-based configuration and the correlation-based inversion against collocated AERONET observations. Both approaches show consistent positive correlations across all wavelengths, indicating overall robustness of the retrieval framework. The component-based configuration generally achieves higher correlation coefficients at shorter wavelengths (440 and 670 nm), whereas the correlation-based approach exhibits comparable dispersion and similar error magnitudes across the spectrum. In both methods, slopes below unity indicate a systematic underestimation at higher AOD levels.

Due to the nonlinear nature of polarimetric aerosol inversion, the state vector must be iteratively adjusted during the optimization process. In the early development stage of optimization-based inversion algorithms, the retrieval process is computationally expensive because vector radiative transfer calculations must be repeated multiple times to match the measurements. Moreover, the Jacobian matrix is required to determine the updated direction and step size of the search, which further increases the computational burden. To accelerate the retrieval, machine-learning-based RT (NN-RT) models have been developed to approximate the physical RT model for calculating the Stokes vector components. Without essential loss of retrieval accuracy, NN-RT models have been proven to enhance retrieval efficiency by several orders of magnitude [213]. In this approach, a dataset that contains many training samples that combines aerosol and surface parameters and Sun/view geometry are generated using any traditional RT model. Once trained, Stokes parameters of TOA-leaving light

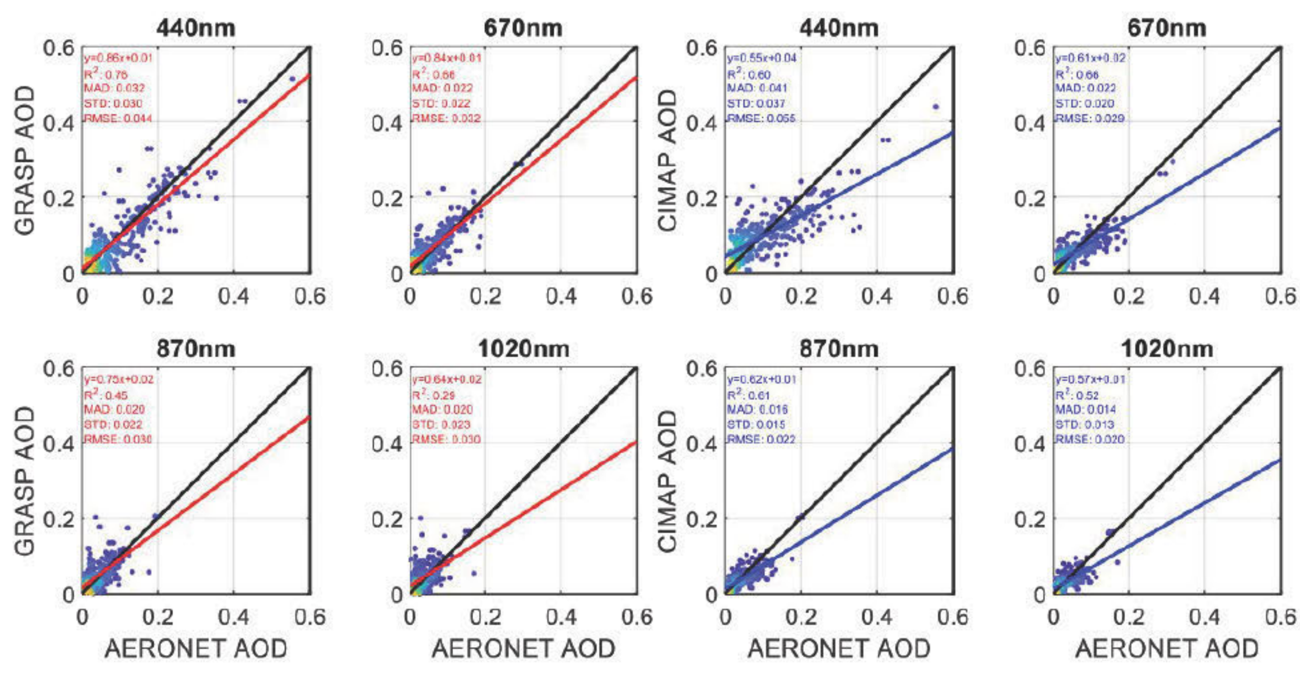

Fig. 38. Comparison of AOD retrieved using the GRASP component-based configuration (left four panels) and the correlation-based inversion (right four panels) against collocated AERONET data at the sites along the west coast of the United States (2008–2011). Results are shown for 440, 670, 870, and 1020 nm. The solid lines indicate linear regression fits, and statistical metrics including slope, coefficient of determination (R^2), mean absolute difference (MAD), standard deviation of the differences (STD) between retrieval and AERONET, and root mean square error (RMSE) are reported in each panel. Courtesy of Joe Huang, University of Oklahoma.

and the Jacobian matrix are obtained analytically from the trained RT model coefficients. Using the same approach, light scattering calculations are trained using random combinations of aerosol properties to calculate single scattering properties, including AOD, SSA and phase matrix.

C. Current Challenges and Outlook

Over the past few decades, aerosol retrieval algorithms for multi-angle radiometry and polarimetry have advanced significantly. Nevertheless, several fundamental challenges persist. For example, the RT simulations underlying most operational aerosol retrieval algorithms make the plane-parallel atmosphere assumption and adopt simplified particle geometries (e.g., spheres or spheroids). While these approximations enable computational efficiency and global-scale application, they inherently limit the ability to represent the full three-dimensional (3D) variability of aerosol fields and the complexity of particle morphology encountered in realistic atmospheric conditions. In many situations, aerosol distributions are often highly heterogeneous in space and time. For example, smoke plumes from wildfires, volcanic emissions, and urban outflows exhibit strong horizontal gradients, vertical layering, and complex interactions with boundary-layer dynamics. Under such conditions, the assumption of horizontal homogeneity in plane-parallel RT calculation can introduce biases in both aerosol abundance and microphysical retrievals. Simplified particle shape representations are often inadequate for describing aggregated soot particles, fractal-like smoke aerosols, or irregular dust mixtures, leading to uncertainties in absorption, phase function, and polarization signatures.

To accurately resolve aerosol 3D structure and microphysical complexity, enhanced observational and modeling strategies are required. First, synergistic use of complementary measurements is essential. For example, the integration of multi-angle polarimetry with hyperspectral observations increases sensitivity to aerosol absorption, composition, and its vertical profile. Coupling spaceborne sensors with lidar and sun-photometer measurements provides further vertical constraints that are otherwise insufficiently determined from passive measurements alone. Second, the incorporation of physically consistent a priori information, such as aerosol transport model outputs, chemical transport simulations, and climatological constraints, can help stabilize inversions and reduce solution non-uniqueness. Third, advances in RT modeling are necessary, including the development of efficient 3D vector radiative transfer solvers capable of accounting for spatial inhomogeneity effects. Improved representation of particle morphology is another critical frontier. For example, for the combustion-derived aerosols, particularly wildfire smoke, fractal aggregate models may better capture scattering and polarization behavior than conventional spheroidal approximations. Incorporating such physically realistic scattering models into inversion frameworks will enhance retrieval fidelity for absorbing aerosols. These advancements are also particularly important for emerging research topics such as aerosol-cloud joint retrieval, constituting a critical step towards quantitative investigation of aerosol-cloud interactions. In smoke-plume environments or partially cloudy scenes, aerosol and cloud microphysics are strongly coupled, and independent retrieval assumptions may break down. Joint inversion frameworks that simultaneously retrieve aerosol and cloud properties using multi-sensor observations and advanced RT models represent a promising pathway forward.

In our opinion, future progress in aerosol remote sensing will likely focus on the convergence of enhanced measurement diversity (polarimetric, hyperspectral, multi-platform, active-passive integration), physically informed a priori constraints, advanced 3D radiative transfer modeling, and improved particle scattering physics. Such developments will move the field beyond column-averaged characterization toward more physically consistent reconstruction of aerosol spatial structure and its interaction with clouds and radiation in three-dimensional space.

XI. ACTIVE REMOTE SENSING

In the above discussions, we primarily focus on reviewing several passive remote sensing techniques for inferring cloud and aerosol properties. Active remote sensing techniques based on spaceborne lidar observations offer unique capabilities that are not readily achievable with passive observations. To demonstrate the strengths of active remote sensing techniques, Fig. 39 shows the correlation between the layer-integrated attenuated backscatter (γ') and the layer-integrated depolarization ratio (δ) observed by CALIOP lidar during August 2006. The left panel of Fig. 39 shows the schematic correlation of these two parameters, whereas the right panel shows the data. γ' and δ are defined as [214]:

$$\delta = \frac{\int_{\text{cloud base}}^{\text{cloud top}} \beta'_{\perp}(z)\,\mathrm{d}z}{\int_{\text{cloud base}}^{\text{cloud top}} \beta'_{\parallel}(z)\,\mathrm{d}z}, \tag{78}$$

$$\gamma' = \int_{\text{cloud\_base}}^{\text{cloud\_top}} \frac{\beta'_{\perp}(z)}{\cos\theta_{\text{off-nadir}}}\,\mathrm{d}z + \int_{\text{cloud\_base}}^{\text{cloud\_top}} \frac{\beta'_{\parallel}(z)}{\cos\theta_{\text{off-nadir}}}\,\mathrm{d}z, \tag{79}$$

where $\beta'_{\parallel}(z)$ and $\beta'_{\perp}(z)$ indicate the variations of the parallel and perpendicular components of attenuated backscatter versus altitude. $\theta_{\text{off-nadir}}$ indicates the title angle of the lidar laser beam from the nadir. The CALIOP laser beam was pointed with an angle of 0.3° from the nadir before November 2007 but was subsequently tilted at 3° from the nadir to avoid strong backscattering signals associated with horizontally oriented ice crystals [215].

For water clouds, the single-scattering of individual droplets is given by the Lorenz-Mie theory, and the depolarization ratio is zero in the backscattering direction. However, multiple scattering by droplets leads to nonzero backscattering depolarization, and the signal strength increases with water cloud optical thickness. The correlation between the layer-integrated attenuated backscatter (γ') and layer-integrated depolarization ratio (δ) is quite different for water and ice clouds, as shown in Fig. 39. This feature allows robust distinction of cloud thermodynamic phases, and an effective algorithm has been developed [215].

Horizontally oriented pristine ice crystals (primarily plates and columns) lead to small backscattering depolarization ratio but strong backscatter signals, whereas the opposite scenario is observed for randomly oriented ice crystals. Based on this feature of the δ - γ' correlation, it was estimated [216] that horizontally oriented ice crystals exist in approximately 88%, 84% and 29% of optically thick (optical thickness > 3) ice and mixed-phase clouds with temperatures higher than -30°C, between -30°C and -45°C, and below -45°C, respectively. Furthermore, it was estimated [214] that 0-6%, 0-3%, and 0-0.5% of ice crystals are quasi-horizontally oriented plates in war optically thick mixed-phase clouds, warm (T>-35°C) ice clouds, and cold (T<-35°C) ice clouds, respectively. These findings were unlikely to be achieved using passive remote sensing observations.

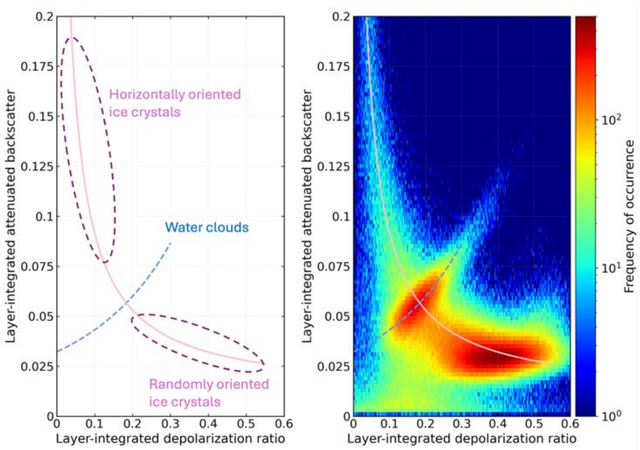

Fig. 39. Correlation between the layer-integrated attenuated backscatter (γ') and layer-integrated depolarization ratio (δ) observed by CALIOP lidar during August 2006 when the lidar laser beam was tilted off the nadir.

XII. CONCLUSIONS

Satellite optical remote sensing of clouds and aerosols is fundamentally rooted in electromagnetic scattering theory. While light scattering by homogeneous spheres is accurately described by Lorenz-Mie theory, the Earth's atmosphere contains complex, nonspherical, and inhomogeneous particles, such as ice crystals, mineral dust, and internally mixed aerosols. We have reviewed significant advances in numerical computation of electromagnetic scattering for calculating the scattering of nonspherical and inhomogeneous particles across a broad size-parameter spectrum, including FDTD/PSTD, DDA, T-matrix, separation-of-variables methods, invariant-imbedding techniques, and physical-geometric optics approaches. Nevertheless, no single computational method spans the full range from the Rayleigh-to-geometric-optics regime with uniform efficiency and accuracy. In practice, current remote sensing frameworks rely on hybrid strategies that combine rigorous solutions for small-to-moderate size parameters with geometric-optics approximations for large particles. Developing computationally efficient methods that accurately capture diffraction, interference, and surface-wave effects in the intermediate-size-parameter regime across the entire scattering angular range remains a central challenge in electromagnetic scattering theory.

Single-particle scattering properties form the foundation of radiative transfer modeling, which further couples the treatment of scattering, absorption, and thermal emission, and accounts for interactions among molecules, aerosols, cloud particles, and underlying surface. Cloud and aerosol remote sensing is therefore not merely an inversion problem, but a multi-scale physical synthesis that links particle morphology, bulk microphysical properties, scattering properties, and radiative transfer. Operational cloud retrievals based on visible and shortwave IR bi-spectral techniques, such as the Nakajima-King approach implemented in operational algorithms for instruments like MODIS and ABI, exploit differential absorption to infer cloud optical thickness and effective particle size under daylight conditions. The IR split-window and emissivity-ratio techniques complement these methods by enabling day-night retrievals and enhancing sensitivity to optically thin cirrus. However, systematic discrepancies between solar-band and IR-based retrievals, particularly for ice clouds, highlight the sensitivity of inferred properties to assumed particle habit, surface roughness, and vertical inhomogeneity. These differences underscore the need for spectrally consistent ice optical models applicable across both solar and thermal regimes.

On the other hand, aerosol retrieval algorithms developed for MODIS and MISR have established a methodological benchmark for passive multispectral remote sensing. They have enabled long-term monitoring of aerosol loading, transport, and radiative impacts. The transfer, adaptation, and advancement of these algorithms to subsequent platforms demonstrate their enduring legacy. Similarly, active-passive synergy from CALIPSO has expanded constraints on aerosol physical and vertical properties. These developments illustrate how advances in physical modeling translate into robust operational aerosol and cloud products and multi-decadal climate data records.

Despite substantial progress, several scientific and methodological challenges remain. For example, many retrieval systems rely on plane-parallel or single-layer assumptions that are insufficient for mixed-phase or three-dimensional cloud and aerosol plume structures. In addition, uncertainties in particle morphology, internal mixing state, and vertical distribution continue to limit accurate characterization of aerosol absorption and scattering effects, as well as ice cloud radiative effects. In addition, inconsistencies among retrieval algorithms and across spectral regimes or platforms indicate the need for unified particle models that are simultaneously consistent with polarimetric, radiometric, active, and thermal observations.

Future advances will likely emerge from integrated observational and modeling architectures. Polarimetric measurements provide enhanced sensitivity to particle shape and refractive index. Multi-angle and hyperspectral observations offer improved separation of surface and atmospheric contributions, as well as of spherical and non-spherical particles, and provide improved information about atmospheric composition and distribution height. Synergistic use of passive imagers with active lidar and radar instruments can better constrain vertical layering and three-dimensional structure. At the theoretical level, continued development of spectrally consistent single-scattering databases and more computationally efficient semi-classical electromagnetic solvers will strengthen the physical foundation of retrieval algorithms. Ultimately, the goal is a unified, physically consistent framework linking electromagnetic scattering, radiative transfer, satellite inversion methodologies, and climate applications.

By connecting fundamental scattering physics with operational satellite retrieval systems and long-term climate data records, optical remote sensing of clouds and aerosols exemplifies the interplay between theoretical rigor and practical implementation. Continued progress will depend on sustained collaboration across electromagnetic scattering, radiative transfer, inversion algorithm development, instrument design, and Earth science measurement users. Achieving a unified and spectrally consistent representation of atmospheric particles, applicable across sensors, platforms, and modeling communities, remains a central objective for advancing quantitative understanding of the Earth's radiation balance and its response to natural variability and anthropogenic change.

The present review primarily focuses on classical, well-established remote sensing theories and techniques grounded in rigorous physical principles. However, we are now entering an era in which artificial intelligence (AI) is increasingly enabling advances in atmospheric remote sensing. For example, traditional retrieval algorithms typically rely on iterative inversion, repeatedly calling computationally expensive light-scattering and radiative-transfer models. Alternatively, they compare observations with pre-computed look-up tables to retrieve cloud and aerosol properties from passive or active observations. While these approaches are physically transparent and well validated, they can be computationally intensive. It is also difficult to apply them to the rapidly increasing volume of satellite data arising from high-resolution spectral, spatial, and temporal observations. AI-based methods, particularly those based on machine learning and deep learning, are beginning to reshape the retrieval paradigm by enabling fast, data-driven inference and efficient processing of large datasets. These approaches have demonstrated strong potential to accelerate forward modeling and to directly retrieve geophysical parameters from observations. Moreover, AI provides new opportunities for synergizing the use of multi-sensor data (e.g., passive and active measurements; satellite-based and in-situ measurements). It also enables the capture of complex nonlinear relationships that are difficult to represent in traditional frameworks.

Despite these promising advances, several fundamental challenges remain. For example, many AI models lack physical transparency and have limited physical interpretability, reducing user confidence in operational applications. In many situations, their performance is sensitive to the configuration parameters used in the training process. It often degrades when applied outside the training domain (e.g., under conditions not fully represented in the training datasets). Furthermore, AI-based approaches depend on the quality and representativeness of synthetic or observational training data. Biases in the training datasets can propagate into remote sensing inversion. Ensuring physical consistency with remote sensing theory remains an active area of research. Looking forward, physics-based remote sensing theory and modeling remain the foundation, while AI acts as an enabler and accelerator. Their synergy will shape the next generation of remote sensing methodologies. A promising direction, for example, is the integration of physics-based modeling and AI. This includes hybrid approaches such as physics-informed neural networks and machine-learning-assisted inversion frameworks. These methods can combine the interpretability and robustness of traditional radiative transfer-based retrievals with the efficiency and flexibility of AI. The reader is referred to Boukabara et al. [217] and Yuan et al. [218] for further discussion of the opportunities and challenges associated with the applications of AI in atmospheric and environmental remote sensing.

ACKNOWLEDGMENT

Xu Liu from NASA Langley Research Center helped summarize the principal component radiative transfer model. Jian Wei and Siheng Wang from Texas A&M University, and Benting Chen, Joe Huang, and Wenzhi Zhang from the University of Oklahoma assisted with the preparation of several figures used in the paper. Steven Schroeder helped edit the manuscript.

REFERENCES

[1] W. B. Rossow, K. R. Knapp, and A. H. Young, "International satellite cloud climatology project: Extending the record," *J. Clim.*, vol. 35, no. 1, pp. 141–158, 2022.

[2] C. J. Stubenrauch *et al.*, "Assessment of global cloud datasets from satellites: Project and database initiated by the GEWEX radiation panel," *Bull. Am. Meteorol. Soc.*, vol. 94, no. 7, pp. 1031–1049, 2013.

[3] K. Sassen, Z. Wang, and D. Liu, "Cirrus clouds and deep convection in the tropics: Insights from CALIPSO and CloudSat," *Journal of Geophysical Research: Atmospheres*, vol. 114, no. D4, 2009.

[4] W. B. Rossow and R. A. Schiffer, "Advances in understanding clouds from ISCCP," *Bull. Am. Meteorol. Soc.*, vol. 80, no. 11, pp. 2261–2288, 1999.

[5] S. A. Klein, Y. Zhang, M. D. Zelinka, R. Pincus, J. Boyle, and P. J. Gleckler, "Are climate model simulations of clouds improving? An evaluation using the ISCCP simulator," *Journal of Geophysical Research: Atmospheres*, vol. 118, no. 3, pp. 1329–1342, 2013.

[6] L. Lorenz, *Lysbevægelsen i og uden for en af plane Lysbølger belyst Kugle*. na, 1890.

[7] G. Mie, "Beiträge zur Optik trüber Medien, speziell kolloidaler Metallösungen," *Ann. Phys.*, vol. 330, no. 3, pp. 377–445, 1908.

[8] R. P. Lawson, A. V Korolev, S. G. Cober, T. Huang, J. W. Strapp, and G. A. Isaac, "Improved measurements of the drop size distribution of a freezing drizzle event," *Atmos. Res.*, vol. 47–48, pp.

181–191, 1998, doi: 10.1016/S0169-8095(98)00062-3.

[9] M. P. Bailey and J. Hallett, “A comprehensive habit diagram for atmospheric ice crystals: Confirmation from the laboratory, AIRS II, and other field studies,” *J. Atmos. Sci.*, vol. 66, no. 9, pp. 2888–2899, 2009, doi: 10.1175/2009JAS2883.1.

[10] K.-N. Liou and P. Yang, *Light scattering by ice crystals: fundamentals and applications*. Cambridge University Press, 2016.

[11] K. Liou and S. Ou, “The role of cloud microphysical processes in climate: An assessment from a one-dimensional perspective,” *Journal of Geophysical Research: Atmospheres*, vol. 94, no. D6, pp. 8599–8607, 1989.

[12] S. A. Twomey, M. Piepgrass, and T. L. Wolfe, “An assessment of the impact of pollution on global cloud albedo,” *Tellus B*, vol. 36, no. 5, pp. 356–366, 1984.

[13] B. A. Albrecht, “Aerosols, cloud microphysics, and fractional cloudiness,” *Science (1979).*, vol. 245, no. 4923, pp. 1227–1230, 1989.

[14] B. N. Holben *et al.*, “AERONET—A federated instrument network and data archive for aerosol characterization,” *Remote Sens. Environ.*, vol. 66, no. 1, pp. 1–16, 1998.

[15] M. D. King, Y. J. Kaufman, W. P. Menzel, and D. Tanre, “Remote sensing of cloud, aerosol, and water vapor properties from the moderate resolution imaging spectrometer(MODIS),” *IEEE transactions on geoscience and remote sensing*, vol. 30, no. 1, pp. 2–27, 1992.

[16] S. Platnick *et al.*, “The MODIS Cloud Optical and Microphysical Products: Collection 6 Updates and Examples from Terra and Aqua,” *IEEE Transactions on Geoscience and Remote Sensing*, vol. 55, no. 1, pp. 502–525, Jan. 2017, doi: 10.1109/TGRS.2016.2610522.

[17] P. Minnis *et al.*, “CERES MODIS Cloud Product Retrievals for Edition 4 - Part I: Algorithm Changes,” *IEEE Transactions on Geoscience and Remote Sensing*, vol. 59, no. 4, pp. 2744–2780, Apr. 2021, doi: 10.1109/TGRS.2020.3008866.

[18] P. Minnis *et al.*, “VIIRS Edition 1 Cloud Properties for CERES, Part 1: Algorithm Adjustments and Results,” *Remote Sens. (Basel).*, vol. 15, no. 3, p. 578, 2023, doi: 10.3390/rs15030578.

[19] A. Marshak *et al.*, “Aerosol properties in cloudy environments from remote sensing observations: A review of the current state of knowledge,” *Bull. Am. Meteorol. Soc.*, vol. 102, no. 11, pp. E2177–E2197, 2021, doi: 10.1175/BAMS-D-20-0225.1.

[20] R. C. Levy, L. A. Remer, and O. Dubovik, “Global aerosol optical properties and application to Moderate Resolution Imaging Spectroradiometer aerosol retrieval over land,” *Journal of Geophysical Research: Atmospheres*, vol. 112, p. D13210, 2007, doi: 10.1029/2006JD007815.

[21] N. C. Hsu *et al.*, “Enhanced Deep Blue aerosol retrieval algorithm: The second generation,” *Journal of Geophysical Research: Atmospheres*, vol. 118, pp. 9296–9315, 2013, doi: 10.1002/jgrd.50712.

[22] R. A. Kahn and B. J. Gaitley, “An analysis of global aerosol type as retrieved by MISR,” *Journal of Geophysical Research: Atmospheres*, vol. 120, no. 9, pp. 4248–4281, 2015.

[23] W. L. Smith and C. M. R. Platt, “Comparison of satellite-deduced cloud heights with indications from radiosonde and ground-based laser measurements,” *Journal of Applied Meteorology (1962-1982)*, pp. 1796–1802, 1978.

[24] T. Nakajima and M. D. King, “Determination of the optical thickness and effective particle radius of clouds from reflected solar radiation measurements. Part I: Theory,” *J. Atmos. Sci*, vol. 47, no. 15, pp. 1878–1893, 1990.

[25] H. C. Van de Hulst and V. Twersky, “Light scattering by small particles,” *Phys. Today*, vol. 10, no. 12, pp. 28–30, 1957.

[26] M. I. Mishchenko, L. D. Travis, and A. A. Lacis, *Scattering, Absorption, and Emission of Light by Small Particles*. Cambridge, UK: Cambridge University Press, 2002.

[27] J. E. Hansen and L. D. Travis, “Light scattering in planetary atmospheres,” *Space Sci. Rev.*, vol. 16, no. 4, pp. 527–610, 1974.

[28] M. Saito, P. Yang, J. Ding, and X. Liu, “A comprehensive database of the optical properties of irregular aerosol particles for radiative transfer simulations,” *J. Atmos. Sci.*, vol. 78, no. 7, pp. 2089–2111, 2021.

[29] Q. Fu and W. Sun, “Mie theory for light scattering by a spherical particle in an absorbing medium,” *Appl. Opt.*, vol. 40, no. 9, pp. 1354–1361, 2001.

[30] P. Yang *et al.*, “Inherent and apparent scattering properties of coated or uncoated spheres embedded in an absorbing host medium,” *Appl. Opt.*, vol. 41, no. 15, pp. 2740–2759, 2002.

[31] W. E. Meador and W. R. Weaver, “Two-stream approximations to radiative transfer in planetary atmospheres: A unified description of existing methods and a new improvement,” *Journal of Atmospheric Sciences*, vol. 37, no. 3, pp. 630–643, 1980.

[32] S. Wang, T. Ren, P. Yang, M. Saito, and H. E. Brindley, “Improved Temperature-Dependent Ice Refractive Index Compilation in the Far-Infrared Spectrum,” *Geophys. Res. Lett.*, vol. 51, no. 14, Jul. 2024, doi: 10.1029/2024GL110176.

[33] S. Wang, P. Yang, H. E. Brindley, X. Huang, and T. S. L’ecuyer, “Enhanced full spectral temperature-dependent refractive index of liquid water from supercooled to ambient conditions,” *Geophys. Res. Lett.*, vol. 53, no. 6, p. e2025GL119385, 2026.

[34] J. S. Foot, “Some observations of the optical properties of clouds. II: Cirrus,” *Quarterly Journal of the Royal Meteorological Society*, vol. 114, no. 479, pp. 145–164, 1988.

[35] P. Yang, K.-N. Liou, L. Bi, C. Liu, B. Yi, and B. A. Baum, “On the radiative properties of ice clouds: Light scattering, remote sensing, and radiation parameterization,” *Adv. Atmos. Sci.*, vol. 32, no. 1, pp. 32–63, 2015.

[36] C. F. Bohren and D. R. Huffman, *Absorption and scattering of light by small particles*. John Wiley & Sons, 2008.

[37] K. Yee, “Numerical solution of initial boundary value problems involving Maxwell’s equations in isotropic media,” *IEEE Trans. Antennas Propag.*, vol. 14, no. 3, pp. 302–307, 1966.

[38] P. Yang and K. N. Liou, “Finite-difference time domain method for light scattering by small ice crystals in three-dimensional space,” *Journal of the Optical Society of America A*, vol. 13, no. 10, pp. 2072–2085, 1996.

[39] W. Sun, Q. Fu, and Z. Chen, “Finite-difference time-domain solution of light scattering by dielectric particles with a perfectly matched layer absorbing boundary condition,” *Appl. Opt.*, vol. 38, no. 15, pp. 3141–3151, 1999.

[40] J.-P. Berenger, “A perfectly matched layer for the absorption of electromagnetic waves,” *J. Comput. Phys.*, vol. 114, no. 2, pp. 185–200, 1994.

[41] E. M. Purcell and C. R. Pennypacker, “Scattering and absorption of light by nonspherical dielectric grains,” *Astrophysical Journal, Vol. 186, pp. 705-714 (1973)*, vol. 186, pp. 705–714, 1973.

[42] B. T. Draine and P. J. Flatau, “Discrete-dipole approximation for scattering calculations,” *Journal of the Optical Society of America A*, vol. 11, no. 4, pp. 1491–1499, 1994.

[43] M. A. Yurkin and A. G. Hoekstra, “The discrete dipole approximation: an overview and recent developments,” *J. Quant. Spectrosc. Radiat. Transf.*, vol. 106, no. 1–3, pp. 558–589, 2007.

[44] Q. H. Liu, “The PSTD algorithm: A time-domain method requiring only two cells per wavelength,” *Microw. Opt. Technol. Lett.*, vol. 15, no. 3, pp. 158–165, 1997.

[45] C. Liu, L. Bi, R. L. Panetta, P. Yang, and M. A. Yurkin, “Comparison between the pseudo-spectral time domain method and the discrete dipole approximation for light scattering simulations,” *Opt. Express*, vol. 20, no. 15, pp. 16763–16776, 2012.

[46] S. Asano and G. Yamamoto, “Light scattering by a spheroidal particle,” *Appl. Opt.*, vol. 14, no. 1, pp. 29–49, 1975.

[47] J. Ding and P. Yang, “Separation of variables method for light scattering by two-layer spheroids with size parameters up to 1000,” *Opt. Express*, vol. 33, no. 19, pp. 40532–40564, 2025.

[48] J. Ding and P. Yang, “Improving numerical stability of the separation of variables method for light scattering by spheroids with size parameters beyond 1000,” *J. Quant. Spectrosc. Radiat. Transf.*, p. 109644, 2025.

[49] M. I. Mishchenko and L. D. Travis, “Light scattering by polydispersions of randomly oriented spheroids with sizes comparable to wavelengths of observation,” *Appl. Opt.*, vol. 33, no. 30, pp. 7206–7225, 1994.

[50] B. R. Johnson, “Invariant imbedding T matrix approach to electromagnetic scattering,” *Appl. Opt.*, vol. 27, no. 23, pp. 4861–4873, 1988.

[51] L. Bi and P. Yang, “Accurate simulation of the optical properties of atmospheric ice crystals with the invariant imbedding T-matrix method,” *J. Quant. Spectrosc. Radiat. Transf.*, vol. 138, pp. 17–35, 2014.

[52] S. Wang, “Separation of Variables and T-Matrix Method for Efficient Computation of Light Scattering by Single- and Two-Layer Spheroids,” *Opt. Express*, to be submitted, 2026.

[53] P. Yang, *Physical-geometric optics for light-scattering by nonspherical particles: Applications to remote sensing and climate science*. Cambridge University Press, 2026.

[54] P. Yang and K. N. Liou, “Geometric-optics–integral-equation method for light scattering by nonspherical ice crystals,” *Appl. Opt.*, vol. 35, no. 33, pp. 6568–6584, 1996.

[55] O. Dubovik *et al.*, “Application of spheroid models to account for aerosol particle nonsphericity in remote sensing of desert dust,” *Journal of Geophysical Research: Atmospheres*, vol. 111, no. D11, 2006.

[56] O. Muñoz, F. Moreno, D. Guirado, D. D. Dabrowska, H. Volten, and J. W. Hovenier, “The Amsterdam–Granada light scattering database,” *J. Quant. Spectrosc. Radiat. Transf.*, vol. 113, no. 7, pp. 565–574, 2012.

[57] L. Bi, P. Yang, G. W. Kattawar, Y. Hu, and B. A. Baum, “Scattering and absorption of light by ice particles: Solution by a new physical-geometric optics hybrid method,” *J. Quant. Spectrosc. Radiat. Transf.*, vol. 112, no. 9, pp. 1492–1508, 2011.

[58] B. Sun, P. Yang, G. W. Kattawar, and X. Zhang, “Physical-geometric optics method for large size faceted particles,” *Opt. Express*, vol. 25, no. 20, pp. 24044–24060, 2017.

[59] Y. Takano and K.-N. Liou, “Solar radiative transfer in cirrus clouds. Part I: Single-scattering and optical properties of hexagonal ice crystals,” *Journal of Atmospheric Sciences*, vol. 46, no. 1, pp. 3–19, 1989.

[60] P. Yang, J. Ding, R. L. Panetta, K.-N. Liou, G. W. Kattawar, and M. Mishchenko, “On the convergence of numerical computations for both exact and approximate solutions for electromagnetic scattering by nonspherical dielectric particles,” *Progress In Electromagnetics Research.*, vol. 164, p. 27, 2019.

[61] P. Yang and K. N. Liou, “Light scattering by hexagonal ice crystals: solutions by a ray-by-ray integration algorithm,” *Journal of the Optical Society of America A*, vol. 14, no. 9, pp. 2278–2289, 1997.

[62] M. Saito and P. Yang, “Generalization of atmospheric nonspherical particle size: Interconversions of size distributions and optical equivalence,” *J. Atmos. Sci.*, vol. 79, no. 12, pp. 3333–3349, 2022.

[63] Y. Zhang, P. Yang, M. Gao, and X. Zhang, “Optical properties simulated for oceanic particles with nonspherical core-shell morphologies,” *J. Quant. Spectrosc. Radiat. Transf.*, vol. 338, p. 109400, 2025.

[64] J. Coy, “A Novel Ice Cloud Optical Property Model for Passive and Active Remote Sensing Applications,” *Journal of Geophysical Research: Atmospheres*, in review, 2026.

[65] D. M. Winker *et al.*, “The CALIPSO mission: A global 3D view of aerosols and clouds,” *Bull. Am. Meteorol. Soc.*, vol. 91, no. 9, pp. 1211–1230, 2010.

[66] R. M. Goody and Y. L. Yung, *Atmospheric radiation: theoretical basis*. Oxford university press, 1995.

[67] I. E. Gordon and R. J. Hargreaves, “Preface to the HITRAN 2024: HITRAN special issue to celebrate the scientific contributions of Dr. Laurence Rothman,” *J. Quant. Spectrosc. Radiat. Transf.*, vol. 352, p. 109813, 2026.

[68] K.-N. Liou, *An introduction to atmospheric radiation*, vol. 84. Academic press, 2002.

[69] S. A. Clough, M. J. Iacono, and J.-L. Moncet, “Line-by-line calculations of atmospheric fluxes and cooling rates: Application to water vapor (paper 92jd01419),” *JOURNAL OF GEOPHYSICAL RESEARCH-ALL SERIES-*, vol. 97, pp. 15–761, 1992.

[70] M. J. Alvarado *et al.*, “Performance of the Line-By-Line Radiative Transfer Model (LBLRTM) for temperature, water vapor, and trace gas retrievals: recent updates evaluated with IASI case studies,” *Atmos. Chem. Phys.*, vol. 13, no. 14, pp. 6687–6711, 2013.

[71] A. A. Lacis and V. Oinas, “A description of the correlated k distribution method for modeling nongray gaseous absorption, thermal emission, and multiple scattering in vertically inhomogeneous atmospheres,” *Journal of Geophysical Research: Atmospheres*, vol. 96, no. D5, pp. 9027–9063, 1991.

[72] Q. Fu and K. N. Liou, “On the correlated k-distribution method for radiative transfer in nonhomogeneous atmospheres,” *Journal of Atmospheric Sciences*, vol. 49, no. 22, pp. 2139–2156, 1992.

[73] D. P. Kratz and F. G. Rose, “Accounting for molecular absorption within the spectral range of the CERES window channel,” *J. Quant. Spectrosc. Radiat. Transf.*, vol. 61, no. 1, pp. 83–95, 1999.

[74] D. P. Edwards and G. L. Francis, “Improvements to the correlated-k radiative transfer method: Application to satellite infrared sounding,” *Journal of Geophysical Research: Atmospheres*, vol. 105, no. D14, pp. 18135–18156, 2000.

[75] H. H. Aumann *et al.*, “AIRS/AMSU/HSB on the Aqua mission: Design, science objectives, data products, and processing systems,” *IEEE Transactions on Geoscience and Remote Sensing*, vol. 41, no. 2, pp. 253–264, 2003.

[76] C. Clerbaux *et al.*, “Monitoring of atmospheric composition using the thermal infrared IASI/MetOp sounder,” *Atmos. Chem. Phys.*, vol. 9, no. 16, pp. 6041–6054, 2009.

[77] X. Liu, W. L. Smith Sr, D. K. Zhou, and A. M. Larar, “A principal component-based radiative transfer forward model (PCRTM) for hyperspectral instruments,” in *Multispectral and Hyperspectral Remote Sensing Instruments and Applications II*, SPIE, 2005, pp. 96–105.

[78] X. Liu, W. L. Smith, D. K. Zhou, and A. Larar, “Principal component-based radiative transfer model for hyperspectral sensors: Theoretical concept,” *Appl. Opt.*, vol. 45, no. 1, pp. 201–209, 2006.

[79] X. Liu *et al.*, “Development of a fast and accurate PCRTM radiative transfer model in the solar spectral region,” *Appl. Opt.*, vol. 55, no. 29, pp. 8236–8247, 2016.

[80] V. Natraj, R.-L. Shia, and Y. L. Yung, “On the use of principal component analysis to speed up radiative transfer calculations,” *J. Quant. Spectrosc. Radiat. Transf.*, vol. 111, no. 5, pp. 810–816, 2010.

[81] V. Natraj, X. Jiang, R. Shia, X. Huang, J. S. Margolis, and Y. L. Yung, “Application of principal component analysis to high spectral resolution radiative transfer: A case study of the O2 A band,” *J. Quant. Spectrosc. Radiat. Transf.*, vol. 95, no. 4, pp. 539–556, 2005.

[82] M. I. Mishchenko, L. D. Travis, and A. A. Lacis, *Multiple scattering of light by particles: radiative transfer and coherent backscattering*. Cambridge University Press, 2006.

[83] J. I. F. King, “The radiative heat transfer of planet earth. Scientific Use of Earth Satellites,” *Ann Arbor*, 1956.

[84] L. D. Kaplan, “Inference of atmospheric structure from remote radiation measurements,” *J. Opt. Soc. Am.*, vol. 49, no. 10, pp. 1004–1007, 1959.

[85] W. L. Smith, “Iterative solution of the radiative transfer equation for the temperature and absorbing gas profile of an atmosphere,” *Appl. Opt.*, vol. 9, no. 9, pp. 1993–1999, 1970.

[86] S. A. Ackerman, K. I. Strabala, W. P. Menzel, R. A. Frey, C. C. Moeller, and L. E. Gumley, “Discriminating clear sky from clouds with MODIS,” *Journal of Geophysical Research: Atmospheres*, vol. 103, no. D24, pp. 32141–32157, 1998.

[87] W. B. Rossow, “Measuring cloud properties from space: A review,” *J. Clim.*, vol. 2, no. 3, pp. 201–213, 1989.

[88] W. B. Rossow, L. C. Garder, and A. A. Lacis, “Global, seasonal cloud variations from satellite radiance measurements. Part I: Sensitivity of analysis,” *J. Clim.*, vol. 2, no. 5, pp. 419–458, 1989.

[89] W. B. Rossow and L. C. Garder, “Cloud detection using satellite measurements of infrared and visible radiances for ISCCP,” *J. Clim.*, vol. 6, no. 12, pp. 2341–2369, 1993.

[90] G. Seze and W. B. Rossow, “Time-cumulated visible and infrared radiance histograms used as descriptors of surface and cloud variations,” *Int. J. Remote Sens.*, vol. 12, no. 5, pp. 877–920, 1991.

[91] R. W. Saunders and K. T. Kriebel, “An improved method for detecting clear sky and cloudy radiances

from AVHRR data," *Int. J. Remote Sens.*, vol. 9, no. 1, pp. 123–150, 1988.

[92] K. T. Kriebel, R. W. Saunders, and G. Gesell, "Optical properties of clouds derived from fully cloudy AVHRR pixels," *Beiträge zur Physik der Atmosphäre*, vol. 62, pp. 165–171, 1989.

[93] G. Gesell, "An algorithm for snow and ice detection using AVHRR data: An extension to the APOLLO software package," *Int. J. Remote Sens.*, vol. 10, no. 4, pp. 897–905, 1989.

[94] L. L. Stowe *et al.*, "Global distribution of cloud cover derived from NOAA/AVHRR operational satellite data," *Advances in Space Research*, vol. 11, no. 3, pp. 51–54, 1991.

[95] L. L. Stowe, S. K. Vemury, and A. V Rao, "AVHRR clear-sky radiation data sets at NOAA/NESDIS," *Advances in Space Research*, vol. 14, no. 1, pp. 113–116, 1994.

[96] J. Key, "The Cloud and Surface Parameter Retrieval (CASPR) System for Polar AVHRR, User's Guide. Cooperative Institute for Meteorological Satellite Studies, University of Wis- consin, Madison," p. 59, 2002.

[97] G. B. Gustafson, R. G. Isaacs, R. P. d'Entremont, J. M. Sparrow, and T. M. Hamill, "Support of environmental requirements for cloud analysis and archive (SERCAA): Algorithm Descriptions," 1994.

[98] L. M. McMillin and C. Dean, "Evaluation of a new operational technique for producing clear radiances," *Journal of Applied Meteorology*, vol. 21, pp. 1005–1014, 1982.

[99] J. Li, W. P. Menzel and A. J. Schriener, "Variational retrieval of cloud parameters from GOES sounder longwave cloudy radiance measurements," *Journal of Applied meteorology*, vol. 40, pp. 312–330, 2001.

[100] A. J. Schreiner T. J. Schmit and W. P. Menzel, "Observations and trends of clouds based on GOES Sounder data," *J. Geophys. Res.*, vol. 106, no. D17, pp. 20349–20363, 2001.

[101] W. P. Menzel R. A *et al.*, "MODIS global cloud-top pressure and amount estimation: algorithm description and results," *Journal of Applied Meteorology and Climatol- ogy*, vol. 47, pp. 1175–1198, 2008.

[102] K. D. Hutchison and J. M. Jackson, "Cloud detection over desert regions using the 412 nanometer MODIS channel," *Geophys. Res. Lett.*, vol. 30, no. 23, 2003.

[103] K. D. Hutchison *et al.*, "Automated cloud detection and classification of data collected by the Visible Infrared Imager Radiometer Suite (VIIRS)," *Int. J. Remote Sens.*, vol. 26, no. 21, pp. 4681–4706, 2005.

[104] E. G. Moody, M. D. King, S. Platnick, C. B. Schaaf, and F. Gao, "Spatially complete global spectral surface albedos: Value-added datasets derived from Terra MODIS land products," *IEEE Transactions on Geoscience and Remote Sensing*, vol. 43, no. 1, pp. 144–158, 2005.

[105] E. P. McClain, "Evaluation of CLAVR Phase-I Algorithm Performance—Final Report," 1993, *US Department of Commerce/NOAA/NESDIS, Report*.

[106] B. Pinty and M. M. Verstraete, "GEMI: A non-linear index to monitor global vegetation from satellites," *Vegetatio*, vol. 101, pp. 15–20, 1992.

[107] B. Gao, A. F. H. Goetz, and W. J. Wiscombe, "Cirrus cloud detection from airborne imaging spectrometer data using the 1.38 µm water vapor band," *Geophys. Res. Lett.*, vol. 20, no. 4, pp. 301–304, 1993.

[108] Ben-Dor, "A precaution regarding cirrus cloud detection from airborne imaging spectrome-ter data using the 1.38 um water vapor band," *Journal of Remote Sensing*, vol. 50, pp. 346–350, 1994.

[109] T. Inoue, "A cloud type classification with NOAA 7 split window measuremenets," *J. Geophys. Res.*, vol. 92, no. D4, pp. 3991–4000, 1987.

[110] O. B. Brown *et al.*, "MODIS infrared sea surface temperature algorithm algorithm theoretical basis document version 2.0," *University of Miami*, vol. 31, pp. 33–98, 1999.

[111] K. D. Hutchison and K. R. Hardy, "Threshold functions for automated cloud analyses of global meteorological satellite imagery," *Int. J. Remote Sens.*, vol. 16, no. 18, pp. 3665–3680, 1995.

[112] Y. Liu, J. R. Key, R. A. Frey, S. A. Ackerman, and W. P. Menzel, "Nighttime polar cloud detection with MODIS," *Remote Sens. Environ.*, vol. 92, no. 2, pp. 181–194, 2004.

[113] A. Gruber and T. S. Chen, "Diurnal variation of outgoing longwave radiation," *Journal of climatology*, vol. 8, no. 1, pp. 1–16, 1988.

[114] W. B. Rossow and A. A. Lacis, "Global, seasonal cloud variations from satellite radiance measurements. Part II. Cloud properties and radiative effects," *J. Clim.*, vol. 3, no. 11, pp. 1204–1253, 1990.

[115] D. P. Wylie and W. P. Menzel, "Two years of cloud cover statistics using VAS," *J. Clim.*, vol. 2, pp. 380–392, 1989.

[116] M. C. Wu and J. Susskind, "Outgoing long-wave radiation computed from HIRS2/MSU soundings," *Journal of Geophysical Research: Atmospheres*, vol. 95, no. D6, pp. 7579–7602, 1990.

[117] F. Parol, J. C. Buriez, G. Brogniez, and Y. Fouquart, "Information content of AVHRR channels 4 and 5 with respect to the effective radius of cirrus cloud particles," *J. Appl. Meteorol. Climatol.*, vol. 30, no. 7, pp. 973–984, 1991.

[118] M. J. Pavolonis, "Advances in extracting cloud composition information from spaceborne infrared radiances—A robust alternative to brightness temperatures. Part I: Theory," *J. Appl. Meteorol. Climatol.*, vol. 49, no. 9, pp. 1992–2012, 2010.

[119] A. K. Heidinger, M. J. Pavolonis, R. E. Holz, B. A. Baum, and S. Berthier, "Using CALIPSO to explore the sensitivity to cirrus height in the infrared observations from NPOESS/VIIRS and GOES-R/ABI," *Journal of Geophysical Research: Atmospheres*, vol. 115, no. D4, 2010.

[120] A. K. Heidinger and M. J. Pavolonis, "Gazing at cirrus clouds for 25 years through a split window. Part

I: Methodology," *J. Appl. Meteorol. Climatol.*, vol. 48, no. 6, pp. 1100–1116, 2009.

[121] C. D. Rodgers, *Inverse methods for atmospheric sounding: theory and practice*, vol. 2. World scientific, 2000.

[122] D. Li, M. Saito, and P. Yang, "Time-dependent systematic biases in inferring ice cloud properties from geostationary satellite observations," *Remote Sens. (Basel).*, vol. 15, no. 3, p. 855, 2023.

[123] D. Li, M. Saito, P. Yang, N. G. Loeb, W. L. Smith, and P. Minnis, "On the Scattering-Angle Dependence of the Spectral Consistency of Ice Cloud Optical Thickness Retrievals Based on Geostationary Satellite Observations," *IEEE Transactions on Geoscience and Remote Sensing*, vol. 61, pp. 1–12, 2023.

[124] B. Yi, X. Huang, P. Yang, B. A. Baum, and G. W. Kattawar, "Considering polarization in MODIS-based cloud property retrievals by using a vector radiative transfer code," *J. Quant. Spectrosc. Radiat. Transf.*, vol. 146, pp. 540–548, 2014.

[125] T. J. Schmit, M. M. Gunshor, W. P. Menzel, J. J. Gurka, J. Li, and A. S. Bachmeier, "Introducing the Next-Generation Advanced Baseline Imager on GOES-R," *Bull. Am. Meteorol. Soc.*, vol. 86, no. 8, pp. 1079–1096, 2005, doi: 10.1175/BAMS-86-8-1079.

[126] T. Inoue, "On the temperature and effective emissivity determination of semi-transparent cirrus clouds by bi-spectral measurements in the 10μm window region," *Journal of the Meteorological Society of Japan. Ser. II*, vol. 63, no. 1, pp. 88–99, 1985.

[127] A. Garnier *et al.*, "Retrieval of cloud properties using CALIPSO Imaging Infrared Radiometer. Part I: Effective emissivity and optical depth," *J. Appl. Meteorol. Climatol.*, vol. 51, no. 7, pp. 1407–1425, 2012.

[128] "https://atmosphere-imager.gsfc.nasa.gov."

[129] D. Tanré, Y. J. Kaufman, M. Herman, and S. Mattoo, "Remote sensing of aerosol properties over oceans using the MODIS/EOS spectral radiances," *Journal of Geophysical Research: Atmospheres*, vol. 102, no. D14, pp. 16971–16988, 1997, doi: 10.1029/96JD03437.

[130] Y. J. Kaufman, D. Tanré, L. A. Remer, E. F. Vermote, A. Chu, and B. N. Holben, "Operational remote sensing of tropospheric aerosol over land from EOS moderate resolution imaging spectroradiometer," *Journal of Geophysical Research: Atmospheres*, vol. 102, no. D14, pp. 17051–17067, 1997, doi: 10.1029/96JD03988.

[131] L. A. Remer *et al.*, "The dark target algorithm for observing the global aerosol system: Past, present, and future," *Remote Sens. (Basel).*, vol. 12, no. 18, p. 2900, 2020.

[132] V. Sawyer *et al.*, "An updated VIIRS dark target aerosol product for continuity with MODIS: assessing regional aerosol trends," *Front. Environ. Sci.*, vol. 13, p. 1602145, 2025.

[133] N. C. Hsu, S.-C. Tsay, M. D. King, and J. Herman, "Aerosol properties over bright-reflecting sourceregions," *IEEE Trans Geosci Remote Sens*, vol. 42, pp. 557–569, 2004, doi: 10.1109/TGRS.2004.824067.

[134] J. Lee, N. C. Hsu, W. V Kim, A. M. Sayer, and S. Tsay, "VIIRS version 2 deep blue aerosol products," *Journal of Geophysical Research: Atmospheres*, vol. 129, no. 6, p. e2023JD040082, 2024.

[135] A. Lyapustin *et al.*, "Multiangleimplementation of atmospheric correction (MAIAC): 2," 2011, doi: 10.1029/2010JD014986.

[136] "https://modis-land.gsfc.nasa.gov/MAIAC.html."

[137] "https://deepblue.gsfc.nasa.gov."

[138] "https://darktarget.gsfc.nasa.gov/."

[139] Y. J. Kaufman, "Measurements of the Aerosol Optical Thickness and The Path Radiance-Implication on Aerosol Remote Sensing and Atmospheric Corrections," in *10th Annual International Symposium on Geoscience and Remote Sensing*, IEEE, 1990, pp. 1023–1026.

[140] L. A. Remer *et al.*, "The MODIS aerosol algorithm, products,and validation," *J Atmos Sci*, vol. 62, no. 4, p. 947, 2005, doi: 10.1175/JAS3385.1.

[141] R. C. Levy *et al.*, "Thecollection 6 MODIS aerosol products over land and ocean," *Atmos Meas Tech*, vol. 6, pp. 2989–3034, 2013, doi: 10.5194/amt-6-2989-2013.

[142] L. A. Remer, S. Mattoo, R. C. Levy, A. Heidinger, R. B. Pierce, and M. Chin, "Retrieving aerosol in a cloudy environment: Aerosol product availability as a function of spatial resolution," *Atmos. Meas. Tech.*, vol. 5, no. 7, pp. 1823–1840, 2012.

[143] R. C. Levy, L. A. Remer, S. Mattoo, E. F. Vermote, and Y. J. Kaufman, "Second-generation opera-tional algorithm: retrieval of aerosol properties over land from inversion of moderate resolutionimaging Spectroradiometer spectral reflectance," *J Geophys Res*, vol. 112, p. D13211, 2007, doi: 10.1029/2006JD007811.

[144] Y. J. Kaufman, O. Boucher, D. Tanré, M. Chin, L. A. Remer, and T. Takemura, "Aerosol anthro-pogenic component estimated from satellite data," *Geophys Res Lett*, vol. 32, p. L17804, 2005, doi: 10.1029/2005GL023125.

[145] Y. J. Kaufman, I. Koren, L. A. Remer, D. Tanré, P. Ginoux, and S. Fan, "Dust transport anddeposition observed from the Terra-moderate resolution imaging Spectroradiometer (MODIS)spacecraft over the Atlantic Ocean," 2005, doi: 10.1029/2003JD004436.

[146] J. Lee, N. C. Hsu, A. M. Sayer, C. Bettenhausen, and P. Yang, "AERONET-based nonspherical dust optical models and effects on the VIIRS Deep Blue/SOAR over-water aerosol product," *Journal of Geophysical Research: Atmospheres*, vol. 122, no. 19, pp. 10384–10401, 2017, doi: 10.1002/2017JD027258.

[147] D. M. Giles *et al.*, "Advancements in theaerosol robotic network (AERONET) version 3 database–automated near-real-time qualitycontrol algorithm with improved cloud screening for sun photometer aerosol optical depth (AOD) measurements," *Atmos*

Meas Tech, vol. 12, pp. 169–209, 2019, doi: 10.5194/amt-12-169-2019.
[148] "https://aeronet.gsfc.nasa.gov."
[149] L. A. Munchak *et al.*, "MODIS 3 km aerosol product: algorithm and global perspective," *Atmos Meas Tech*, vol. 6, no. 7, p. 1829, 2013, doi: 10.5194/amt-6-1829-2013.
[150] A. M. Sayer, L. A. Munchak, N. C. Hsu, R. C. Levy, C. Bettenhausen, and M. J. Jeong, "MODIScollection 6 aerosol products: comparison between Aqua's e-deep blue, dark target, and'merged'data sets, and usage recommendations," *J Geophys Res Atmos*, vol. 119, no. 24, p. 13, 2014, doi: 10.1002/2014JD022453.
[151] H. Jethva, O. Torres, and Y. Yoshida, "Accuracy assessment of MODIS land aerosol opticalthickness algorithms using AERONET measurements over North America," 2019, doi: 10.5194/amt-12-4291-2019.
[152] V. S. Martins, A. Lyapustin, C. L. A. de, C. C. F. Barbosa, and E. Novo, "Validation ofhigh-resolution MAIAC aerosol product over South America," *J Geophys Res Atmos*, vol. 122, no. 14, p. 7537, 2017, doi: 10.1002/2016JD026301.
[153] A. Smirnov *et al.*, "Maritime aerosol network as a component of aerosolrobotic network," *J Geophys Res Atmos*, vol. 114, p. D06204, 2009, doi: 10.1029/2008JD011257.
[154] "https://ladsweb.modaps.eosdis.nasa.gov/missions-and-measurements/science-domain/aerosol/.Accessed", [Online]. Available: https://ladsweb.modaps.eosdis.nasa.gov/missions-and-measurements/science-domain/aerosol/.Accessed
[155] "https://ladsweb.modaps.eosdis.nasa.gov/missions-and-measurements/science-domain/l3-atmosphere/", [Online]. Available: https://ladsweb.modaps.eosdis.nasa.gov/missions-and-measurements/science-domain/l3-atmosphere/
[156] C. Di Biagio *et al.*, "Global scale variability of the mineral dust long-wave refractive index: a new dataset of in situ measurements for climate modeling and remote sensing," *Atmos. Chem. Phys.*, vol. 17, no. 3, pp. 1901–1929, 2017.
[157] D. Scheuvens, L. Schütz, K. Kandler, M. Ebert, and S. Weinbruch, "Bulk composition of northern African dust and its source sediments—A compilation," *Earth. Sci. Rev.*, vol. 116, pp. 170–194, 2013.
[158] K. Kandler *et al.*, "Chemical composition and complex refractive index of Saharan Mineral Dust at Izaña, Tenerife (Spain) derived by electron microscopy," *Atmos. Environ.*, vol. 41, no. 37, pp. 8058–8074, 2007.
[159] K. Kandler *et al.*, "Size distribution, mass concentration, chemical and mineralogical composition and derived optical parameters of the boundary layer aerosol at Tinfou, Morocco, during SAMUM 2006," *Tellus B: Chemical and Physical Meteorology*, vol. 61, no. 1, pp. 32–50, 2009.
[160] Y.-X. Hu, D. Winker, P. Yang, B. Baum, L. Poole, and L. Vann, "Identification of cloud phase from PICASSO-CENA lidar depolarization: A multiple scattering sensitivity study," *J. Quant. Spectrosc. Radiat. Transf.*, vol. 70, no. 4–6, pp. 569–579, 2001.
[161] M. Saito, P. Yang, A. K. Heidinger, and Y. Li, "An Improved Beta Method for Ice Cloud Property Retrievals: Theory," *Journal of Geophysical Research: Atmospheres*, vol. 125, no. 14, Jul. 2020, doi: 10.1029/2019JD031863.
[162] M. Saito, P. Yang, X. Huang, H. E. Brindley, M. G. Mlynczak, and B. H. Kahn, "Spaceborne Middle- and Far-Infrared Observations Improving Nighttime Ice Cloud Property Retrievals," *Geophys. Res. Lett.*, vol. 47, no. 18, Sep. 2020, doi: 10.1029/2020GL087491.
[163] I. N. Sokolik, "Remote sensing of mineral dust aerosols in the UV/visible and IR regions," in *Optical remote sensing of the atmosphere and clouds III*, SPIE, 2003, pp. 265–271.
[164] P. Zhang, N. Lu, X. Hu, and C. Dong, "Identification and physical retrieval of dust storm using three MODIS thermal IR channels," *Glob. Planet. Change*, vol. 52, no. 1–4, pp. 197–206, 2006.
[165] D. Li, Y. Zhang, M. Saito, P. Yang, and Y. Hu, "The impact of dust mineralogical compositions on CALIOP-IIR-based retrievals of the optical and microphysical properties of dust plumes," *Journal of Geophysical Research: Atmospheres*, vol. 130, no. 14, p. e2025JD043829, 2025.
[166] B. Chen *et al.*, "Detection of dust aerosol by combining CALIPSO active lidar and passive IIR measurements," *Atmos. Chem. Phys.*, vol. 10, no. 9, pp. 4241–4251, 2010.
[167] M.-H. Kim, S.-W. Kim, and A. H. Omar, "Dust lidar ratios retrieved from the CALIOP measurements using the MODIS AOD as a constraint," *Remote Sens. (Basel).*, vol. 12, no. 2, p. 251, 2020.
[168] J. Zheng *et al.*, "The thermal infrared optical depth of mineral dust retrieved from integrated CALIOP and IIR observations," *Remote Sens. Environ.*, vol. 270, p. 112841, 2022.
[169] J. Zheng *et al.*, "Thermal infrared dust optical depth and coarse-mode effective diameter over oceans retrieved from collocated MODIS and CALIOP observations," *Atmos. Chem. Phys.*, vol. 23, no. 14, pp. 8271–8304, Jul. 2023, doi: 10.5194/acp-23-8271-2023.
[170] D. J. Diner *et al.*, "Multi-angle Imaging SpectroRadiometer (MISR) instrument description and experiment overview," *IEEE Transactions on Geoscience and Remote Sensing*, vol. 36, pp. 1072–1088, 1998.
[171] J. V Martonchik *et al.*, "Techniques for the retrieval of aerosol properties over land and ocean using multiangle imaging," *IEEE Transactions on Geoscience and Remote Sensing*, vol. 36, pp. 1212–1227, 1998.
[172] D. J. Diner *et al.*, "Using angular and spectral shape similarity constraints to improve MISR aerosol and surface retrievals over land," *Remote Sens. Environ.*, vol. 94, pp. 155–171, 2005.

[173] D. J. Diner *et al.*, “Level 2 Aerosol Retrieval Algorithm Theoretical Basis Document,” 2008.
[174] R. A. Kahn *et al.*, “Multiangle Imaging SpectroRadiometer global aerosol product assessment by comparison with the Aerosol Robotic Network,” *J. Geophys. Res.*, vol. 115, p. D23209, 2010.
[175] M. J. Garay *et al.*, “Introducing the 4.4 km spatial resolution Multi-Angle Imaging SpectroRadiometer (MISR) aerosol product,” *Atmos. Meas. Tech.*, vol. 13, pp. 593–628, 2020.
[176] M. L. Witek, M. J. Garay, D. J. Diner, M. A. Bull, and F. C. Seidel, “New approach to the retrieval of AOD and its uncertainty from MISR observations over dark water,” *Atmos. Meas. Tech.*, vol. 11, pp. 429–439, 2018.
[177] Y. Yang, L. Di Girolamo, and D. Mazzoni, “Selection of the automated thresholding algorithm for the MISR radiometric camera-by-camera cloud mask over land,” *Remote Sens. Environ.*, vol. 107, pp. 159–171, 2007.
[178] G. Zhao and L. Di Girolamo, “A cloud fraction versus view angle technique for automatic in-scene evaluation of the MISR cloud mask,” *Journal of Applied Meteorology*, vol. 43, pp. 860–869, 2004.
[179] L. Di Girolamo and M. J. Wilson, “A first look at band-differenced angular signatures for cloud detection from MISR,” *IEEE Transactions on Geoscience and Remote Sensing*, vol. 41, pp. 1730–1734, 2003.
[180] D. J. Diner *et al.*, “Exploration of a polarized surface bidirectional reflectance model using the Ground-based Multiangle SpectroPolarimetric Imager,” *Atmosphere (Basel).*, vol. 3, pp. 591–619, 2012.
[181] C. Cox and W. Munk, “Statistics of sea surface derived from sun glitter,” *J. Mar. Res.*, vol. 13, pp. 198–227, 1954.
[182] B. G. Smith, “Geometrical shadowing of a random rough surface,” *IEEE Trans. Antennas Propag.*, vol. 17, pp. 15668–15671, 1967.
[183] D. J. Diner *et al.*, “Advances in multiangle satellite remote sensing of speciated airborne particulate matter and association with adverse health effects: from MISR to MAIA,” *J. Appl. Remote Sens.*, vol. 12, p. 042603, 2018.
[184] J. V Martonchik, D. J. Diner, K. A. Crean, and M. A. Bull, “Regional aerosol retrieval results from MISR,” *IEEE Transactions on geoscience and remote sensing*, vol. 40, no. 7, pp. 1520–1531, 2002.
[185] M. Born, E. Wolf, and A. Bhatia, “Principles of Optics (6 edition) Cambridge,” *Cambridge U. Press, Cambridge, UK*, 1999.
[186] S. Chandrasekhar, *Radiative transfer*. Courier Corporation, 2013.
[187] O. Dubovik, Z. Li, M. I. Mishchenko, D. Tanré, and Y. Karol, “Polarimetric remote sensing of atmospheric aerosols: Instruments, methodologies, results, and perspectives,” *J. Quant. Spectrosc. Radiat. Transf.*, vol. 224, pp. 474–511, 2019.
[188] A. Puthukkudy *et al.*, “Retrieval of aerosol properties from Airborne Hyper-Angular Rainbow Polarimeter (AirHARP) observations during ACEPOL 2017,” *Atmos. Meas. Tech.*, vol. 13, pp. 5207–5236, 2020.
[189] J. M. Smit *et al.*, “SPEX airborne spectropolarimeter calibration and performance,” *Appl. Opt.*, vol. 58, pp. 5695–5719, 2019.
[190] P. J. Werdell *et al.*, “The plankton, aerosol, cloud, ocean ecosystem mission: status, science, advances,” *Bull. Am. Meteorol. Soc.*, vol. 100, no. 9, pp. 1775–1794, 2019.
[191] J. V Martins, R. Fernandez-Borda, B. McBride, L. A. Remer, and H. M. J. Barbosa, “The HARP Hyperangular Imaging Polarimeter and the need for small satellite payloads with high science payoff for Earth science remote sensing,” in *Proc. IEEE International Geoscience and Remote Sensing Symposium (IGARSS)*, 2018, pp. 6304–6307.
[192] O. P. Hasekamp *et al.*, “Aerosol measurements by SPEXone on the NASA PACE mission: expected retrieval capabilities,” *J. Quant. Spectrosc. Radiat. Transf.*, vol. 227, pp. 170–184, 2019.
[193] G. Meister *et al.*, “The Ocean Color Instrument (OCI) on the PACE mission: system design and prelaunch radiometric performance,” *IEEE Transactions on Geoscience and Remote Sensing*, vol. 62, p. 5517418, 2024.
[194] F. Xu *et al.*, “Coupled retrieval of aerosol properties and land surface reflection using the Airborne Multiangle SpectroPolarimetric Imager,” *Journal of Geophysical Research: Atmospheres*, vol. 122, pp. 7004–7026, 2017.
[195] D. J. Diner *et al.*, “The Airborne Multiangle SpectroPolarimetric Imager (AirMSPI): a new tool for aerosol and cloud remote sensing,” *Atmos. Meas. Tech.*, vol. 6, pp. 2007–2025, 2013.
[196] O. P. Hasekamp and J. Landgraf, “Retrieval of aerosol properties over land surfaces: capabilities of multiple-viewing-angle intensity and polarization measurements,” *Appl. Opt.*, vol. 46, pp. 3332–3344, 2007.
[197] L. Wu, O. Hasekamp, B. van Diedenhoven, and B. Cairns, “Aerosol retrieval from multiangle, multispectral photopolarimetric measurements: importance of spectral range and angular resolution,” *Atmos. Meas. Tech.*, vol. 8, pp. 2625–2638, 2015.
[198] B. Cairns, E. E. Russell, and L. D. Travis, “The research scanning polarimeter: calibration and ground-based measurements,” in *Proc. SPIE*, 1999, p. 186.
[199] D. L. Phillips, “A technique for numerical solution of certain integral equations of the first kind,” *Journal of the Association for Computing Machinery*, vol. 9, pp. 84–97, 1962.
[200] S. Twomey, “On the numerical solution of Fredholm integral equations of the first kind by inversion of the linear system produced by quadrature,” *Journal of the Association for Computing Machinery*, vol. 10, pp. 97–101, 1963.

[201] S. Twomey, *Introduction to the Mathematics of Inversion in Remote Sensing and Indirect Measurements*. New York: Elsevier, 1977.
[202] A. N. Tikhonov, "On the solution of incorrectly stated problems and a method of regularization," *Dokl. Akad. Nauk SSSR*, vol. 151, pp. 501–504, 1963.
[203] A. N. Tikhonov and V. Y. Arsenin, *Solution of Ill-Posed Problems*. New York: Wiley, 1977.
[204] O. Dubovik *et al.*, "Statistically optimized inversion algorithm for enhanced retrieval of aerosol properties from spectral multi-angle polarimetric satellite observations," *Atmos. Meas. Tech.*, vol. 4, pp. 975–1018, 2011.
[205] O. Dubovik, "Optimization of numerical inversion in photopolarimetric remote sensing," in *Photopolarimetry in remote sensing*, Springer, 2006, pp. 65–106.
[206] O. Dubovik *et al.*, "Accuracy assessments of aerosol optical properties retrieved from AERONET sun and sky radiance measurements," *J. Geophys. Res.*, vol. 105, pp. 9791–9806, 2000.
[207] L. Li *et al.*, "Retrieval of aerosol components directly from satellite and ground-based measurements," *Atmos. Chem. Phys.*, vol. 19, pp. 13409–13435, 2019.
[208] L. Li *et al.*, "Retrievals of fine-mode light-absorbing carbonaceous aerosols from POLDER/PARASOL observations over East and South Asia," *Remote Sens. Environ.*, vol. 247, p. 111913, 2020.
[209] X. Zhang *et al.*, "Extensive characterization of aerosol optical properties and chemical component concentrations: application of the GRASP/Component approach to long-term AERONET measurements," *Science of the Total Environment*, vol. 812, p. 152553, 2022.
[210] F. Xu, D. J. Diner, O. Dubovik, and Y. Schechner, "A correlated multi-pixel inversion approach for aerosol remote sensing," *Remote Sens. (Basel).*, vol. 11, p. 746, 2019.
[211] T. Huang, F. Xu, L. Gao, C. J. Flynn, and O. Dubovik, "A correlation-based inversion method for aerosol property (CIMAP) retrieval from AERONET measurements," *J. Quant. Spectrosc. Radiat. Transf.*, vol. 272, p. 107808, 2021.
[212] Huang et al., "A correlation-based inversion approach for satellite-borne aerosol remote sensing," *J. Quant. Spectrosc. Radiat. Transf.*, submitted, 2026.
[213] M. Gao *et al.*, "Efficient multi-angle polarimetric inversion of aerosols and ocean color powered by a deep neural network forward model," *Atmos. Meas. Tech.*, vol. 14, pp. 4083–4110, 2021.
[214] C. Zhou, P. Yang, A. E. Dessler, Y. Hu, and B. A. Baum, "Study of horizontally oriented ice crystals with CALIPSO observations and comparison with Monte Carlo radiative transfer simulations," *J. Appl. Meteorol. Climatol.*, vol. 51, no. 7, pp. 1426–1439, 2012.
[215] Y. Hu *et al.*, "CALIPSO/CALIOP cloud phase discrimination algorithm," *J. Atmos. Ocean. Technol.*, vol. 26, no. 11, pp. 2293–2309, 2009.
[216] C. Zhou, P. Yang, A. E. Dessler, and F. Liang, "Statistical properties of horizontally oriented plates in optically thick clouds from satellite observations," *IEEE Geoscience and Remote Sensing Letters*, vol. 10, no. 5, pp. 986–990, 2012.
[217] S.-A. Boukabara, V. Krasnopolsky, J. Q. Stewart, E. S. Maddy, N. Shahroudi, and R. N. Hoffman, "Leveraging modern artificial intelligence for remote sensing and NWP: Benefits and challenges," *Bull. Am. Meteorol. Soc.*, vol. 100, no. 12, pp. ES473–ES491, 2019.
[218] Q. Yuan *et al.*, "Deep learning in environmental remote sensing: Achievements and challenges," *Remote Sens. Environ.*, vol. 241, p. 111716, 2020.

Ping Yang (Fellow, IEEE) received a Ph.D. degree from the University of Utah, Salt Lake City, Utah, USA, in 1995. He is a *Regents Professor* and *University Distinguished Professor* and holds the David Bullock Harris Chair in Geosciences at Texas A&M University, College, Texas, USA. His research focuses on light scattering, radiative transfer, and remote sensing. He has co-authored 394 refereed journal papers and five books.

He received many awards and honors, including the *NASA Exceptional Scientific Achievement Medal,* the biennial *David and Lucille Atlas Remote Sensing Prize* by AMS, the biennial *van de Hulst Light-Scattering Award* by Elsevier/JQSRT, the *Distinguished Texas Scientist Award* by the Texas Academy of Science, the quadrennial *Gold Medal Award* by the International Radiation Commission, and the *Humboldt Research Award* by the Alexander von Humboldt Foundation, Germany.

Dr. Yang is a Fellow of IEEE, the American Meteorological Society, the American Geophysical Union, the American Physical Society, OPTICA (formerly, the Optical Society of America), the Electromagnetics Academy, and the American Association for the Advancement of Science.

Kerry Meyer received the B.S. (2001), M.S. (2004), and PhD (2007) degrees from Texas A&M University. In his current role at NASA Goddard Space Flight Center, he is responsible for maintaining the cloud product algorithms for MODIS, VIIRS, and other like space borne and airborne imagers. His broader research activities include cloud and aerosol remote sensing and their applications.

Robert Levy, Climate and Radiation Laboratory, NASA's Goddard Space Flight Center in Greenbelt, MD, USA. He received the M.A., B.S. and PhD degrees from Oberlin College (1994), Colorado State University (1996), and the University of Maryland (2007), respectively. At NASA, he is focused on retrieving global aerosol properties from satellite observations and using the retrieved products for quantifying the role of aerosols in climate and air quality. He is responsible for maintaining the "Dark Target" aerosol algorithm and product suite representing multiple sensors.

Dongchen Li is currently a Postdoctoral Research Associate in the Department of Atmospheric Sciences at Texas A&M University, College Station, TX, USA. His research interests include satellite remote sensing of clouds and aerosols and radiative transfer.

Feng Xu received the Ph.D. degree in physics from the University of Rouen, France. He is currently an Associate Professor in the School of Meteorology, University of Oklahoma, Norman, OK, USA. His research focuses on environmental remote sensing, atmospheric radiative transfer, and light scattering by aerosol and cloud particles. Dr. Xu serves as an editor or associate editor for several journals in atmospheric science and remote sensing.

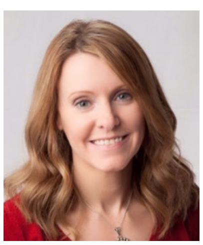

Anita D. Rapp received the B.S. degree in Meteorology from Texas A&M University, College Station, TX, U.S.A, in 2000. She received the M.S. degree in 2004 and the Ph.D. degrees in 2008 in Atmospheric Sciences from Colorado State University, Fort Collins, CO, U.S.A. She was a visiting postdoctoral fellow at the Cooperative Institute for Research in Environmental Sciences at the University of Colorado Boulder in 2009 and joined Texas A&M University in 2010. She is currently a Professor and the Graduate Program Director in the Department of Atmospheric Sciences at Texas A&M University in College Station, TX, U.S.A. Her research focuses on applications of multisensor satellite remote sensing observations to understand cloud and precipitation processes.

Zhibo Zhang received his Ph.D. in Atmospheric Sciences from Texas A&M University in 2008. After working at NASA Goddard Space Flight Center as a postdoctoral researcher for two years, he joined the Physics Department at UMBC in 2011. He is currently a full professor of Physics and leads the Aerosol Cloud Radiation—Observation and Simulation (ACROS) group. His research interests include aerosol-cloud-radiation interactions, aerosol and cloud remote sensing, machine learning and big data analytics, climate modeling, and climate change.